GEOCHEMISTRY AND PETROGENESIS OF JOHN DAY ASH FLOWS NEAR PRINEVILLE, OREGON

BY

KARYN ANN PATRIDGE

A thesis submitted in partial fulfillment
of the requirements for the degree of

MASTER OF SCIENCE IN GEOLOGY

WASHINGTON STATE UNIVERSITY
School of Earth and Environmental Sciences

MAY 2010

To the Faculty of Washington State University:

The members of the Committee appointed to examine the dissertation/thesis of KARYN ANN PATRIDGE find it satisfactory and recommend that it be accepted.

John A. Wolff, Ph. D., Chair

Peter B. Larson, Ph. D.

Jason D. McClaughry, M. S.

ACKNOWLEDGEMENTS

First I would like to thank my advisor Dr. John Wolff for suggesting this project, when I came to him only with the idea that I wanted to work with volcanic rocks. This project developed into quite an exciting adventure and opened up many avenues for future work. He is also responsible for connecting me with my field advisor Jason McClaughry, for which I am greatly appreciative.

Many thanks to Jason McClaughry for his help in the field; the maps that he produced made this project possible, while the opportunities he has provided me as student have helped me gain confidence and experience as a young professional geologists. Mark Ferns has also been an important ally during this project, by his constant encouragement and comic relief. I would also like to thank Carrie Gordon of the USFS always having a smile on her face.

I would also like to thank the technical staff here at WSU's GeoAnalytical laboratory. They were always quick to answer questions and help out during my XRF and ICP sample preparation, and special thanks to Scotty Cornelius for his help on the microprobe.

I would like to thank my friends that I have made during my time here at WSU. You have helped me get through this degree by listening to me complain, cry and play music down at Ricos.

Most importantly I would like to thank my family. They are my foundation; their love follows me everywhere, regardless of what I do.

GEOCHEMISTRY AND PETROGENESIS OF JOHN DAY ASH FLOWS NEAR PRINEVILLE, OREGON

Abstract

by Karyn Ann Patridge, M.S.
Washington State University
May 2010

Chair: John A. Wolff

The John Day rhyolite ash flows exposed near Prineville, Oregon are temporally equivalent to member G of the John Day Formation (JDF), a dominantly basalt-rhyolite bimodal province. Previous work has largely attributed John Day volcanism to subduction; however new data suggest this model needs revision.

The rhyolites share affinities with A-type granitoids, and can be divided into two peralkaline groups; a less fractionated high-Fe group with less depleted Sr and Eu and less enriched Th, Rb, Nb, Hf, and LREE abundances and a more fractionated low-Fe group. The high-Fe group exhibits constant Zr/Hf ratios indicating no zircon fractionation, while the low-Fe group exhibits decreasing Zr/Hf ratios indicative of zircon fractionation. Thus, the high-Fe group was originally more peralkaline than the low-Fe group.

The John Day rhyolites share striking similarities with the Trans-Pecos Volcanic Province (TPVP) rhyolites, which suggest they were derived by similar processes and their differences reflect variable source composition, degree of melting and fractionation. Viewed as a whole the TPVP displays a continual transition from calc-alkaline

compositions to strongly peralkaline compositions as a consequence to changing stress regimes. These stress changes are similar to those postulated for the compositional changes observed in Clarno-John Day volcanism. Thus, the Clarno and John Day Formations should be viewed as one magmatic province that evolved as a result of changing stress regimes in Oregon. The nature of what caused the initial switch is still under debate, but coincident magmatism throughout much of west suggests it was related to post-Laramide removal of the Farallon slab.

TABLE OF CONTENTS

PAGE

STRATIGRAPHY AND UNIT DESCRIPTIONS

MAJOR, MINOR AND TRACE ELEMENT GEOCHEMISTRY

DISCUSSION

APPENDICES

LIST OF FIGURES

PAGE

LIST OF TABLES

Introduction

Subduction-related volcanism has been a dominant process along the Pacific Northwest margin since the Mesozoic. Previous work has largely attributed the easterly inland volcanism of Montana and Wyoming to be the result of shallow slab subduction (Lipman and others, 1971). However, a model to explain how and why volcanism subsequently receeded westward to its current location along the Cascades arc is lacking. Detailed investigations of Basin and Range extension and associated rocks of the Oligocene-Miocene "ignimbrite flareup" throughout much of the southwest have largely been attributed to post-Laramide removal of the Farallon plate (Humphreys, 1995). But for areas north in central and eastern Oregon, lack of mapping and associated geochemical studies of Paleogene rocks has hindered the understanding of volcanism during the middle Eocene to Late Oligocene.

The late Eocene to Late Oligocene John Day Formation (JDF) of central and eastern Oregon marks a distinct change in the style of volcanic activity, from the widespread primarily calc-alkaline eruptions of the Clarno Formation to more localized bimodal basalt-rhyolite bimodal volcanism. Previous workers have postulated vent sites at or near the current Cascade arc (Robinson, 1975; Robinson and Brem, 1981; Robinson and others, 1984; Bestland and others, 1999), while others have suggested small Oligocene rhyolite domes scattered throughout central and eastern Oregon (Swanson, 1969; Robinson and others, 1984, 1990; Oberniller, 1987; Smith and others, 1998), but neither of these settings can fully explain the notable chemical differences and similarities and overlapping ages of the Clarno and John Day Formations. Moreover, the understanding of when the modern Cascades arc was established in Oregon remains unclear.

Recent mapping over the past decade has identified three Paleogene calderas well east of inferred source vents in the Cascades and much larger than the proposed rhyolite domes. These include the: (1) Wildcat Mountain Caldera (~40 Ma, McClaughry and others, 2009) (2) Crooked River Caldera (29.5 Ma, McClaughry and Ferns, 2007; McClaughry and others, 2009), and (3) Tower Mountain caldera (28.5 Ma, Ferns and others, 2001; McClaughry and others, 2009). However, the direct correlation of widespread ash flow tuffs and other pyroclastic deposits to vent sites remains poorly constrained in central and eastern Oregon. Additionally, reconnaissance geochemical sampling and radiometric dating of these units suggest many more vents exist, and have yet to be discovered.

This study focuses on John Day ash flow tuffs associated with the Crooked River caldera (CRC, McClaughry Ferns, 2007) at Prineville, Oregon, and aims to (1) geochemically characterize these units and try to constrain the magmatic processes involved in their petrogenesis, (2) establish a general conception of their volcano-tectonic setting, (3) apply geochemical data to improve stratigraphic correlation within the JDF and (4) add to the overall understanding of JDF volcanism and knowledge of Eocene to early Miocene volcanism in central and northeastern Oregon.

Review of Pre-Tertiary rocks in the Blue Mountains Province

The per-Tertiary rocks of Oregon consist of a collection of terranes that were accreted to the North American continent during the Mesozoic. Regional exposure of these rocks is largely restricted to a north-east-southwest trending belt in areas east and west of central Oregon in the Blue Mountains and Klamath Mountains provinces. A brief overivew of their lithologies is necessary, as they are most potential sources for silicic magmas and/or contaminants of mantle derived melts.

The rocks of the Blue Mountains Province (BMP) are commonly divided into four terranes that trend east and northeast across NE Oregon (Fig. 1) and include the Wallowa, Baker, Izee and Olds Ferry terranes (Vallier and others, 1977; Dickinson and Thayer, 1978; Brooks and Vallier, 1978; Dickinson, 1979; Silberling and others, 1984, Vallier, 1995). The Wallowa and Olds Ferry terranes contain Permian to Triassic plutonic, volcanic and volcaniclastic rocks that formed in two subduction related island arc systems (Vallier and others, 1977; Vallier, 1995; Brooks and Vallier, 1978; Dickinson, 1979, 2004; Kays and others, 2006). These island arc assemblages are separated by the Baker terrane, a large belt of subduction melange and arc-related igneous rocks. Overlying all these terranes are Upper Triassic to Jurassic marine sedimentary rocks of the Izee terrane (White and others, 1992; White and Vallier, 1994; Goldstrand, 1994, Vallier, 1995). The Baker and Izee terranes are closest to the study area, thus they will be reviewed in detail. Full descriptions of the Wallowa and Olds Ferry terranes can be found in Vallier and others, (1977); Dickinson and Thayer, (1978); Dickinson, (1979); Brooks, (1979a, b); Mullen, (1983); Silberling and others, (1984); Vallier and Engebretson, (1984); Vallier and Brooks, (1986); Vallier, (1995).

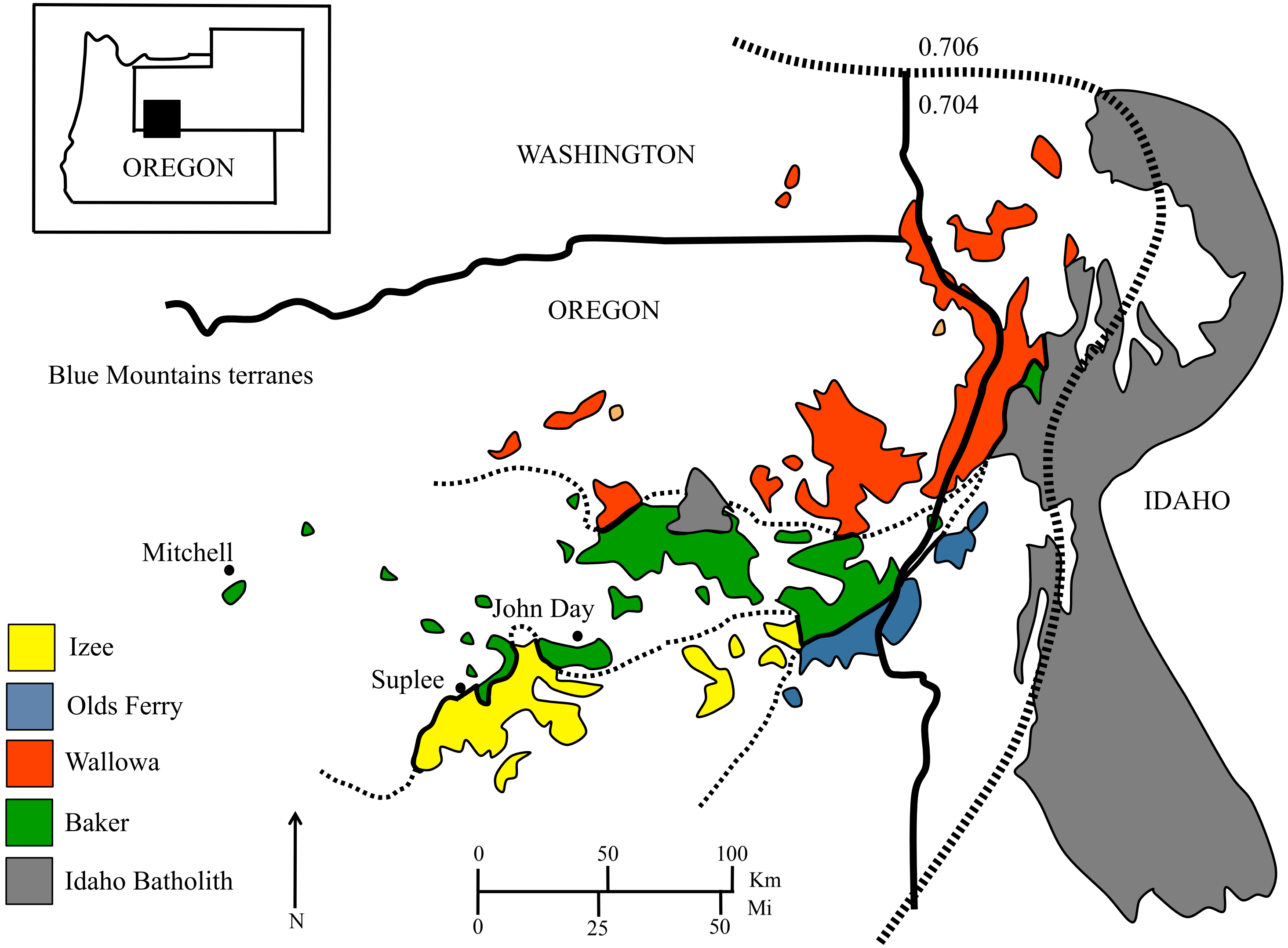

Figure 1. Map of central and eastern Oregon and western Idaho showing the extent of pre-Tertiary rocks. (Terrane names of Silberling and others, 1984; Modified after Blome and Nestell, 1991; LaMaskin and others, 2009). Black solid box shows the approximate location of study area.

The highly diverse Baker terrane contains deformed Permian to Jurassic argillite and chert, olistromal blocks of Devonian to Triassic limestone, serpentinized forearc and oceanic crustal fragments, arc related igneous rocks and locally developed blueschist facies, which were deformed in a long lived subduction and accretionary complex (Ferns and Brooks, 1995, Vallier, 1995). It also contains large blocks of obducted ophiolite sequences like the Canyon Mountain ophiolite complex (Vallier, 1995). The Izee terrane consists of Upper Triassic to Upper Jurassic marine sedimentary rocks that rest in depositional contact on older rocks and structures of the Baker, Wallowa and Olds Ferry terranes (Dickinson and Thayer, 1978; Dickinson, 1979; Brooks and Vallier, 1978; White and others, 1992; Goldstrand, 1994). Dorsey and LaMaskin (2007) divide the sedimentary rocks of the Izee terrane into two stratal packages: (1) MS-1, Late Triassic to Early Jurassic deposits that record a transition from (a) older volcanic and volcaniclastic deposits of the Wallowa and Olds Ferry forearc and intra-arc basins to (b) marine turbidites, shale, and argillite with chert clast conglomerates derived from the emerging Baker terrane; and (2) MS-2, Early to Late Jurassic marine deposits that overlap older structures and record ~20-40 m.y. of deep crustal subsidence in a large marine basin.

Traditionally, the BMP has been considered a single complex far traveled island arc (White and others, 1992; Vallier, 1995), but others (Dickinson, 1979, 2004) suggest that the BMP contains both intraoceanic and continental fringing island arc systems that are separated by a subduction/accretionary complex. More recently Dorsey and LaMaskin (2007) have suggested that the sedimentary rocks across the region were deposited in a subsiding basin. The growing number and variety of tectonic models underscores the geological and tectonic complexity of the BMP.

Final accretion of the BMP along the North American craton is generally thought to have occurred by Late Jurassic time, but the relationship between amalgamation and accretion and subsequent emplacement of numerous igneous plutons is unclear.

Early Magmatism in the Blue Mountains Province

Magmatism in the BMP occurred in three distinct pulses between 162 and 154 Ma, 148 and 137 Ma and 124 and 111 Ma based on U-Pb zircon ages compiled by LaMaskin and others (2009) from Walker (1986, 1989), Manduca (1993), Lee (2004), McClelland and Oldow (2007), Parker and others (2008), and Unruh and others (2008). The oldest belt consists of late Middle-Late Jurassic plutons in the Wallowa and Baker terranes and ranges in composition from gabbro to quartz diorite. Geochemically they are magnesian, calcic to calc-alkaline, and metaluminous, and have low Sr/Y, Na, Al, Sr, but high Y concentrations (LaMaskin and others, 2009).

The second pulse (148 and 137 Ma) consists of two spatially and geochemically distinct belts within the Wallowa and Baker terranes; one from 147-145 Ma with high Sr/Y (high Na, Al, Sr, but low Y) plutons, and another from 148-137 Ma with low Sr/Y (low Na, Al, Sr, but high Y). The plutons with low Sr/Y are similar to the older Middle-Late Jurassic plutons. LeMaskin and others (2009) attribute the variable low Sr/Y and high Sr/Y to reflect changes in source types. The higher Sr/Y ratios of the 147-145 Ma plutons likely reflect melting of dominantly Sr-enriched continental crust that was overly thickened during Late Jurassic orogenesis, whereas the lower Sr/Y likely reflect melting of less contracted crust.

The youngest phase of magmatism, before emplacement of the Idaho batholith, consists of small tonalitic and trondhjemitic plutons that can be divided into two subgroups; (1) 124-120 Ma metaluminous hornblende biotite tonalitic plutons in a northeast-southwest trending belt east of the Late Jurassic belt and (2) 125-111 Ma strongly peraluminous tonalite and trondhejemite plutons that extend subparallel to the Sr initial Sr 0.0706 line in western Idaho (LaMaskin and others, 2009).

Magmatic activity culminated in the Pacific Northwest during the Middle-Late Cretaceous with the emplacement of the Idaho batholith from 100-70 Ma straddling the accreted terrane-North American craton boundary (Armstrong and others, 1977). A lull in magmatism (70-55 Ma) followed, until calc-alkaline Eocene magmatism began in Oregon, Idaho, Montana, northeast Washington and southern British Columbia.

Early Cenozoic History and Volcanism in the Blue Mountains

The earliest Tertiary history in the region is preserved in highly weathered arkosic, carbonaceous and conglomeratic sedimentary Paleogene rocks poorly exposed along the axis of the Blue Mountains. Mineralogy and detritus suggest derivation from a granitic or metamorphic source, possibly from the Idaho batholith to the east. Overlying these strata are andesitic and dacitic volcanic and volcanogenic sedimentary rocks of the Clarno Formation (Walker and Robinson, 1990).

Volcanic rocks of the Clarno Formation are partly coeval with several other Eocene volcanic fields that are scattered throughout the Pacific Northwest and British Columbia, such as (1) Challis volcanics of Idaho, (2) Absaroka volcanics of Montana and Wyoming, (3) Alkalic rocks in Montana and (4) volcanic rocks of the Republic graben of northeast Washington and southern British Columbia (Fig. 2). These calc-alkaline

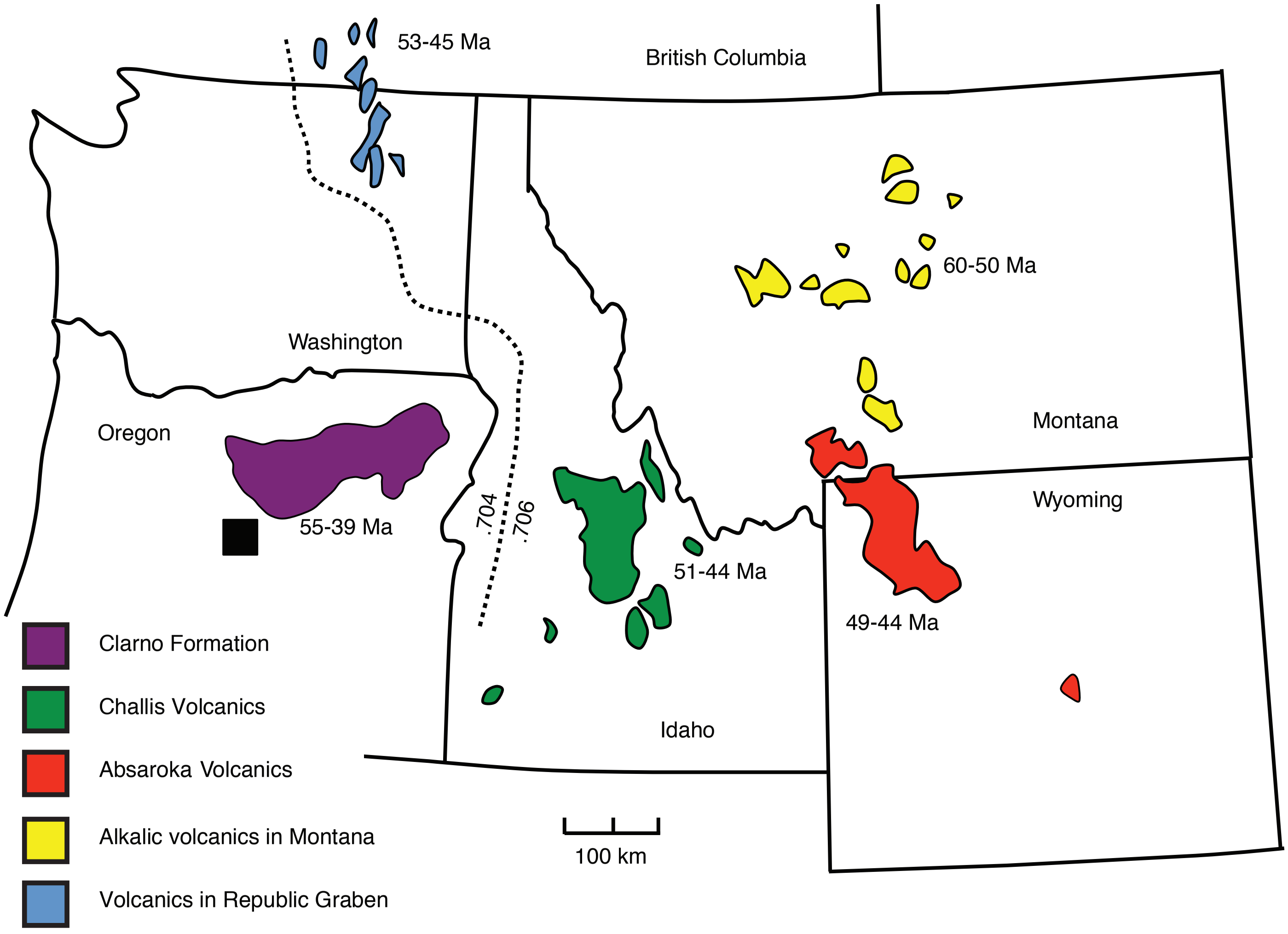

Figure 2. Map of Eocene volcanics throughout the Pacific Nortwest. (Modified after Moye and others, 1988). Black box indicates approximate field area.

volcanic fields have traditionally been linked to shallow slab subduction and fast convergence rates that caused inland volcanism (Lipman and others, 1971). Some workers (Snyder and others, 1976; Armstrong, 1978; Vance, 1982) believe Clarno volcanism is related to a single "Challis arc" that swept westward from Wyoming and Montana, into Idaho and through Oregon and into west-central Washington. However, this model struggles to explain the synchronous volcanism over such a wide area, their chemical differences and similarities, and the geometric orientation and position of the arc relative to the continental margin (Walker and Robinson, 1990).

The Clarno Formation lacks a formally defined regional stratigraphy, but available dates suggest the formation ranges in age from ca. 54 to 39 Ma. An older suite (53.6 ± 0.3 to 45.26 ± 0.31 Ma) similar in age to the Challis volcanics of Idaho (ca. 51-44 Ma; McIntyre and others, 1982), exposed near the hamlets of Clarno and Mitchell (Bestland and others, 1999; Appel, 2001), are interpreted to mark the lower boundary of the formation. Intermediate calc-alkaline rocks exposed in north central Oregon form a tight cluster of ages between 43.86 ± 0.89 and 41.50 ± 0.48 Ma (Bestland and others, 1999; Appel, 2001; McClaughry and Ferns, 2007) and are suggestive of a separate magmatic pulse. Urbanczyk (1994) described a similar age (43.5 ± 0.4 to 36.7 ± 0.2 Ma, lower Clarno) magmatic pulse in rocks correlative with the Clarno Formation in the eastern part of Oregon and a secondary pulse between 37.6 ± 0.4 and 33.6 ± 0.3 Ma (Upper Clarno of Urbanczyk, 1994). The formation can be traced in outcrop from south of Prineville to the north and northeastern along the Blue Mountains uplift, and to areas north of John Day (Fig. 3). Estimated maximum thicknesses are around 2000 m, but increase with proximity to volcanic centers (Bestland and others, 1999).

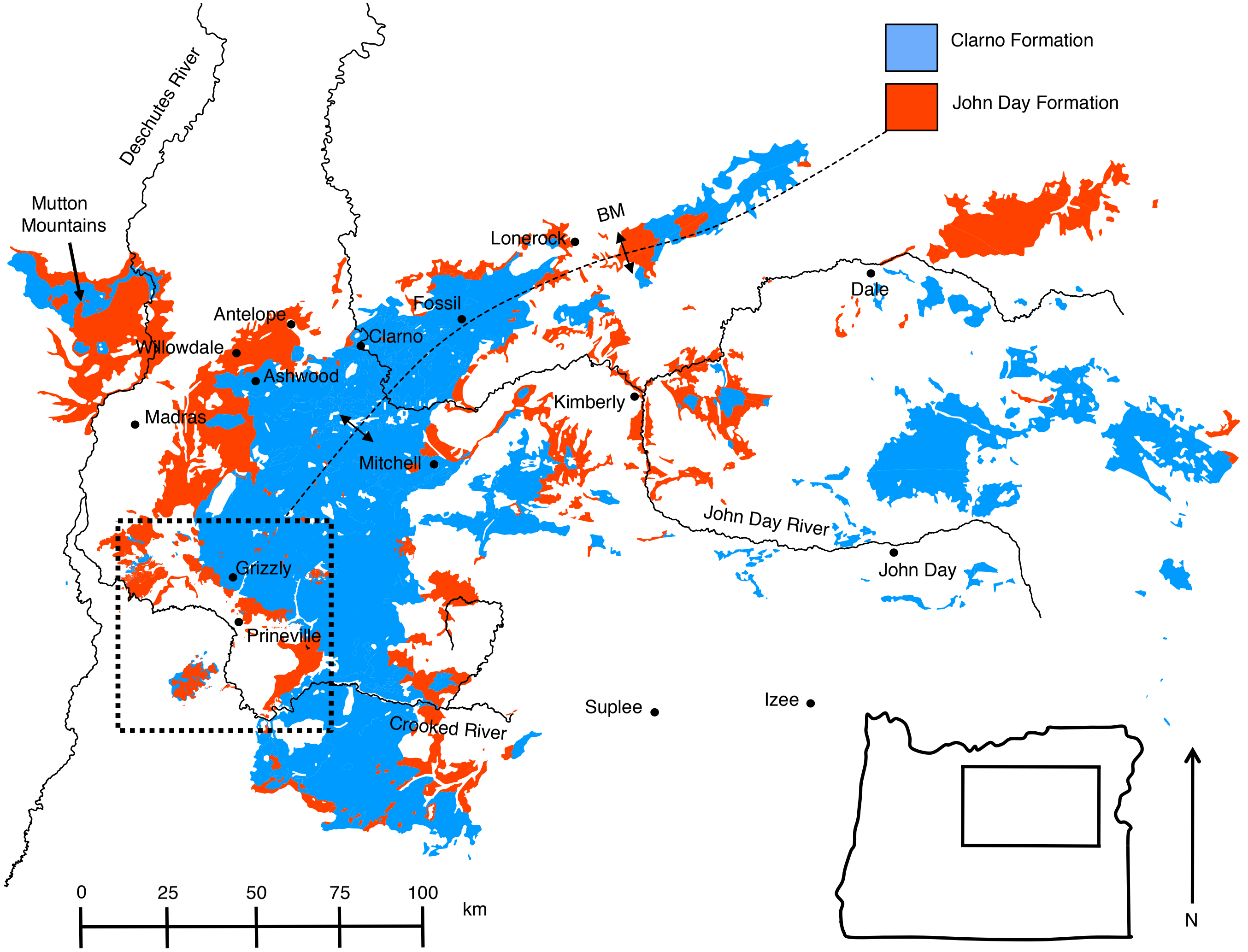

Figure 3.. Figure showing approximate outcrop distribution of Clarno and John Day Formations in central and eastern Oregon (After Walker and MacLeod, 1991; and McClaughry and Ferns, unpub. data). Black dashed box indicates approximate study area. BM = Blue Mountain Antline.

Transition to John Day volcanism

The transition from Clarno to John Day volcanism is usually inferred to have occurred around ~40 Ma based on a date of 39.17 ± 0.15 Ma (Smith and others, 1998) for the member A ash flow (Peck, 1964) of the JDF, which rest on andesites and breccias of the Clarno Formation. However, stratigraphic, compositional and age evidence suggests Clarno activity overlapped with John Day volcanism. Trachyandesites and alkali olivine basalts are common in the lower part of the JDF and upper part of the Clarno Formation (Peck, 1964; Robinson, 1969, 1975; Robinson and others, 1990), and volcaniclastics common in the JDF are locally abundant in the Clarno Formation. There also appears to be a compositional gradation from Clarno rocks, which show a mix of both calc-alkaline and alkaline affinities (Robinson, 2006), to John Day rocks that lack calc-alkaline affinities. Urbanczyk (1994) noted these mixed compositions in eastern Clarno rocks, but also provided Clarno ages (37.6 ± 0.4 and 33.6 ± 0.3 Ma) that overlap with John Day ages. Additionally, the recently mapped Wildcat Mountain caldera (~40 Ma, McClaughry and others, 2009) in the Blue Mountains of eastern Oregon, which straddles the Clarno-John Day boundary (39.17 ± 1.4 Ma, Smith and others, 1998), is composed of a basement of porph/yritic andesite typical of the Clarno Formation, but has rhyolitic caldera outflow lobes temporally correlative to the member A tuff (McClaughry and others, 2009).

These similarities suggest the transition from Clarno to John Day volcanism was gradual. The compositional variations are likely a function of source rock(s) and local and/or regional tectonics. Paleomagnetic studies by Gromme (1986) of Clarno andesites indicate 15.7°± 9.5° of clockwise rotation may have contributed to Eocene-Oligocene extension and John Day volcanism. However, as shown by Wernicke (1987) the Blue Mountains region is known to have experienced extension during the Eocene and Oligocene as a result of being caught between a right lateral shear regime in the northern Cordillera and an E-W extension regime of the Basin and Range province. Taylor (1990) suggested a change in vector orientation may have contributed to slower convergence rates between the Farallon and North American plates between 40 - 35 Ma and 35 Ma and ~20 Ma, which in turn resulted in slab steepening, repositions of the arc at or near its current location and development of a back arc setting in central Oregon. However, this assumes that the current Cascade arc was established by John Day time.

The John Day Formation

The JDF (39-20 Ma) covers at least 100,000 km^2 and perhaps as much as 225,000 km^2 of central and eastern Oregon (John Day magmatic region of Christiansen and Yeats, 1992). It consists of rhyolitic ash flow tuffs, domes and lavas, primary and reworked fall out tephra, and mafic lavas. It generally lacks intermediate compositions like those of the Clarno Formation, and consists more of a bimodal basalt-rhyolite assemblage. It is divided into three facies (Robinson and Brem, 1981) across central and eastern Oregon: (1) an eastern facies that lies east of the Blue Mountains uplift, (2) a southern facies that outcrops to the south and west of the Ochoco Mountains and (3) a western facies that is exposed in between the Blue Mountains uplift and Cascade Range (Fig 4).

The eastern and southern facies are similar in lithology, consisting of mostly of air fall tuffs and tuffaceous sedimentary rocks. The formation in the eastern facies was first described and subdivided by Merriam (1901) for outcrops along the John Day River

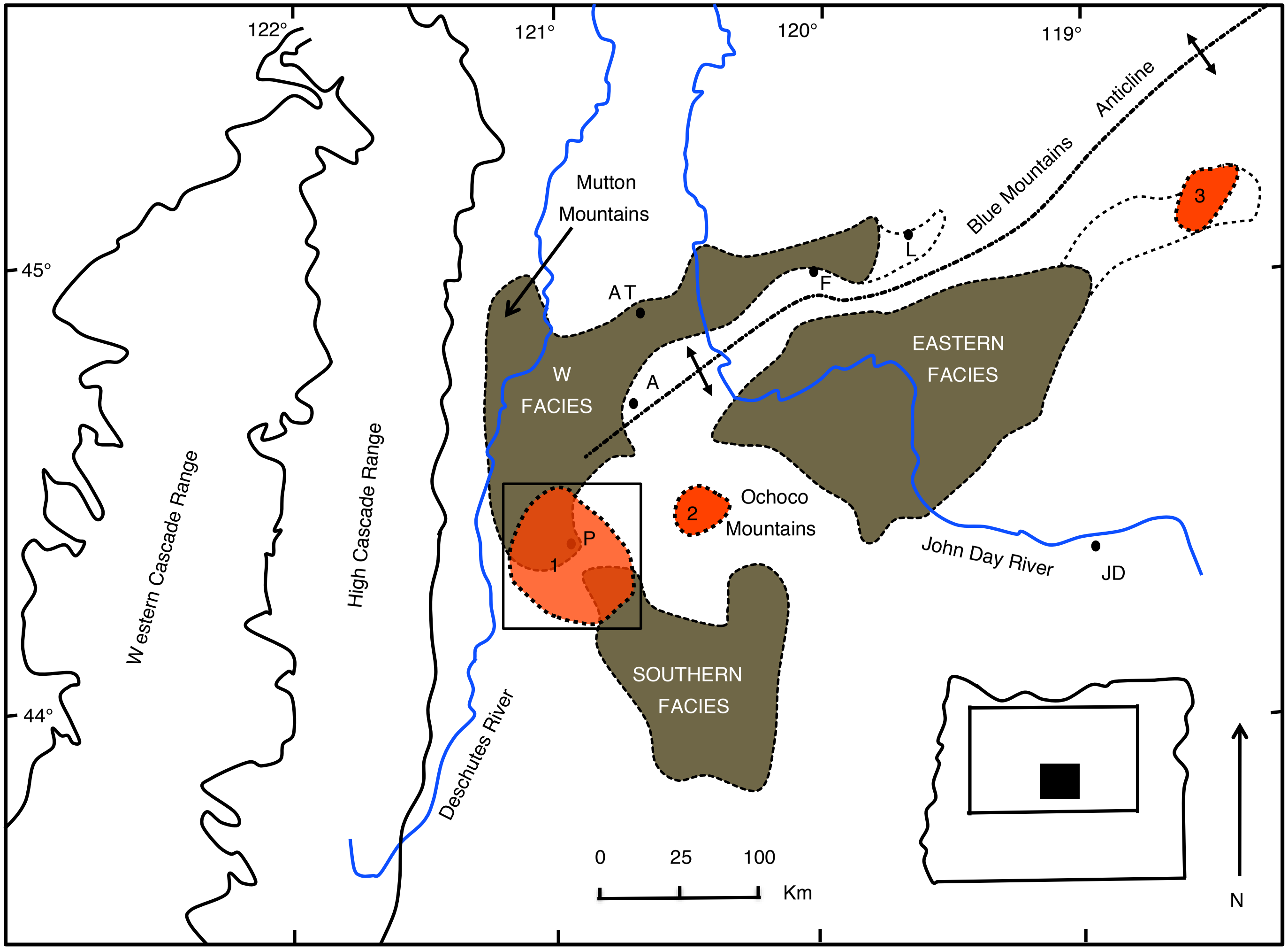

Figure 4. Index map showing extend of John Day facies in central and eastern Oregon. Dashed lines enclose areas of known outcrop, dotted lines enclose areas where rocks of probable John Day age are present (After Robinson and Brem, 1981; Robinson and others, 1984; Robinson and others, 1990). Black box indicates approximate study area. Abbreviations are as follows: AT = Antelope; A = Ashwood; W = Willowdale; F = Fossil; L = Lonerock; P = Prineville; JD = John Day. Red circles correspond to Paleogene caldera in the region; 1 = Crooked River caldera (29.5 Ma; McClaughry and other, 2009); 2 = Tower Mountain caldera (28.5 Ma, McClauhgyr and others, 2009); 3 = Wildcat Mountain caldera (40 Ma, McClaugry and others, 2009).

and later revised by Hay (1963) who proposed a 3-fold division based on the Picture Gorge Ignimbrite, which lies near the center of the formation. Fisher and Rensberger (1972) later divided the formation into four members, which from bottom to top include the (1) Big Basin Member (red claystones), (2) Turtle Cove Member (green and buff tuffaceous claystone and Picture Gorge Ignimbrite of Fisher, 1966a), (3) Kimberly Member (massive tuff beds) and (4) Haystack Valley Member (tuffaceous conglomerates). The southern facies lacks formally defined members, but is similar to the eastern facies and contains two informally named ash flow tuffs (lower and upper tuffs of Robinson and others, 1990).

The western facies was divided by Peck (1964) in members A-I based on ledge-forming ash flow tuffs and mafic lavas in the area between Ashwood and Willowdale in north-central Oregon. This subdivision, with only minor additions, is valid over most of the western facies except in the area between Lonerock and Fossil, and the Mutton Mountains (Robinson, 1975). The member A ash flow tuff (Peck, 1964; 39.17 ± 0.15 Ma, Smith and others, 1998) rests on andesites and breccias of the Clarno Formation (Peck, 1964; Swanson, 1969; Robinson, 1975) and outcrops nearly continuously from Grizzly to the vicinity of Clarno, and as isolated outcrops along the crest of the Blue Mountains anticline (Robinson and Brem, 1981). In areas where member A is not present, some workers have relied on a red saprolite layer as a marker bed (Hay, 1962a&b, 1963; Fisher, 1964). However it is rather unreliable, as similar layers appear at several levels in the JDF and only represent localized unconformities and the layer is not present in all exposures.

The western facies has been described as being lithologically coarser grained, containing minor mafic lavas and abundant rhyolite ash flows compared to the eastern facies (Robinson and others, 1990). However, new mapping and geochemical sampling reveals the ash flow tuffs are more widespread than originally thought. The Blue Mountains anticline likely did serve as a topographic barrier during John Day time (Robinson and others, 1984, Robinson and Brem, 1981; Robinson and others, 1990), but its role in confining ash flow deposition is somewhat unclear, as the timing of uplift is poorly constrained.

Cross correlations between the western and eastern facies are limited. Robinson and Brem (1981) proposed the correlation of member A in the western facies to a small outcrop of a basal ash flow tuff (Robinson, 1975) in the eastern facies, and member G in the western facies to an air fall tuff in the eastern facies based on mineralogy. However, additional information such as radiometric dates, and trace element geochemistry are lacking and could test these correlations. In more recent years, numerous dates from ash flow and air fall tuffs in the John Day Fossil Beds National Monument, as well dates from mapping by the Oregon Department of Geology and Mineral Industries (DOGAMI) have helped establish a regional framework with which to start improving regional correlations. However, more detailed geochemical work is needed.

Sources for JDF

Past workers have suggested the JDF pyroclastic rocks were erupted from vents in or near the current Cascade Range (Robinson, 1975; Robinson and Brem, 1981; Robinson and others, 1984; Bestland and others, 1999), and/or from isolated Oligocene rhyolite domes like Powell Buttes, Juniper Butte, Grizzly Mountain that are scattered throughout central and eastern Oregon (see Figure 5; Swanson, 1969; Robinson and Brem, 1981; Robinson and others, 1984, 1990). Robinson and others (1990) suggested the air fall tuffs were likely the result of coeval early Cascade volcanism, while the ash flow tuffs were products of local eruptions between the Cascade Range and Blue Mountains. They also pointed out the wide range of compositions and ages for the ash flow tuffs, and concluded that they had to be products of multiple sources. Recent mapping and reconnaissance work by McClaughry and others (2009) have identified John Day-age calderas well east of the Cascade Range that were likely sources for some of the major ash flow tuffs and primary and reworked tuffs in the JDF.

Oligocene "Ignimbrite Flareup"

John Day volcanism is coincident with other silicic Oligocene volcanics in the region. For example, the Pike Creek Volcanic Series (Fuller, 1931) and several unnamed volcanic and volcaniclastic rocks exposed in Lake County (units Tsf and Tr from Walker and MacLeod, 1991) on the Oregon-Nevada border in the Basin and Range province. Thick accumulations of Oligocene ash flow tuffs near Eugene Oregon indicate caldera-forming eruptions were also occurring in southwestern Oregon during this time (Retallack and others, 2004). Moreover, the numerous volcanic fields of the Great Basin throughout Nevada and western Utah (Best and Christiansen, 1991) also overlap with John Day volcanism. This widespread magmatic event throughout much of the western United States has been regarded as an "ignimbrite flare-up"; a distinct type of volcanism, in which large volumes of silicic magma (10^6 km^3) are erupted within short time frames (~10 Ma, Armstrong and Ward, 1991). The cause for these types of events is still under debate; though the general model suggests they represent crustal modulation of a mantle derived thermal pulse, which influences how long volcanism occurs on the surface, how much material is erupted, and the composition of that material (Armstrong and Ward, 1991; Humphreys, 1995; Lipman and Glazner, 1991). In the southwest United States, in the Basin and Range province this event has generally been attributed to post-Laramide removal of the Farallon plate (Humphreys, 1995), as evidenced by large volumes of very low velocity upper mantle (Grand, 1994, Humphreys and Decker, 1994a) near the base of the crust (Hearn and others, 1991). However the manner in which the slab was removed is still under debate.

Past Work Relevant to this Study

The John Day-age rhyolitic ash flow tuffs, domes and lavas investigated in this study are centered on the town of Prineville (Figure 2 and 3). Geographically they are part of the western and southern facies and the majority of them are temporally equivalent to member G of the western facies based on similar age, composition, and stratigraphic position. The units include rhyolitic ash flow tuffs and mafic lavas that preceded caldera collapse and syn- and post-caldera rhyolitic ash flow tuffs, domes and lavas

Previous work on these John Day-age ash flows south of the original field area investigated by Peck (1964) is limited and of little detail, except in areas of Smith Rock State Park and Gray Butte near the western edge of the Blue Mountains uplift (Fig 4). Williams (1957) originally mapped this area as part of the John Day Formation, while Robinson and Stensland (1979) mapped the area as a southward dipping section of Clarno rocks onlapped by JDF ash flow tuffs. They considered neither the Tuff of Smith Rock nor Gray Butte Rhyolite as belonging to the Clarno or John Day Formations.

Obermiller (1987) assigned both the Gray Butte Rhyolite and Tuff of Smith Rock a mid-Miocene age based on whole rock K-Ar ages and suggested they were part of an eruptive center.

Smith and others (1998) were the first to correlate the Gray Butte Rhyolite and Tuff of Smith Rock, as well as other age-equivalent ash flows in the Gray Butte/Smith Rock area to the original division of the western facies of JDF near Antelope and Ashwood (Peck, 1964). They assigned the Tuff of Haystack Reservoir (29.53 ± 0.09 Ma, 29.57 ± 0.17 Ma), Tuff of Smith Rock (29 ± 3 Ma) and the Gray Butte Rhyolite (28.82 ± 0.23 Ma) to member G based on age, and noted northeast to southwest increases in thickness within the western facies. They too like Obermiller (1987) suggested the Gray Butte/Smith Rock area was part of a major eruptive complex, but considered it Oligocene in age. They also recognized the Cyrus Spring Fault Zone (CSFZ) as a substantial mid-Tertiary fault that may represent reactivation along the Klamath-Blue Mountain lineament (Riddihough, 1986).

Further detailed studies of these rocks have been inhibited by the lack of detailed geologic mapping and sampling, defined stratigraphy, and geochemical and geochronological data. Reconnaissance mapping by Robinson (1975) assigned outcrops in the Madras-Antelope-Clarno area to members A-I (Peck, 1964) and designated new units not previously defined. Robinson and Brem (1981) noted upper and lower unnamed rhyolite tuffs south of Prineville in the southern facies, but did not correlate them to ash flow tuffs in the western facies. Robinson and others (1990) later dated the lower tuff (Tuff of Eagle Rock) at 32.1 ± 0.7 Ma, temporally equivalent to the 32.49 ± 0.30 Ma Tuff of Rodman Spring that Smith and others (1998) assigned to member F of the JDF.

McClaughry and others (2009) correlated intermediate basaltic andesite lavas exposed at Prineville Reservoir to member B trachyandesites (unit Tjb of Robinson, 1975) based on similar petrography and chemistry (Robinson, 1975; Robinson and Brem, 1981; Robinson and others, 1990). Evans and Brown (1981) dated a similar basaltic andesite flow at 30.1 ± 1.1 Ma from a geothermal well just west of Powell Buttes (Brown and others, 1980).

Geologic mapping by the Oregon Department of Geology and Mineral Industries (DOGAMI) of the Lower Crooked Basin has lead to clarification of previously recognized units, as well as recognition of new units and their distribution. Based on geochemistry, structure, stratigraphy and ages of these John Day-age rhyolitic ash flow tuffs, domes and lavas and associated mafic lavas, McClaughry and others (2009) identify them as a discrete eruptive package (Lower Crooked Volcanic Field, LCVF) that formed in association with the early Oligocene Crooked River caldera (29.5 Ma, McClaughry and Ferns, 2007). Based on age, these eruptive products are temporally equivalent to member G of the JDF in the Antelope-Ashwood area originally defined by Peck (1964). This project aims to geochemically characterize the eruptive outflow, caldera fill and post-caldera rhyolite domes that formed as a result of the Crooked River caldera eruption, investigate their petrogenesis and improve the understanding of John Day volcanism.

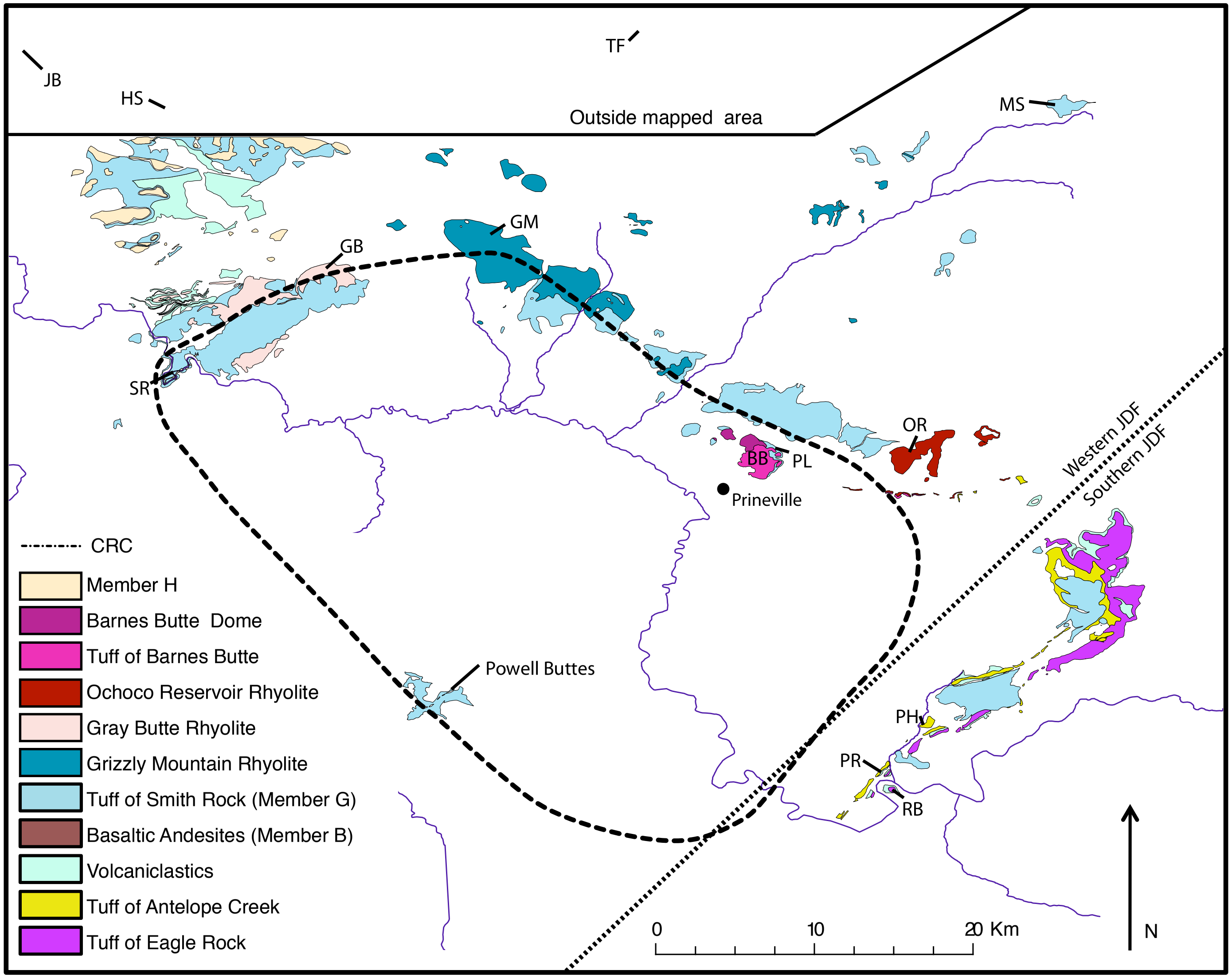

Figure 5. Geologic map showing locations where units were sampled.
HS = Haystack Reservoir State Park;
TF = Teller Flat;
MS = McKay Saddle;
GB = Gray Butte;
SR = Smith Rock State Park; OR = Ochoco Reservroir
GM = Grizzly Mountain;
BB = Barnes Butte;
PL = Peppermint Lane;
GG = Gravy Gulch;
PH = Paulina Highway;
PR = Prineville Reservoir State Park; RB = Roberts Bay State Park.
JB = approximate location of Juniper Butte.
Rock units sampled in the study are given in the key. The Smith Rock Tuff and other age equivalent outflow units of JDF member G have been mapped as one unit. Member G units sampled at Haystack Reservoir State Park and Teller Flat are outside mapped boundaries.

Stratigraphy and Unit Descriptions

A geologic map of the study area and outcrop locations is shown in Figure 5. Refer to Appendix E for UTM sample locations. Regional correlation of these John Day ash flow tuffs has been largely piecemeal over the years, due to a lack of geologic mapping, sampling and age dates, as well as the localized nature of their distribution. A generalized stratigraphy of the units based on available dates and stratigraphic relations is shown in Figure 6.

Precaldera Stratigraphy

Tuff of Eagle Rock

The Tuff of Eagle Rock (32.1 ± 0.7 Ma, lower tuff of southern JDF facies of Robinson and others, 1990) exposed at Prineville Reservoir State Park (Fig. 7) consists of a mottled yellow-white, strongly welded, poorly feldspar-phyric, pumice-lithic tuff with rheomorphic features that is up to 50 m thick along the banks of the Prineville Reservoir. It is tilted to the northwest (McClaughry and Ferns, 2007) back towards the inferred Crooked River caldera margin (McClaughry and others, 2009) and may represent syn-caldera collapse deformation. In thin section spherulites and axiolites of feldspar and quartz are abundant indicating extensive post-emplacement alteration. To the northeast of Prineville Reservoir at Eagle Rock, the tuff displays ramp features suggestive of remobilization and rheomorphism, as well as lithophysal cavities filled with vapor phase minerals.

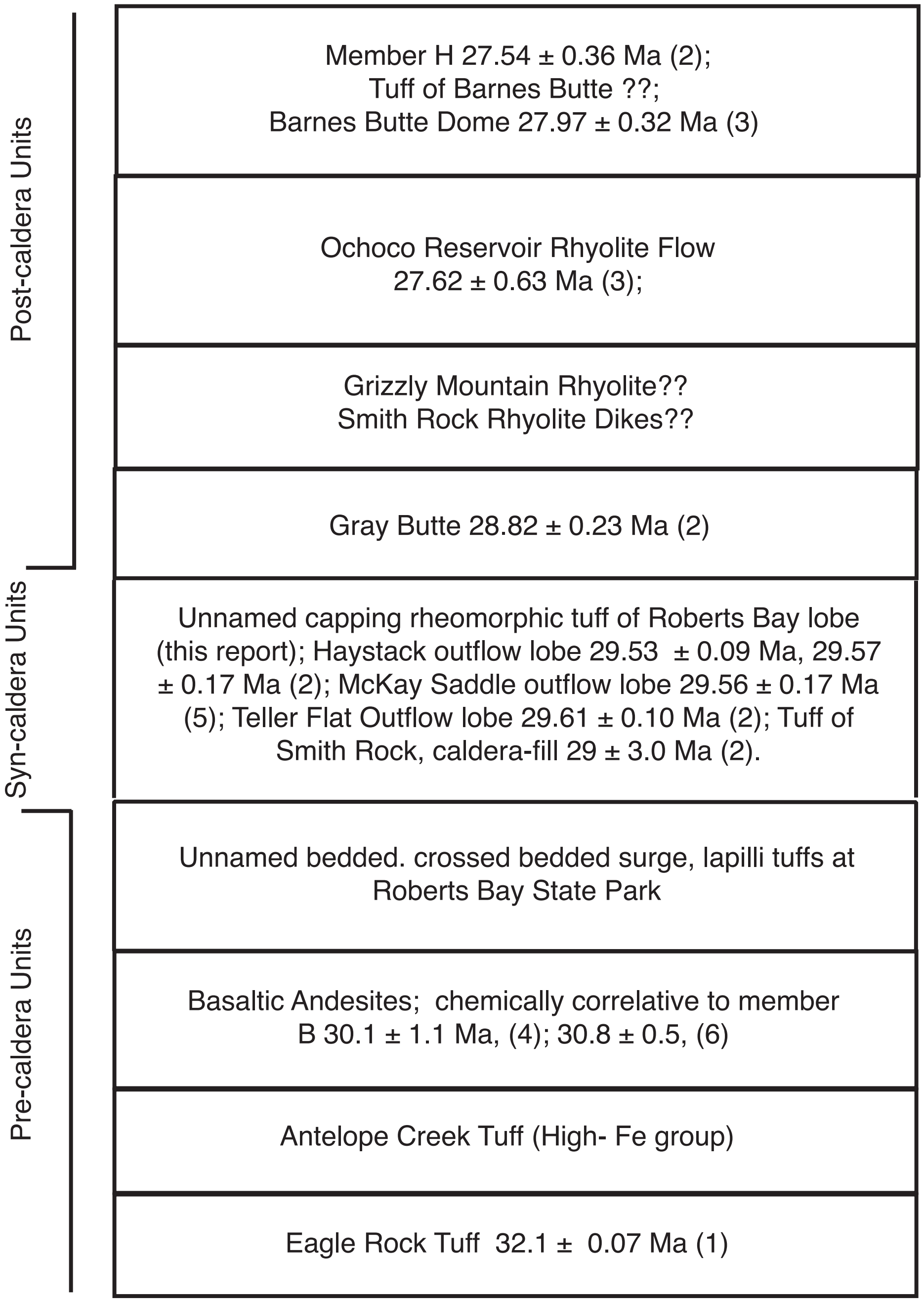

Figure 6. Diagram showing general stratigraphy of John Day age units in relation to formation of the Crooked River Caldera. References are as follows: (1) Robinson and others, 1990; (2) Smith and others, 1998; (3) McCluahgry and Ferns, 2006a; (4) Evans and Brown, 1981; (5) McClaughry and others, 2009; (6) Fiebelkorn and others, 1983.

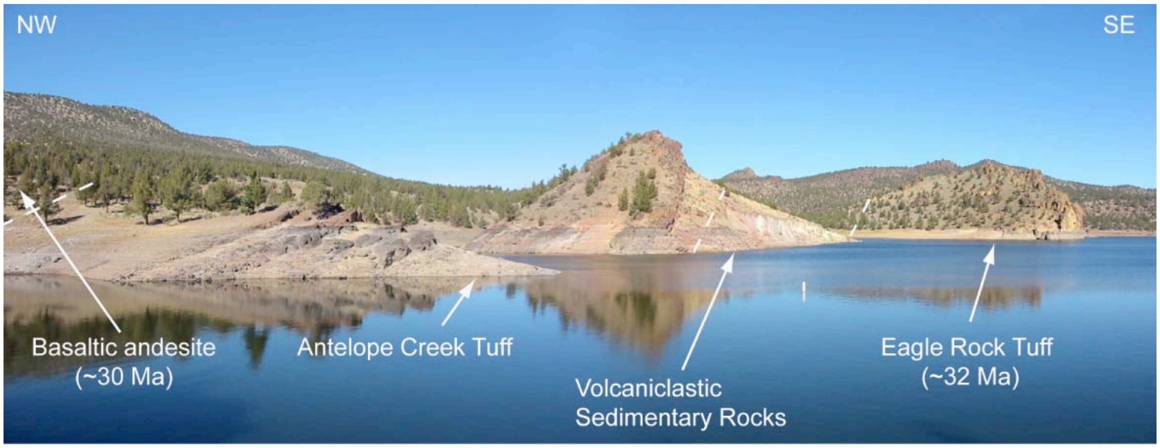

Figure 7. Prineville Reservoir section to the SE of the Crooked River caldera. From top to bottom basaltic andesite, Antelope Creek Tuff, volcaniclastic sedimentary rocks and Eagle Rock Tuff. Note NW dip towards the Crooked River caldera (From McClaughry and others, 2009).

Figure 8. Section of Tuff of Antelope Creek exposed along Paulina Highway. Note lower dark gray welded tuff and upper brownish red welded tuff. Notebook for scale = 13 cm.

Tuff of Antelope Creek

The Tuff of Antelope Creek conformably overlies volcaniclastic sedimentary rocks and the Tuff of Eagle Rock at Prineville Reservoir State Park (Fig. 7), and consists of a 25-30 m section of dark red to purplish gray moderately welded crystal pumice lithic tuff. Sparse phenocrysts of sanidine and plagioclase and clay altered fiammé are set in a groundmass of devitrified glass shards. Mafic lithics are abundant and appear to increase in size up-section.

The Tuff of Antelope Creek is also exposed along the Paulina Highway (UTM 687905 E 4897654 N, Fig. 8) and at Gravy Gulch (688070 E 4901620 N). Along the Paulina Highway the unit conists of 2-3 m of moderately welded tuff that varies upsection. The lower part of the tuff consists of a moderately welded vitric pumice lithic tuff with sparse sanidine and plagioclase crystals and lithic fragments of obsidian, basalt and andesite in a eutaxic groundmass of fine ash (Fig. 9). Banded pumice fragments range in size from a few mm to 2 cm, and are flattened into glassy fiammé. Upward the tuff becomes mottled peach and gray and moderately to poorly welded and crystal content decreases, while lithic and pumice size and content increases. Light gray phryic and dark aphyric lithic fragments range from a few mm to 2 cm. Faulting of this unit at this location is evident by a zone of pervasively altered tuff in the center of the outcrop, and is interpreted to be part of the Prineville Reservoir Fault Zone (McClaughry and others, 2009). At Gravy Gulch (688070 E 4901620 N) the Tuff of Antelope Creek consists of a reddish moderately to strongly welded pumice-poor lithic-rich rhyolitic tuff with sparse phenocrysts of feldspar and spherulitic and axiolitic fiammé in a groundmass

Figure 9. Micrographs under plane light of lower welded tuff from the Tuff of Antelope Creek exposed at UTM 687905 E 4897654 N. (A) Eutaxtic texture with contorted glass shards, typical of moderately welded tuffs. (B) Spheroidal obsidian lithics and (C) sanidine and mafic lithics.

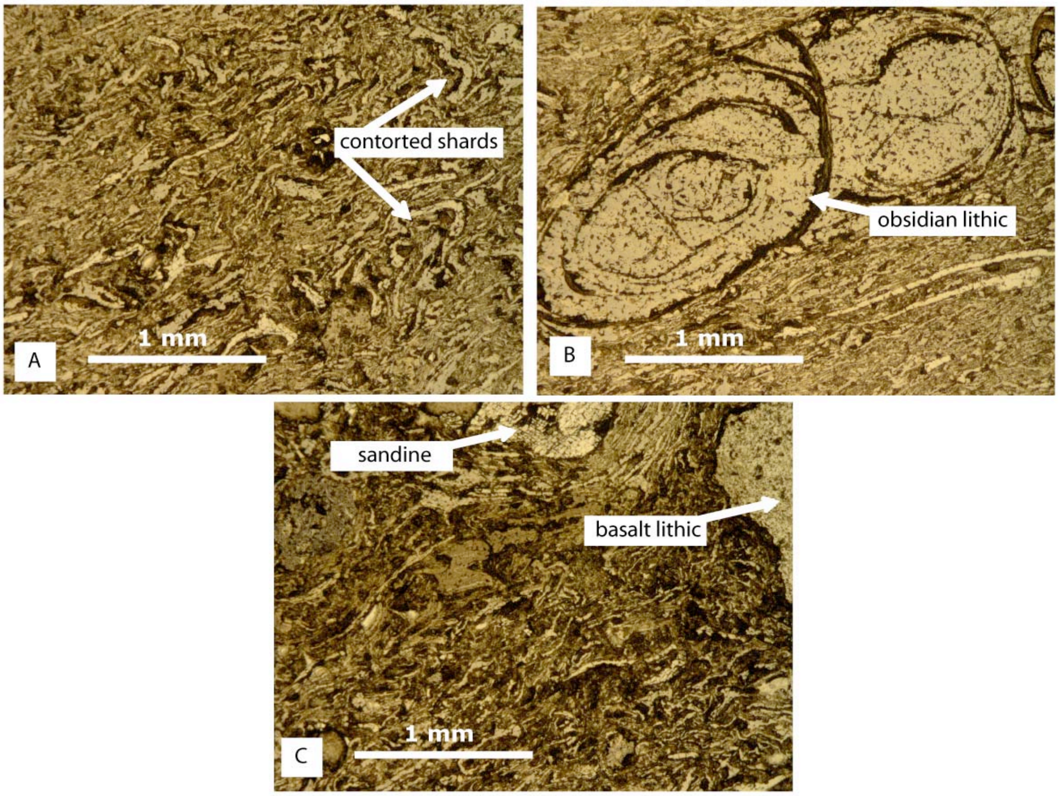

Figure 10. (A) Micrograph of basaltic andesite under crossed polarized light showing aligned plagioclase laths and low birefrigence yellow microgranular clinopyroxene throughout the groundmass. (B) Micrograph under plane polarized light showing altered olivine phenocryst. Fe-oxide minerals are black cubes and have been circled.

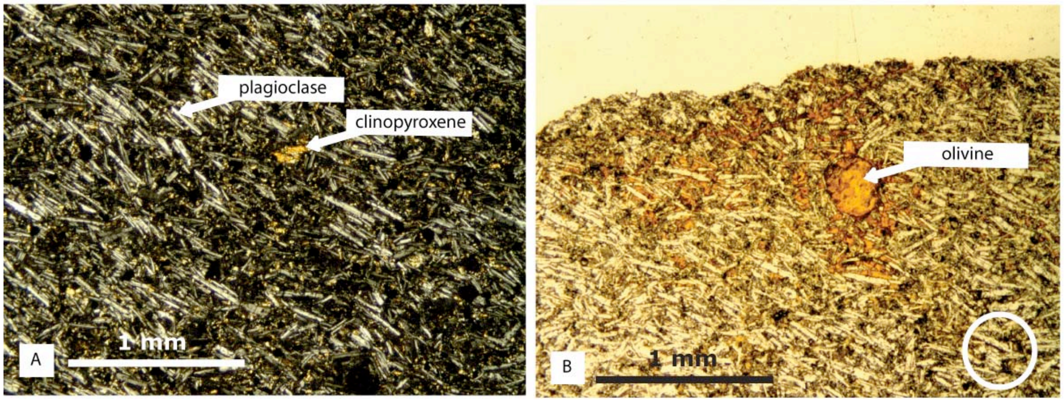

of devitrified glass shards. Lithic fragments of aphyric andesite and rhyolite are quite abundant and range from 0.5 cm to 1.5 cm. Overlying this tuff is a gray vitric moderately welded rhyolite ash flow tuff with bimodal pumice correlative to the Rattlesnake Tuff (Walker, 1977; Streck and Grunder, 1995).

Basaltic Andesites

Basaltic andesites exposed at Prineville Reservoir overlie the Tuffs of Eagle Rock and Antelope Creek and range in thickness from 30 to 45 m. They are gray to black, sparsely plagioclase-phyric with microgranular clinopyroxenes, cubic iron oxides and interstitial glass in a groundmass of aligned plagioclase laths (Fig. 10a). Phenocrysts of olivine are rare and are usually altered to iddingsite (Fig. 10b). These basaltic andesites are compositionally similar to a 30.1 ± 1.1 Ma (Evans and Brown, 1981) basaltic andesite encountered in a geothermal well west of Powell Buttes and member B basaltic andesites (30.8 ± 0.5 Ma, Robinson and others, 1990) exposed near Gray Butte (Smith and others, 1990). Although no basalts were sampled or found at Prineville Reservoir during this study, olivine-phyric Fe- and Ti-rich tholeiites are interbedded with these intermediate lavas north and west of Gray Butte (Smith and others, 1998). Additionally, Robinson (1969) described some tholeiitic to alkaline olivine basalts exposed in north central Oregon.

<u>Unnamed Units At Roberts Bay State Park</u>

Exposed on the southern shore of Prineville Reservoir at Roberts Bay State Park is a thick section of pyroclastic flows, surge deposits, and volcaniclastic rocks reaching thicknesses of at least 150-200 m (Fig 11A). Basal outcrops of basaltic andesites

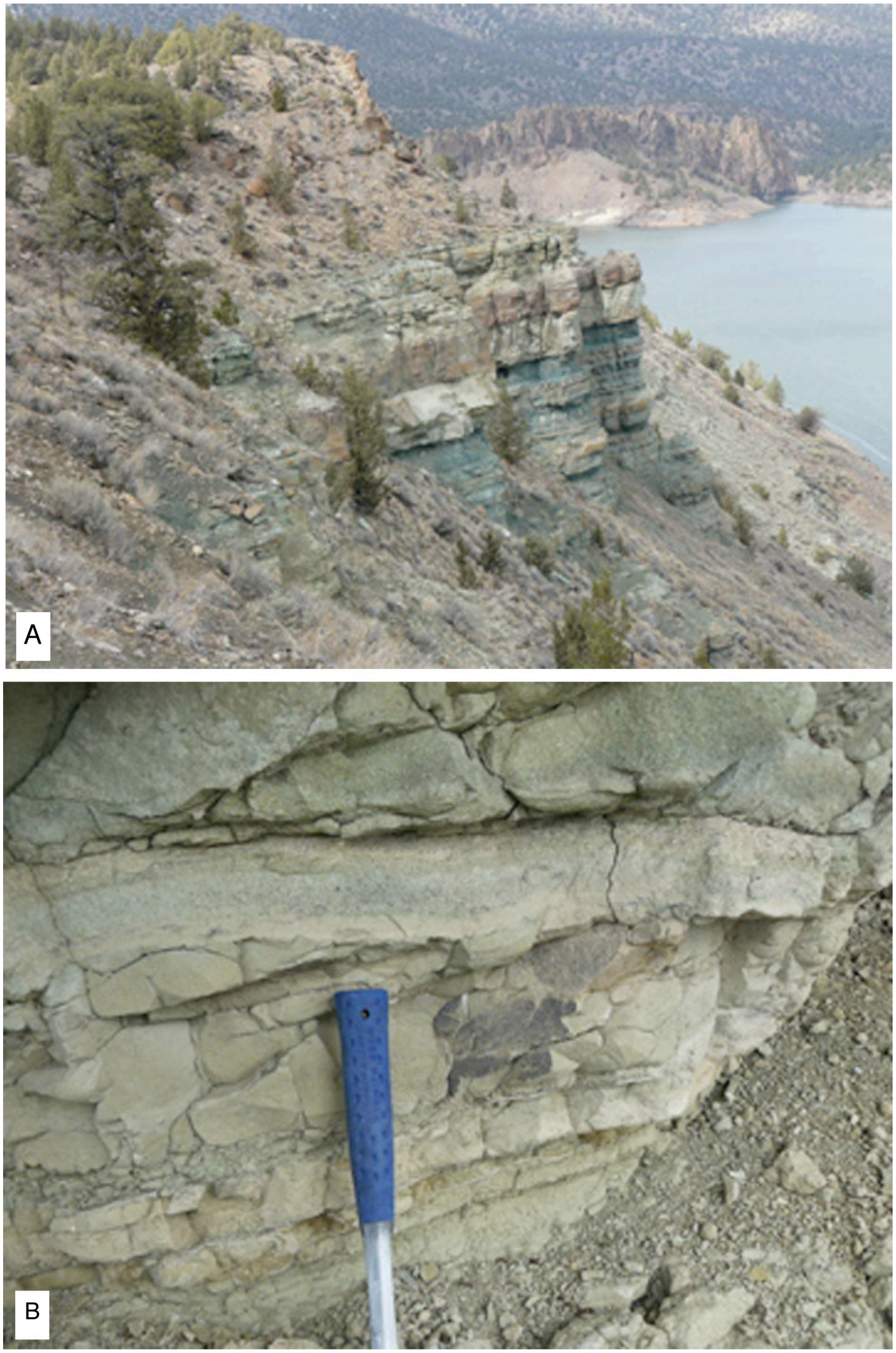

Figure 11. (A) Large section of unnamed welded and non-welded, lapilli tuffs and surge deposits exposed at Roberts Bay State Park. (B) Outcrop of bedded surge deposits.

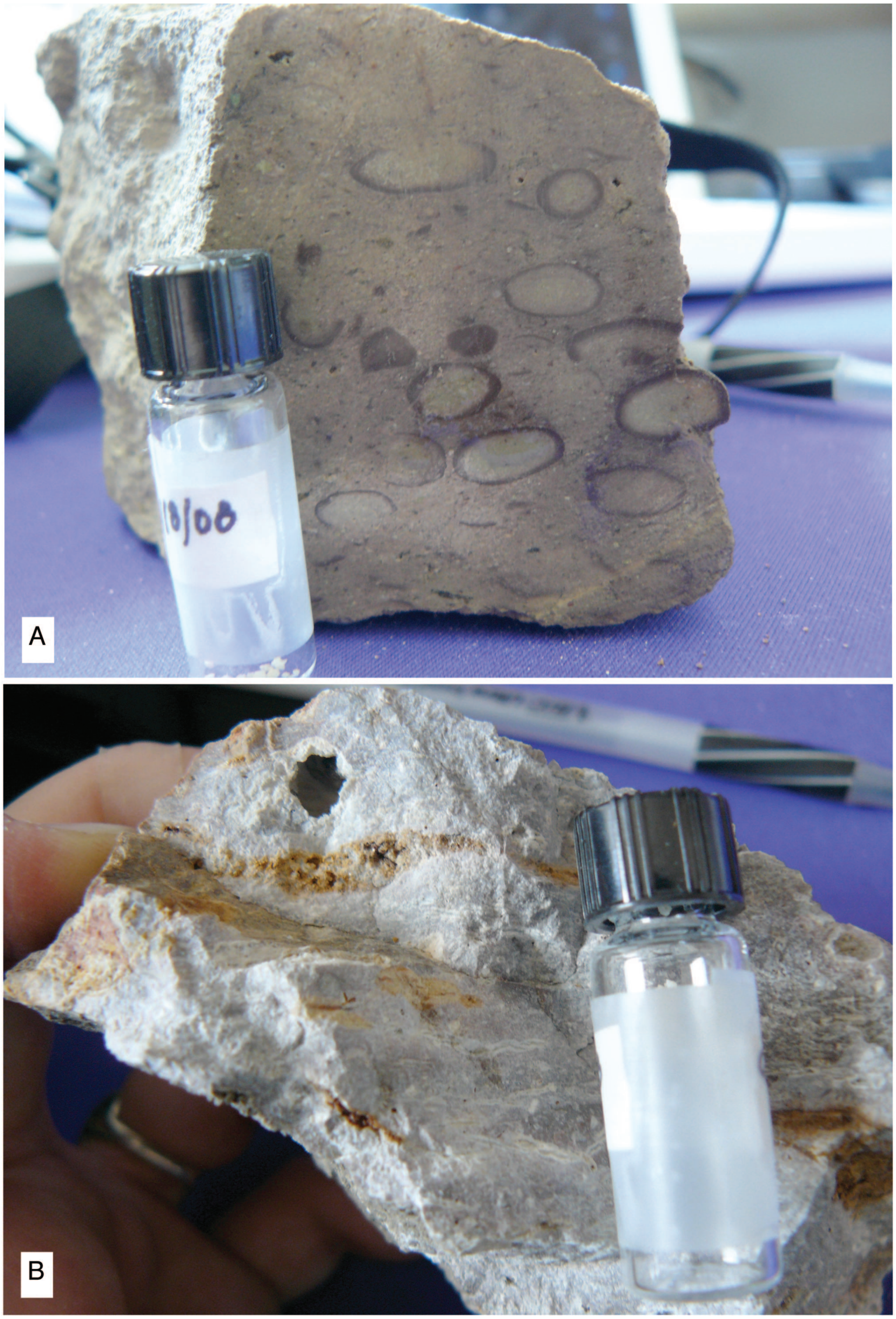

Figure 12. (A) Hand sample of accretionary lapillli tuff from Roberts Bay State Park. (B) Hand sample of capping rheomorphic densely welded tuff at Roberts Bay State Park showing recrystallized fiamme and lithophysal cavities. Note vial equals approximately 4 cm.

lithologically and chemically identical to the basaltic andesites previously described are succeeded upwards by emerald green interbedded welded and nonwelded pumice- lithic-rich- and poor- lapilli-tuffs, air fall and bedded surge deposits (Fig. 11B & 12A). Prior to this study this section of tuffs had not been previously recognized, thus its relation to caldera formation is unclear, and more detailed sampling and mapping is needed to characterize the numerous lithologies. The section is capped by a relatively flat lying dark red densely welded to rheomorphic rhyolite ash flow with recrystallized fiammé and clay-altered feldspars. Lithosphysal cavities have been partially filled with vapor phase minerals (Fig. 12B). McClaughry and Ferns (2006a) interpret the capping rheomorphic ash flow as correlative to the Tuff of Eagle Rock. However, based on its stratigraphic position above the basaltic andesites, and chemical similarities with the Tuff of Smith Rock, this capping tuff is here reinterpreted as the Roberts Bay outflow lobe from the 29.5 eruption of the Crooked River caldera.

Syn-caldera units: Caldera fill and outflow

The Tuff of Smith Rock intracaldera fill and its equivalent outflow units are exposed at several locations within and surrounding the inferred caldera (see Fig. 5) margin. McClaughry and others (2009) interpret these units temporally equivalent to member G based on age, chemistry, structure and stratigraphy.

Intracaldera Fill

The largest exposures of the Tuff of Smith Rock intracaldera fill are at Smith Rock State Park (Fig. 13). At the park the tuff is a massive case-hardened tan unstratified rhyolitic pumice rich tuff, though gently dipping zones (<5°) of fine ash and lithic

Figure 13. View from Smith Rock State Park looking towards Gray Butte Rhyolite Dome. Foreground consists of the Smith Rock Tuff intracaldera fill, with Gray Butte in the background.

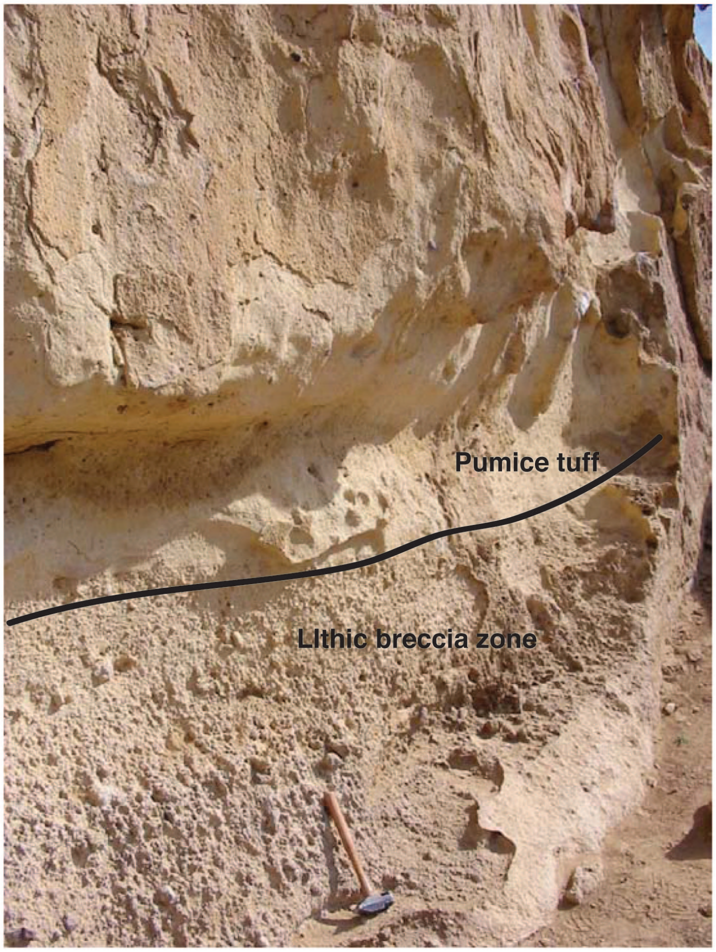

Figure 14. Lithic lag breccia lenses in Smith Rock Tuff at Smith Rock State Park. Note hammer for scale = 1.5 ft.

lenses are common. The lithic lenses are interpreted as lithic lag breccias (Fig. 14) indicative of pulsating pyroclastic flows close to the vent source, and commonly contain basaltic, rhyolitic and limestone lithics ranging in size from a few cm to 18 cm. The presence of limestone lithics indicates the Crooked River caldera erupted through pre-Tertiary marine basement rocks. Locally the tuff is light green and maroon from zeolitic alteration, and all primary material is altered or has recrystallized. McClaughry and others (2009) estimate minimum thicknesses of 0.5 km for the tuff and note high-angle contacts of the tuff against pre-caldera rocks along the margin of the caldera. A fission track date (zircon) reported by Smith and others (1998) dates the Tuff of Smith Rock at 29 ± 3.0 Ma, well within the age dates for member G of the JDF, though more precise age data are needed to constrain and improve this correlation.

Additional intracaldera fill tuff is exposed at a roadcut (UTM 671472 E 4911016 N) on Peppermint Lane within the city of Prineville. At this location the tuff is a light olive green pumice- and lithic-rich tuff, pumices altered to clay ranging in size from a few mm to 6 cm (Fig. 15). Devitrified cuspate glass shards are set in a matrix of clay altered fine ash (Fig. 16A), and sparse sanidine phenocrysts commonly have overgrowth textures (Fig. 16B). Lithic fragments of mafic and felsic rocks are also common.

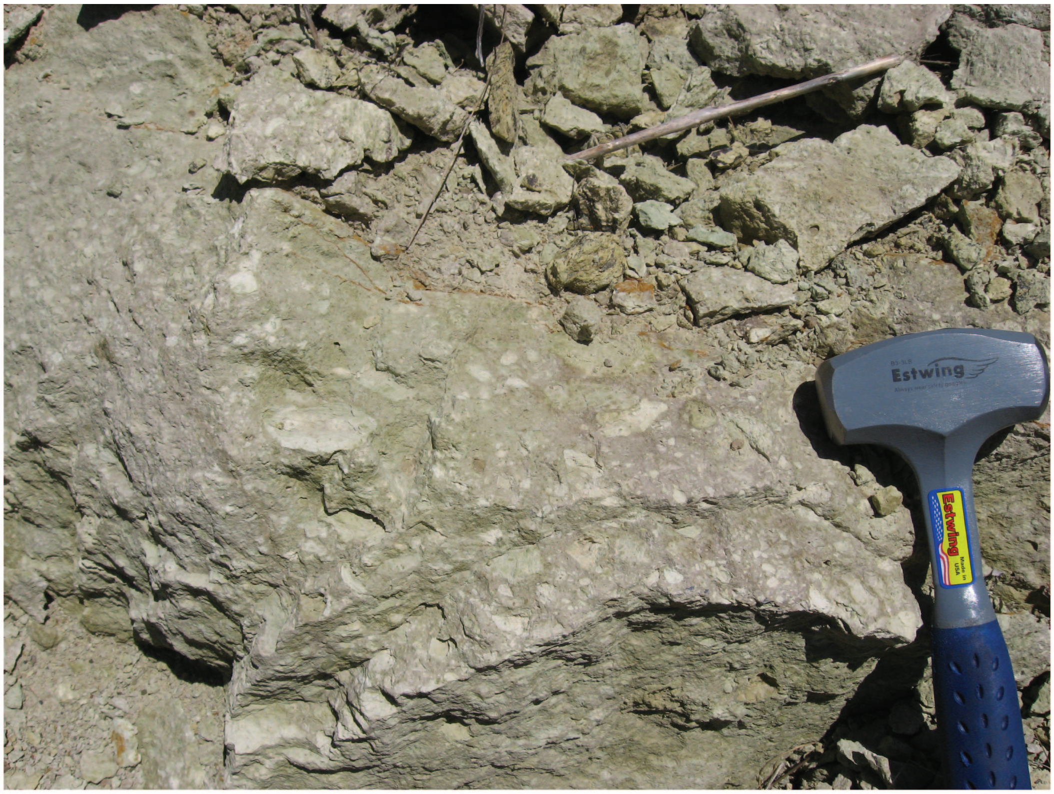

Figure 15. Smith Rock Tuff caldera fill exposed on Peppermint Lane. Note white clay atlered pumices and hammer for scale.

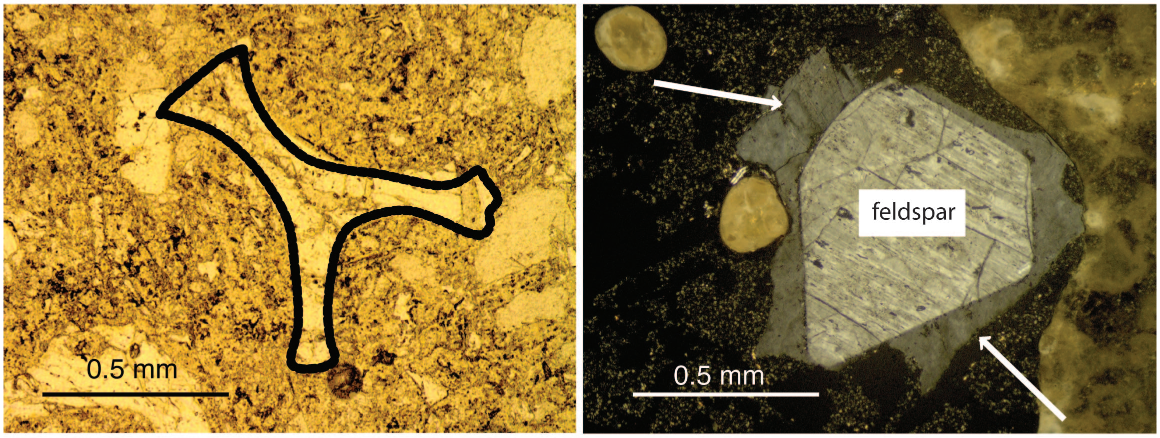

Figure 16. (A) Micrograph under plane polarized light showing outline of devitrified cuspate glassy shards in a matrix of fine ash atlered to clay. (B) Micrograph under crossed polarized light showing secondary grain overgrowth on feldspar set in a matrix of fine clay-altered ash.

Caldera Outflow

Haystack Reservoir lobe

The Haystack Reservoir lobe consists of as much as 30 m of rhyolitic ash flow tuff divided into at least three distinct cooling units (Fig. 17) separated by plane- and cross-bedded nonwelded pumice lithic tuff suggestive of hydromagmatic surge and air fall. Smith and others (1998) were first to formally name, describe and correlate these tuffs to Member G of the JDF, while later work by McClaughry and others (2009) has interpreted these tuffs as outflow from the 29.5 Crooked River caldera eruption.

The lowest ash flow consists of reddish to brown densely welded crystal lithic tuff with large recrystallized fiammé (Fig 18B) that are commonly rimmed with axiolites composed of quartz. Sparse phenocrysts of plagioclase, sanidine and quartz with embayed and resorbed edges indicative of disequilibrium textures are set in a devitrified groundmass of glass shards (Fig. 17A). Lithic fragments of flow-banded rhyolite are also abundant. The presence of slickensides indicates faulting during the formation of the Cyprus Springs Fault Zone (Smith and others, 1998). The middle tuff (29.57 ± 0.17 Ma, Smith and others, 1998) is less strongly welded and consists of plagioclase, sanidine and quartz crystals with embayed and resorbed edges, as well as secondary grain overgrowths. Pumices are commonly devitrified to axiolitically-arranged crystals and lithics of flow-banded rhyolite are common. Vitric float collected near 0647436 E, 4928915 N, likely represents vitrophyres from either the lower or middle welded ignimbrite, but was not exposed in outcrop.

The upper tuff at Haystack Reservoir consists of an orange to red poorly welded pumice tuff that exhibits pumice poor- and rich-zones and is capped with a lithophysal

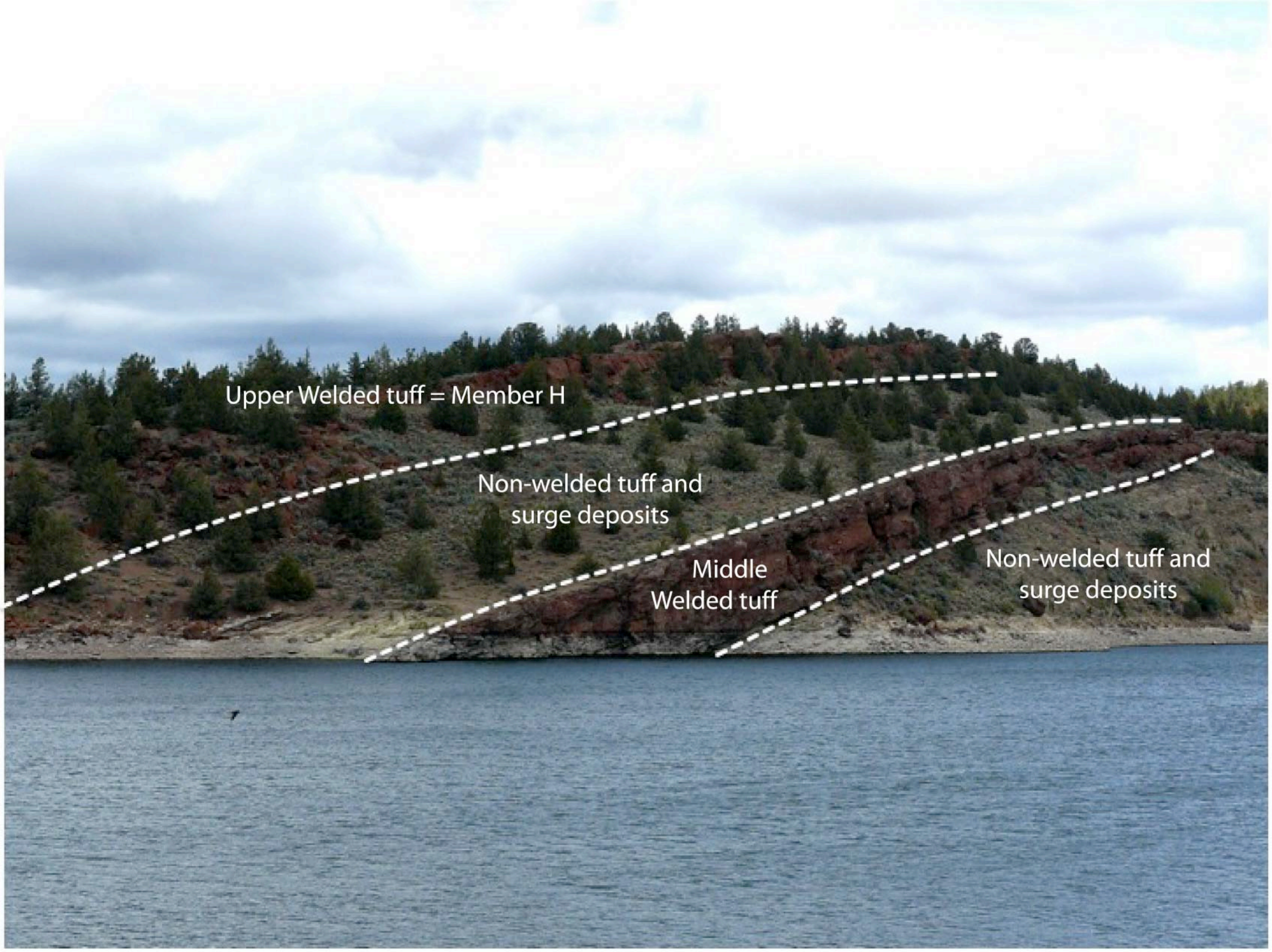

Figure 17. Section of welded and non-welded, bedded and non-bedded tuffs and surge deposits exposed at Haystack Reservoir State Park. The lower welded tuff is not shown in this photo.

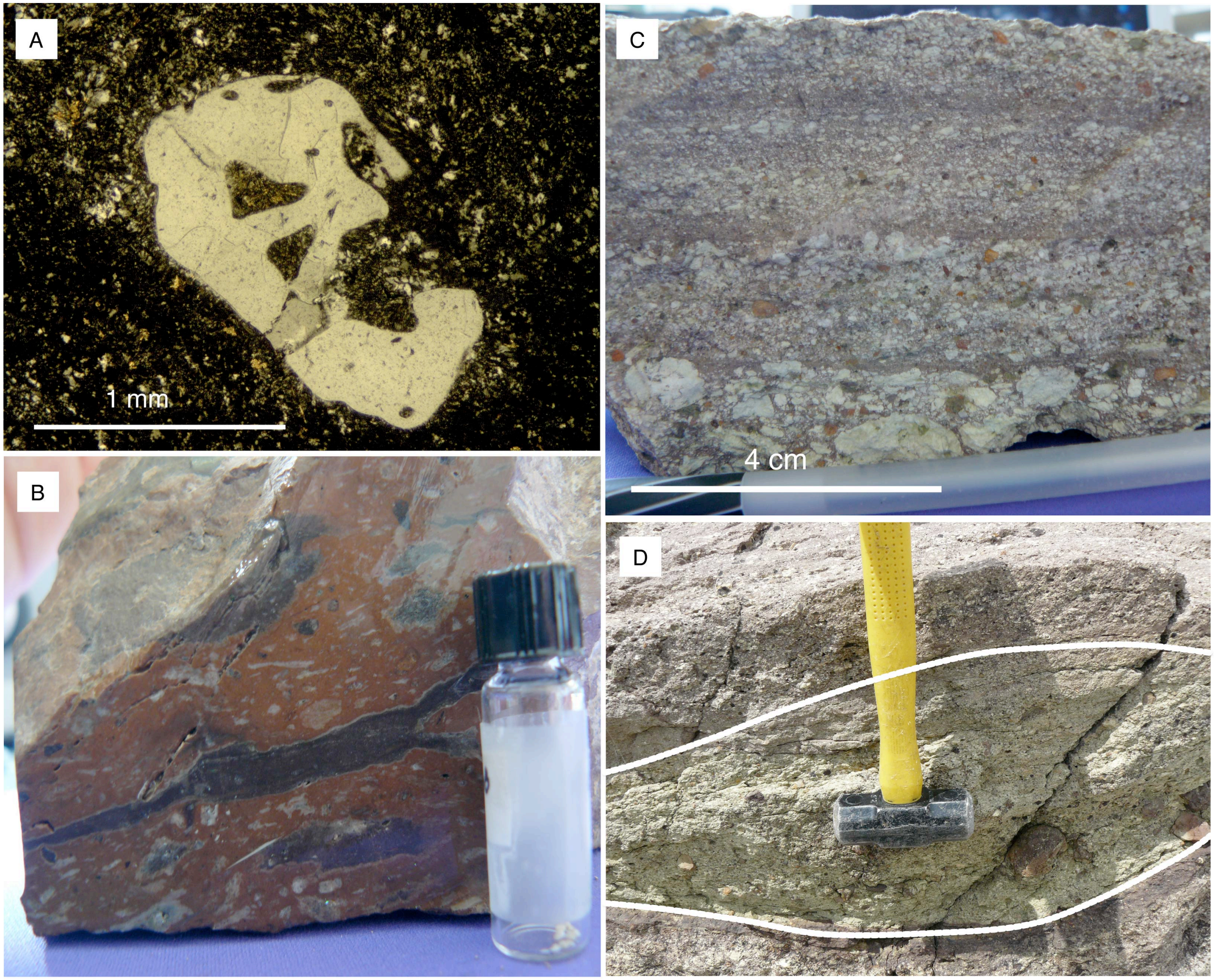

Figure 18. (A) Micrograph under crossed polarized light showing embayed quartz phenycryst in recrystallized ground mass; (B) Hand sample of lower welded tuff of Haystack Reservoir showing recrystallized fiamme (vial = 4 cm); (C) Hand sample of bedded non-welded tuff at Haystack Reservoir showing pumice poor and rich layers. Note reddish color from the incorporation of soil from the underlying soil zone; (D) Pinch and swell features observed in interbedded non-welded tuff and surge deposits at Haystack Reservoir State Park. Note hammer for scale.

zone. Smith and others (1998) interpret this upper tuff as equivalent to Member H of the JDF based on age (27.62 ± 0.63 Ma, Smith and others, 1998).

The interbedded nonwelded pumice lithic tuffs (29.53 ± 0.09 Ma, Smith and others, 1998) contain light olive green to cream colored clay-altered pumice in a pale red groundmass that was likely incorporated in the unit from the underlying red soil zone. Phenocrysts of sanidine and quartz have resorbed and embayed edges, and some display zoning. Lithic fragments of spherulitic devitrified glass, flow banded rhyolite and pyroxenes altered to chlorite are common. Within these tuffs are crystal- and lithic-rich zones and fine ash layers (Fig. 18C). The crystal- and lithic-rich zones share common constituents with the nonwelded tuffs, containing resorbed and embayed sanidine crystals and quartz, and lithic fragments of spherulitic glass, clay-altered pumice, and chlorite. Additionally they contain flow banded rhyolite lithics as noted in the two welded tuffs. They also contain large amounts of oxidized material incorporated from underlying soil zone, which indicates the flow scoured the underlying soil zone during transportation and subsequent emplacement. Based on horizontal- and cross-bedding of the tuffs, (2) pinch and swell features (Fig. 17D) and (3) discrete grading from pumice poor to pumice rich regions (Fig. 17C) these interbedded deposits are suggestive of hydromagmatic surge, indicating water may have been present during the eruption. This interpretation is consistent with Smith and others (1998) who determines this area was a subsising basin during John Day time.

McKay Saddle lobe

The McKay Saddle lobe consists of a 120 m thick compound section of tuff that is poorly exposed NE of Prineville in the Ochoco National Forest (see Fig. 5). The base

(~67 m) consists of a densely welded vitric-pumice-lithic-crystal tuff with pumice fragments, sanidine phenocrysts and lithics of phyric spherulitic obsidian and grades upward into a fresh partially welded obsidian tuff (~18 m) with obsidian fragments with devitrified rims (Fig. 19). Up-section the unit consists of a gray moderately welded, lithic-crystal tuff (~12 m) with obsidian, rhyolite, and andesite lithics in a devitrified groundmass. The section is capped by a tan, non-welded crystal rich tuff with blocky sanidine and small pyroxene phenocrysts in a matrix of fine ash that is only exposed as float along and west of McKay Saddle. McClaughry and others (2009) correlate these units to Member G of the JDF based on a 29.56 ± 0.17 Ma age (McClaugry and others, 2009) and interpret them as outflow from the Crooked River caldera based on stratigraphic position, similar age, and chemistry.

Teller Flat lobe

The Teller Flat lobe is located northeast of the Haystack Reservoir lobe on a plateau region (see Fig. 5). The Teller Flat section ranges from 6-10 m (Fig. 20) and consists of a brown to red crystal rich nonwelded lithophysal locally fumarolically altered rhyolite tuff with large sanidine phenocrysts and lithic fragments of olivine-bearing andesite in a microlitic groundmass of fine ash now altered to clay. Feldspars commonly have grain overgrowths and are intergrown with quartz. Smith and others (1998) assigned this tuff to member G of the John Day Formation based on 29.61 ± 0.10 Ma age (sample GSO95-144, Smith and others, 1998).

Figure 19. Capping perlitic tuff in the outflow exposed at McKay Saddle on the NE margin of the Crooked River caldera.

Figure 20. Section of outflow at Teller Flat on the northern margin of the Crooked River caldera.

Post-caldera units: rhyolite domes, dikes and flows

Following the collapse of the Crooked River caldera, numerous rhyolite domes, dikes and flows geochemically similar the Tuff of Smith Rock were emplaced along the caldera margin and within the caldera.

Gray Butte Rhyolite Dome

Located to the northeast of Smith Rock State Park, the Gray Butte Rhyolite Dome (28.82 ± 0.23 Ma age, Smith and others, 1998) is composed of the Gray Butte Rhyolite (Fig. 13). Previous investigators (Wiliams, 1957; Robinson and Stensland, 1979; Obermiller, 1987; Smith and others, 1998; Sherrod and others, 2004) regarded the Tuff of Smith Rock conformable upon the Gray Butte Rhyolite, but recently mapped high angle contacts between the Tuff of Smith Rock and the Gray Butte Rhyolite by McClaughry and others (2009) indicate the Gray Butte Rhyolite intrudes the Tuff of Smith Rock. The presence of highly altered contacts between the tuff and the rhyolites also indicate post-tuff intrusion of the Gray Butte rhyolite dome. Obermiller (1987) and Smith and others (1998) describe a perlitic vitrophyre at the base of the dome, but no such unit was found in this study. The Gray Butte Rhyolite consists mostly of a tan to gray massive to flow banded semi-phyric rhyolite with altered feldspars in a microgranular groundmass of feldspar and clays. Sample GB353 in particular has feldspar, pyroxene and Fe-Ti oxide glomerocrysts (Fig. 21A&B). McClaughry and others (2009) interpret the Gray Butte Rhyolite as a ring fracture rhyolite dome associated with the Crooked River caldera based on chemistry and age, as well as the high angle and highly altered contacts between the tuff and the rhyolite.

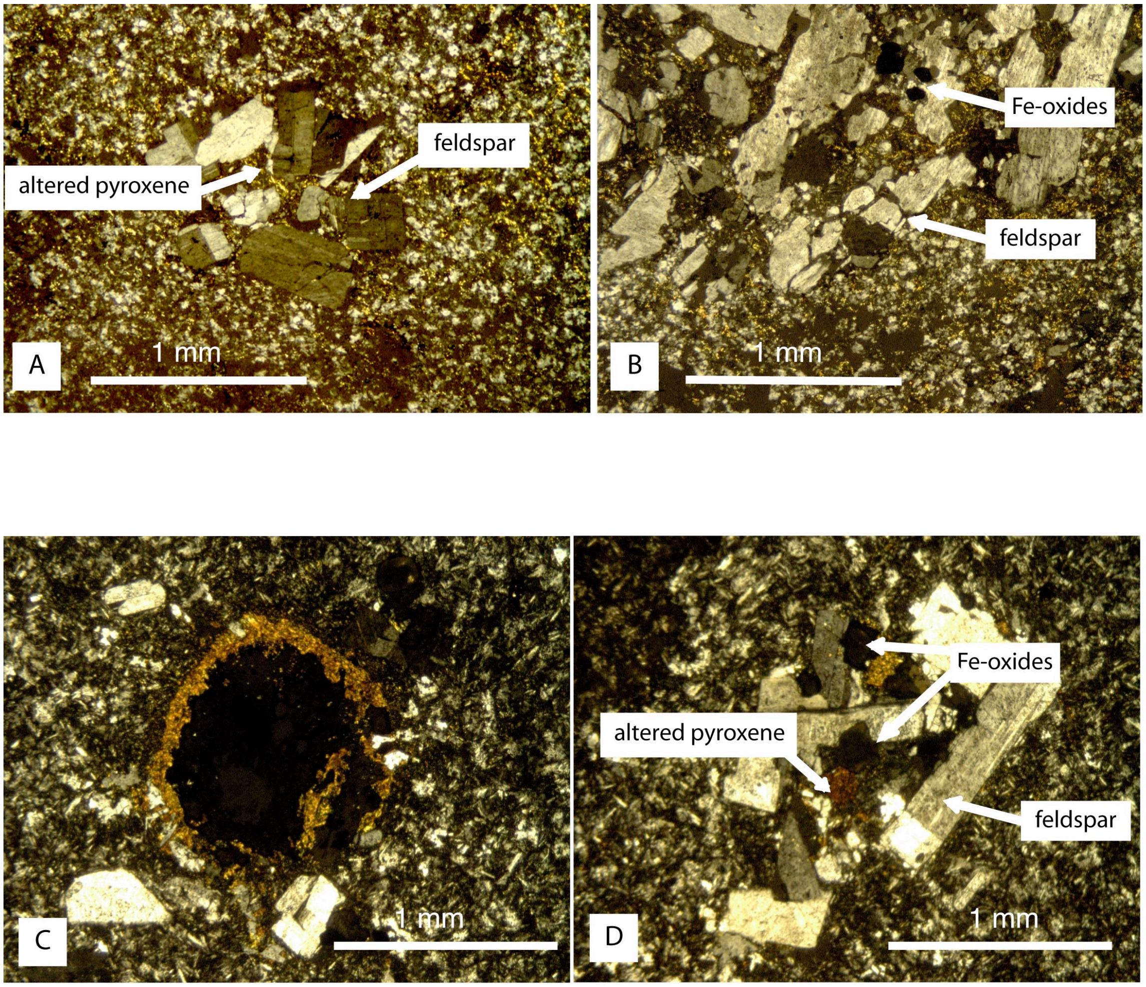

Figure 21. Micrographs (A) and (B) under crossed polars showing feldspar, clinopyroxene and Fe-Ti oxide glomerocrysts in sample 353 of the Gray Butte Rhyolite Dome. Note seive disequilibrium texture in slide (B). Micrographs (C) and (D) under crossed polars showing olivine altered to iddingsite and (D) glomerocrysts of feldspar, clinopyroxene and Fe-Ti oxides in sample SR11 from the Smith Rock State Park rhyolite dikes.

Rhyolite Dikes

Intruding the Tuff of Smith Rock within the confines of Smith Rock State Park are numerous light gray sparsely-phyric rhyolite dikes with vertical flow banding (Fig. 22). Quartz grains are set in a microlitic to sometimes-spherulitic groundmass containing feldspar and quartz. The dikes' intermingled appearance within the tuff suggests it intruded in an anastomosing style (Bishop, 1989) and vesicular zones along the tuff-rhyolite contact suggest the dike may have been emplaced prior to complete degassing of the tuff, thus implying the dikes likely formed not long after collapse of the Crooked River caldera and emplacement of the intracaldera fill. One dike (sample SR11) differs significantly in lithology consisting of phenocrysts of oligoclase, sanidine and altered pyroxene, as well as glomerocrysts of feldspar, biotite altered pyroxene and iron oxides in a felted groundmass of feldspar and quartz (Fig. 21D). This difference in lithology is coupled with differences in major and trace element data that will be discussed later.

Grizzly Mountain Rhyolite Dome

The Grizzly Mountain Rhyolite Dome is located northwest of Prineville off Highway 26 (see Fig. 4). The unit is flow banded and consists of aphanitic regions of recrystallized material and coarser regions of quartz and alkali feldspar phenocrysts and trace apatite in a recrystallized spherulitic groundmass (Fig. 23). McClaughry and others (2009) interpret the Grizzly Mountain rhyolite as a ring-fracture rhyolite dome emplaced along the margin after collapse of the Crooked River caldera.

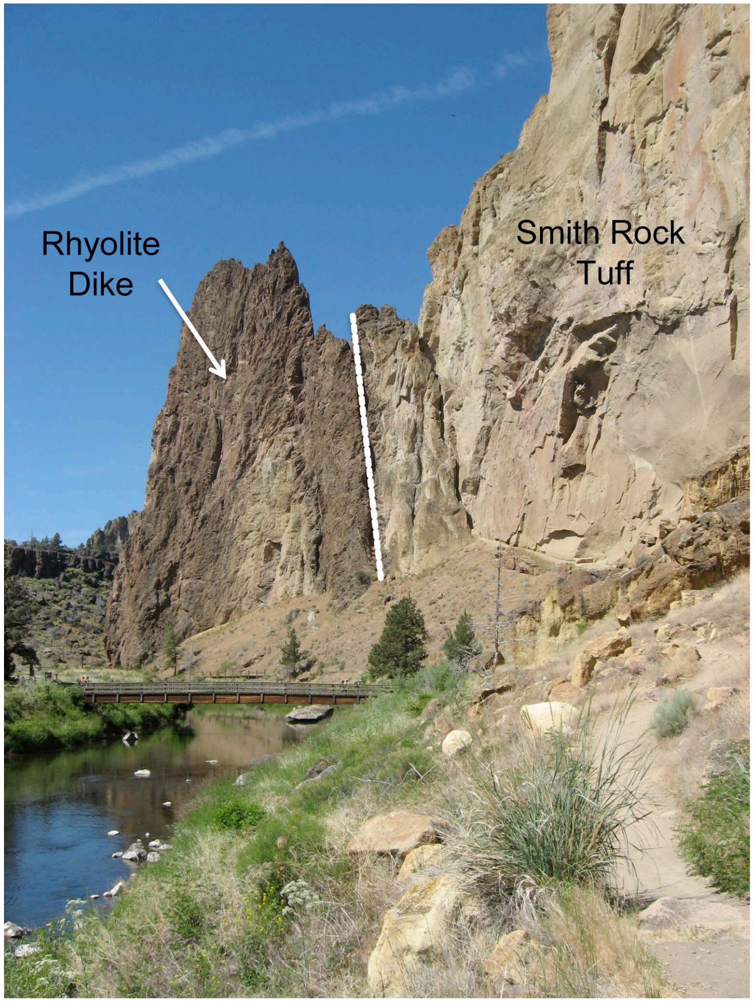

Figure 22. Smith Rock Tuff with adjacent rhyolite dike.

Figure 23. Hand sample showing flow banding in the Grizzly Mountain rhyolite dome (vial = 4 cm).

Barnes Butte Dome and Tuff

The Barnes Butte Dome (27.97 ± 0.32 Ma, McClaughry and Ferns, 2006a) intrudes southeast portions of the Tuff of Smith Rock intracaldera fill and consists of a grayish semi-phyric massive to flow banded rhyolite with sparse phenocrysts of sanidine set in a heavily silicified recrystallized groundmass. Feldspars have overgrowth textures, as well as embayed edges, and orthopyroxene, zircon, and apatite appear in minor amounts. Towards the southern part of the butte, the butte is capped by the Tuff of Barnes Butte, an ash-flow tuff erupted from within the southeastern confines of the Crooked River caldera between 29.56 and 27.97 Ma. The tuff consists of a pink to red moderately welded pumice lithic tuff, with flattened pumice, sparse crystals of sanidine and quartz set a matrix of glass shards with devitrified rims. Lithic fragments of dark red rhyolite and small mafic lithics are common. The rhyolite dome intrusion is geochemically indistinguishable from the Tuff of Barnes Butte, identifying this area as the eruptive source for the tuff. However it is not clear whether the eruption of the Tuff of Barnes Butte resulted in the formation of a collapse structure or from another type of vent structure. The Tuff of Barnes Butte in Prineville shares similar stratigraphic position, lithologic character, and geochemistry with Member H of the JDF, which suggests it may have erupted from within the confines or vicinity of the Crooked River caldera at ca. 28.5 Ma (McClaughry and Ferns, 2006a).

Ochoco Reservoir Rhyolite Flow

The Ochoco Reservoir Rhyolite flow is exposed on cliffs adjacent to the Ochoco dam. The unit consists of a red to purple flow banded phyric rhyolite flow containing sanidine and sparse clinopyroxene phenocrysts in a groundmass of microcrystalline quartz and feldspar (Fig. 24). Original glassy flow bands are completely recrystallized into spherulites and axiolites of quartz and feldspar. Original work by Waters and Vaughan (1968) identified the unit as a rheomorphic ash flow, but the lack of pumice or other pyroclastic textures suggests that it was emplaced as a lava flow that ponded in moat settings near the SE margin of the caldera (McClaughry and others, 2008), though no sources has been identified. A $^{40}Ar/^{39}Ar$ date of 27.54 ± 0.36 Ma for this unit is reported by McClaughry and Ferns (2006b). However, this age is discordant with the rhyolites position below the Tuff of Barnes Butte, which is intruded by the 27.97 ± 0.32 Ma (McClaughry and Ferns, 2006a) Barnes Butte dome.

Major, minor and trace element Geochemistry

A total of ~110 samples were collected from outcrops surrounding the town of Prineville from the localities shown in Figure 5. Of the samples, 75 were analyzed for major, minor and trace elements using X-ray flurorescence (XRF) and inductively coupled plasma mass spectrometry (ICPMS) using the methods of Johnson and others (1999), and Knaack and others (1994). Refer to the Washington State University Geoanalytical website (http://www.sees.wsu.edu/Geolab/note.html) for a summary of methods.

Mineral compositions were analyzed by electron microprobe. However, because of the degree of post-eruptive alteration, few fresh phenocrysts were found. Due to the low modal abundance of pyroxenes, samples were crushed and run through a 250-micron sieve, hand picked and placed on a grain mount. Unfortunately the freshness of the

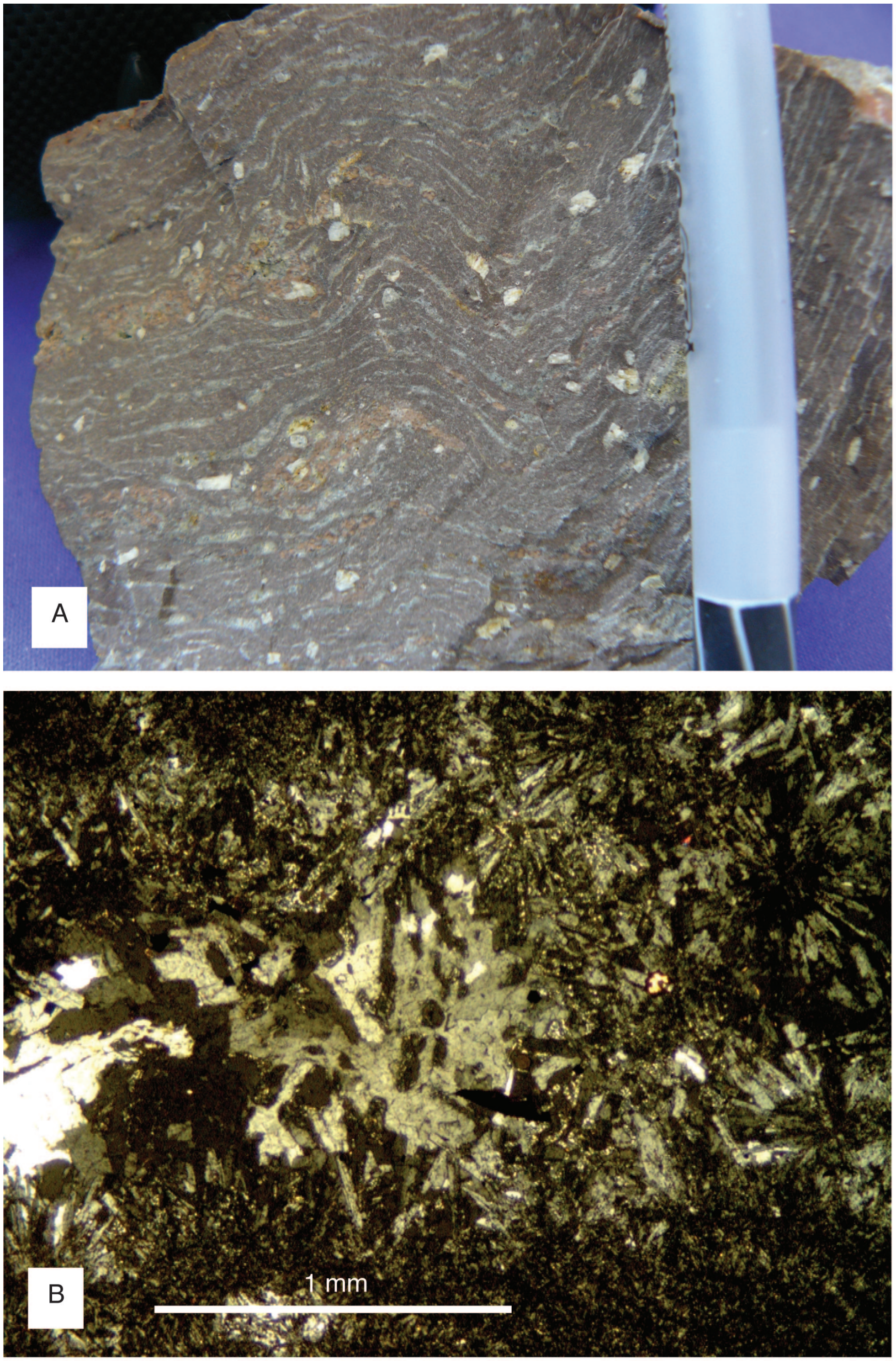

Figure 24. (A) Hand sample of phyric flow banded Ochoco Reservoir Rhyolite (pen = 3 cm). (B) MIcrograph under crossed polars of spherulites and axiolitic textures in Ochoco Reservoir Rhyolite.

pyroxenes was poor and probe data were restricted. Feldspar data were collected from polished thin sections, as well as mineral separates.

Pre-caldera Basaltic Andesites

The tholeiitic basaltic andesites exposed at Prineville Reservoir are the least evolved samples in the suite, with compositions similar to icelandites containing high FeO_T (11.0 - 14.0 wt %), low MgO (1.4-3.5 wt %) and SiO_2 contents ranging from 53.1-57.18 wt.%. Total alkalis ($K_2O + Na_2O$) range from 4.8 - 5.4 wt %, while CaO ranges between 7.6 – 6.3 wt %. Decreasing CaO, TiO_2, SiO_2 and Al_2O_3 and increasing K_2O versus MgO (Fig. 24) suggest pyroxene, plagioclase and Fe-Ti oxide fractionation. MELTS (Ghiorso and Sack, 1995) experiments were run at various various pressures and oxygen fugacities to test fractional crystallization of suggested phases; the melt composition curves are plotted on Fig 25. The models yielded results broadly consistent with pyroxene, plagioclase and Fe-Ti oxides fractional crystallization, though none of the conditions could mimic the FeO enrichment or high P_2O_5 variability. One possible explanation for FeO enrichment could be the accumulation of a Fe-rich phase like magnetite, though magnetite would also cause an increase in Ti. Thus, the other possibility is pyroxene. The presence of anhedral microgranular pyroxene (Fig. 10A) throughout the groundmass may be remnants of resorbed crystals that added Fe back into melt. The variable P_2O_5 content suggests (1) variable fractionation, retention and accumulation of apatite, (2) a variety of parental magmas, or (3) P mobilization from the alteration of interstitial glass. On the whole these experiments indicate these basaltic andesites do not belong to the same genetic suite. They may have been derived from

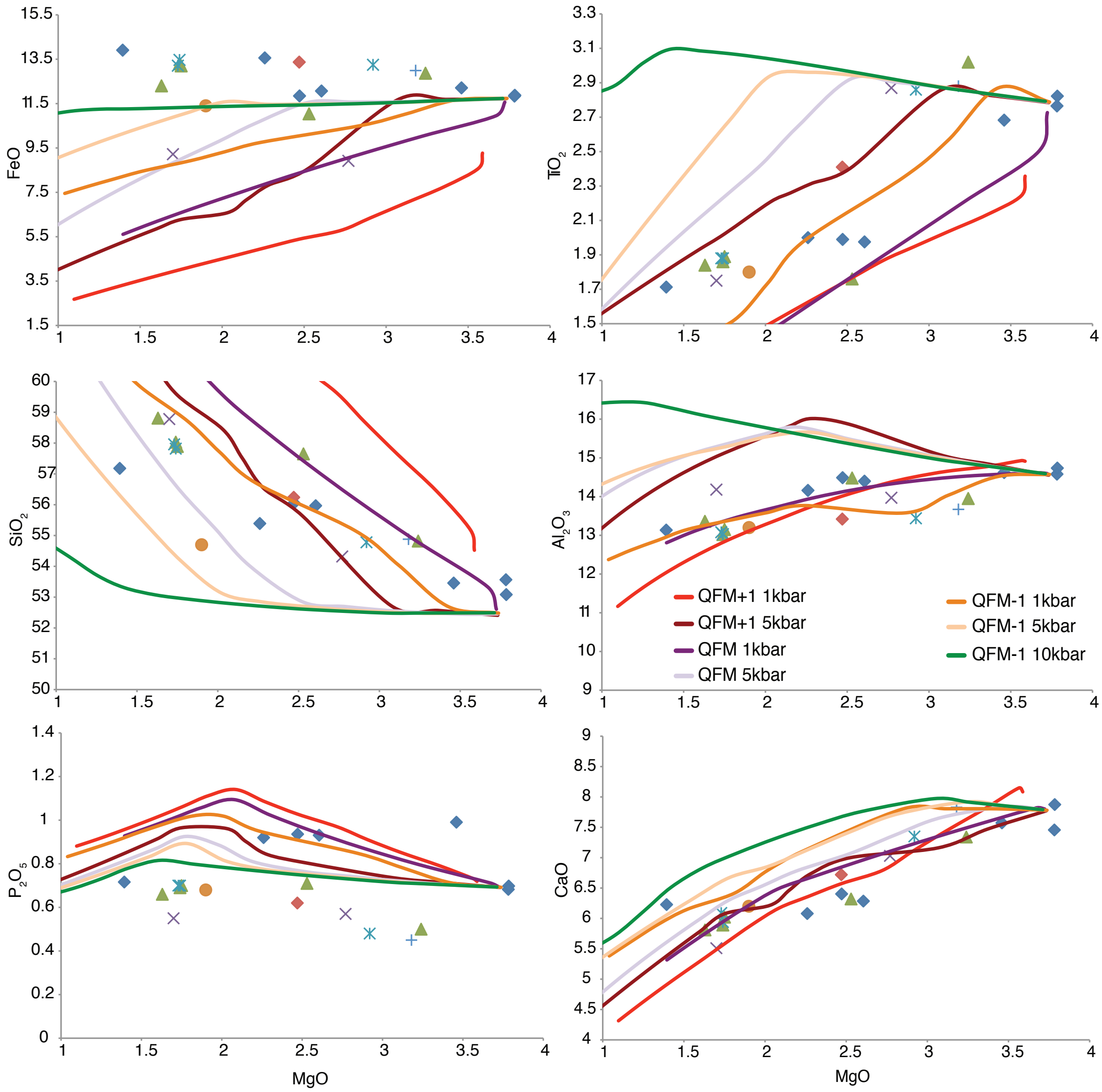

Figure 25. Variation digrams of basaltic andesites. Additional data points taken from the literature (see legend) demonstrate their similarites. Model lines obtained from MELTS experiments are shown for oxygen fugacities of QFM+1, QFM, and QFM-1 at 1 and 5 kbars. One additional line is for a model run at QFM-1 at 10kbar. For the most part the lines substantiate plagioclase, pyroxene and Ti-oxide removal at low pressures. The Fe and P trends require additional processes to explain their trends. The Fe enrichment could be the result of accumulating Fe rich phases, while the variable P contents are likely the result of variable apatite removal, retention or accumulation.

similar parental magmas, but evolved differently due to changes in oxygen fugacity and/or pressure.

Rare earth element (REE) plots (Fig. 26A) indicate relative enrichment in light rare earth elements (LREE), but no strong depletion in heavy rare earth elements (HREE) compared to bulk silicate earth (BSE, McDonough and Sun, 1995). The lack of strong HREE depletion indicates the basaltic andesites were derived from a garnet free mantle source, which suggests sources were either derived from the upper mantle within the spinel zone, or from deeper sources exhausted of garnet due to partial melting that later evolved via fractional crystallization.

The REE patterns all lack negative Eu anomalies. Eu anomalies are a geochemical phenomenon related to the ability of Eu to exist in either a trivalent state (Eu^{3+}) or a divalent state (Eu^{2+}), depending on oxygen fugacity. Under high oxygen fugacities and oxidizing conditions, Eu remains as Eu^{3+} and behaves like the other rare earth elements, but under lower oxygen fugacities and reducing conditions it changes to Eu^{2+}, and substitutes for calcium (Ca^{2+}) in plagioclase. Thus if magma undergoes Rayleigh fractionation of plagioclase under reducing conditions, most of the Eu will be partitioned into this mineral and leave the remaining melt depleted in Eu, therefore causing a negative Eu anomaly. The lack of Eu anomalies suggests the basaltic andesites were derived under high oxygen fugacities. Moreover, the enrichment of Eu versus against SiO_2 (Fig. 26A inset) indicates Eu was not depleted with further differentiation, and suggests it was behaving as an incompatible element during fractional crystallization.

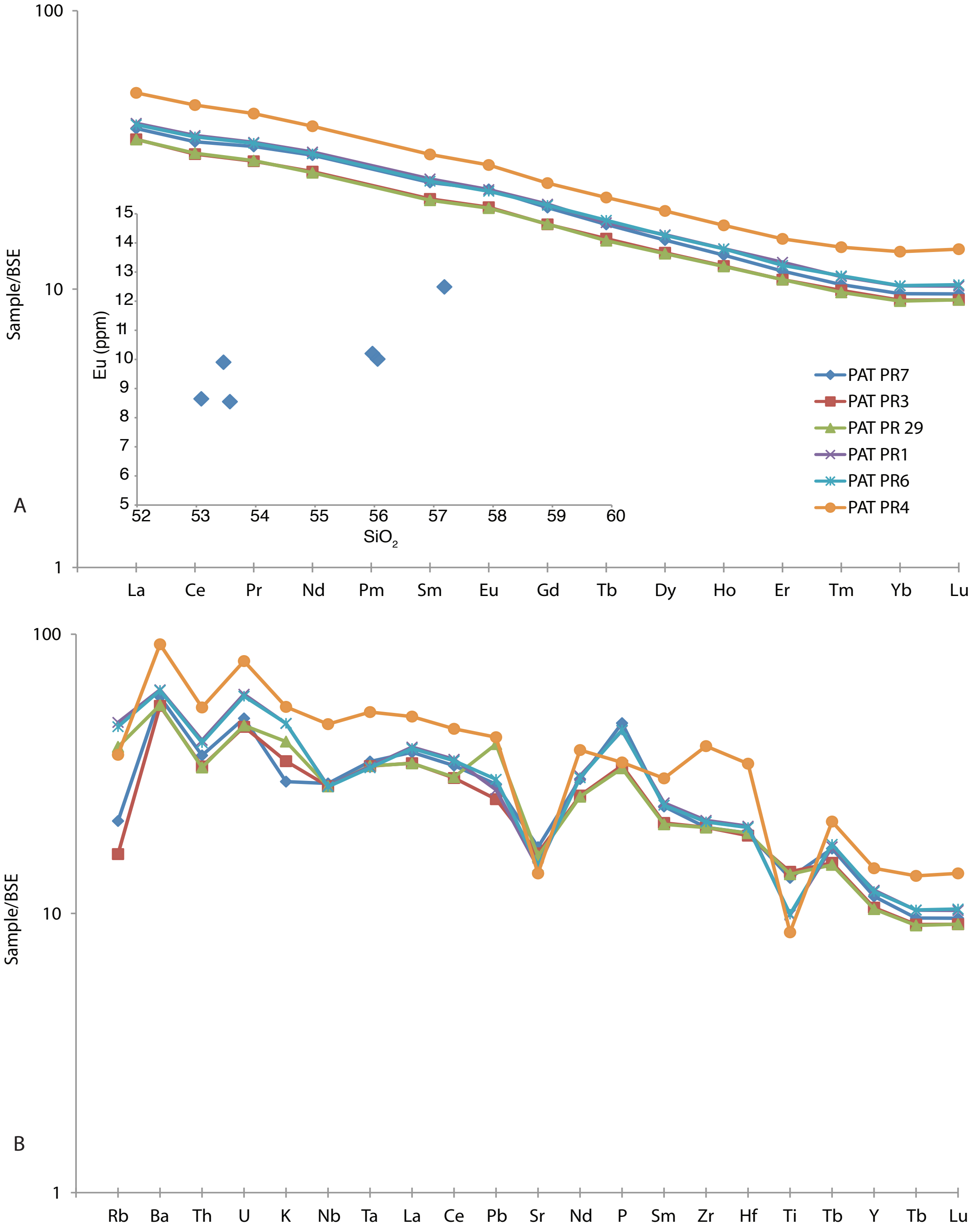

Figure 26. (A) Rare earth element plot of basaltic andesites from Prineville Reservoir normalized to bulk silicate earth (BSE, McDonough and Sun, 1995). Refer to legend for individual samples. (B) Trace element plot indicating Th, Sr and Ti depletion and P enrichment. Note anomalous Zr and Hf enrichment in sample PR4.

Normalized trace element plots (Fig. 26B) indicate relative depletions in Sr, Ti and Th and enrichment in P. Sr depletions are consistent with plagioclase fractionation, but also demonstrate the decoupled behavior of Sr from Eu. Thus, the incompatible behavior of Eu during plagioclase feldspar fractionation supports and confirms the conclusion that these basaltic andesites were probably derived under high oxygen fugacities. Ti depletions are consistent with Fe-Ti oxide fractional crystallization, while Th depletions relative to Ba and U are likely inherited from the source from which these magmas were derived, as Th compatible phases like monazite and allanite are highly soluble in mafic melts. P enrichment is likely controlled by the crystallization and accumulation of apatite. Sample PR4 appears to represent the most fractionated of the basaltic andesites, with the highest SiO_2, and lowest TiO_2 and MgO, and notable enrichments in HFSE, trace elements (Fig. 26B).

Figure 26B reveals weak negative Nb-Ta depletion with respect to La and Th that are suggestive of a non-arc related origin; however, as shown by Leeman and others (1990), many southern Washington Cascade basaltic lavas have atypical Nb-Ta depletions for arc lavas. Nb-Ta depletions of arc lavas have commonly been attributed to the retention of these elements and other HFSE in the subducting slab as a result of their high insolublility in fluids. Thus, these elements are immobile in subducted fluids, while LILE and more mobile elements are transport by these fluids, which leads to their enrichment in the subducting slab (Leeman and others, 1990). Urbanczyk (1994) noted similar muted Na-Ta depletions in the Lower sequence basaltic lavas of the eastern

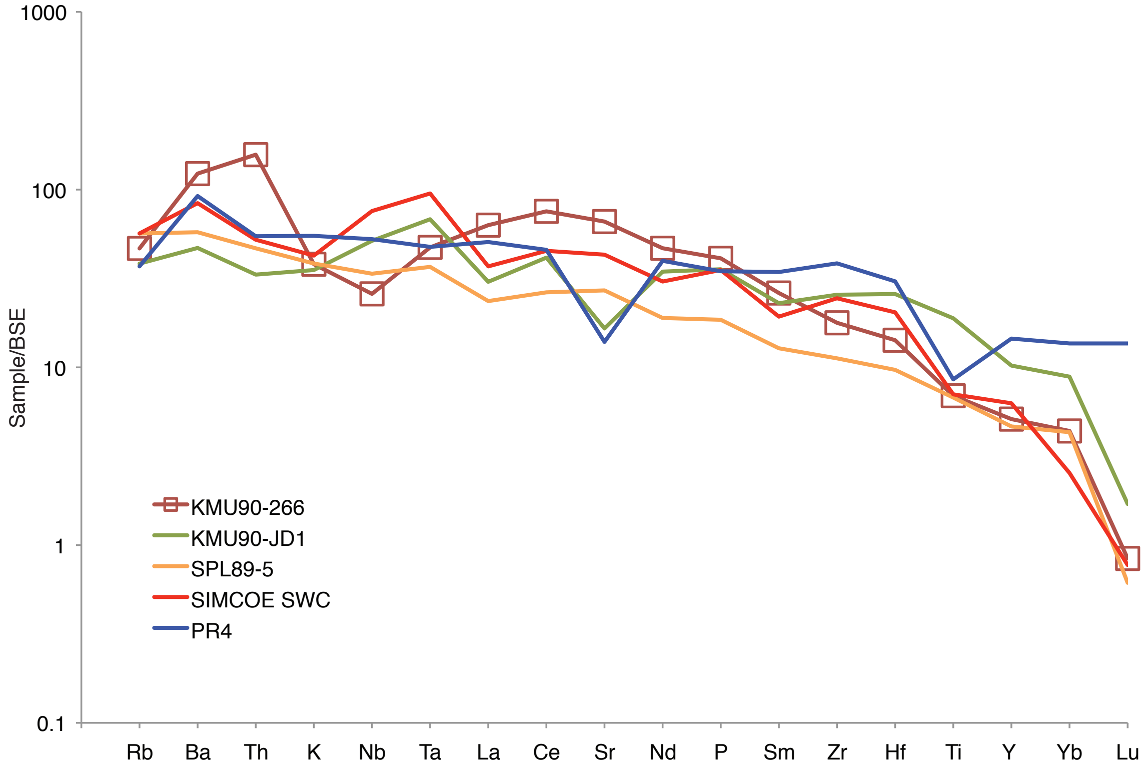

Figure 27. Spider plot including represenative samples of : Prineville basaltic andesite (PAT PR7, this study), Lower and Upper Clarno basalts (SPL89-5 and KMU90-266 respectively; Urbanczyk, 1994), John Day basalts (KMU90-JKD1, Urbanczyk, 1994) and Simcoe basalts from the southern Washington Cascades (SIMCOE SWC, from Leeman and others, 1990). Note prominent negative Nb-Ta anomalies of Upper Clarno basalt, while the John Day basalts and basaltic andesites, Lower Clarno basalts and Simcoe basalts have muted to positive Nb-Ta anomalies. Moreover, the John Day basalts and basatic andesites appear less depleted in heavy rare earth elements.

Clarno Formation and compared them with the Simcoe basalts that Leeman and others (1990) pointed out as having low Ba/Nb (<20) ratios and compositional similarities to ocean island and mid-ocean ridge basalts. The John Day basalts and basaltic andesites (this study) have trace element patterns consistent with the Lower Clarno rocks of Urbanczyk (1994) that show less pronounced Nb and Ta depletions (Figure 27).

Leeman and others (1990) suggested these atypical arc magmas were likely generated from variable melting of mixed sources that were tectonically mixed during the accretion of oceanic and island arc terranes. The fact that central and eastern Oregon are built upon these same types of basement rocks suggests similar processes may have lead to the chemistries observed in these John Day basaltic andesites.

Rhyolites

Rhyolite compositions range from low- to high-silica rhyolite as shown on a total alkali versus silica diagram (Fig. 28). Those that exceed the highest SiO_2-rich position (>77.8 wt% SiO_2) of the granite minimum in the SiO_2 - $NaAlSi_3O_8$ - $KAlSi_3O_8$ ternary system (Tuttle and Bowen, 1958) have been modified by secondary processes. Moreover, if silica has been affect by secondary processes, alkalis have likely been affect as well. Thus, it is necessary to establish a means of evaluating the reliability of the more mobile elements that will be used in evalulating the petrogenesis of these rhyolites. High field strength elements (HFSE) are highly immobile and unaffected by post-eruptive alteration, thus their trends on covariation diagrams reflect petrogenetic processes. Therefore, they serve as good parameters to compare the variation of more mobile elements (Sr, Rb, K_2O and Na_2O). A plot HFSE versus Sr, Rb and K_2O reveals variations that more or less mimic the degree of variation between HFSE and HFSE (Fig.

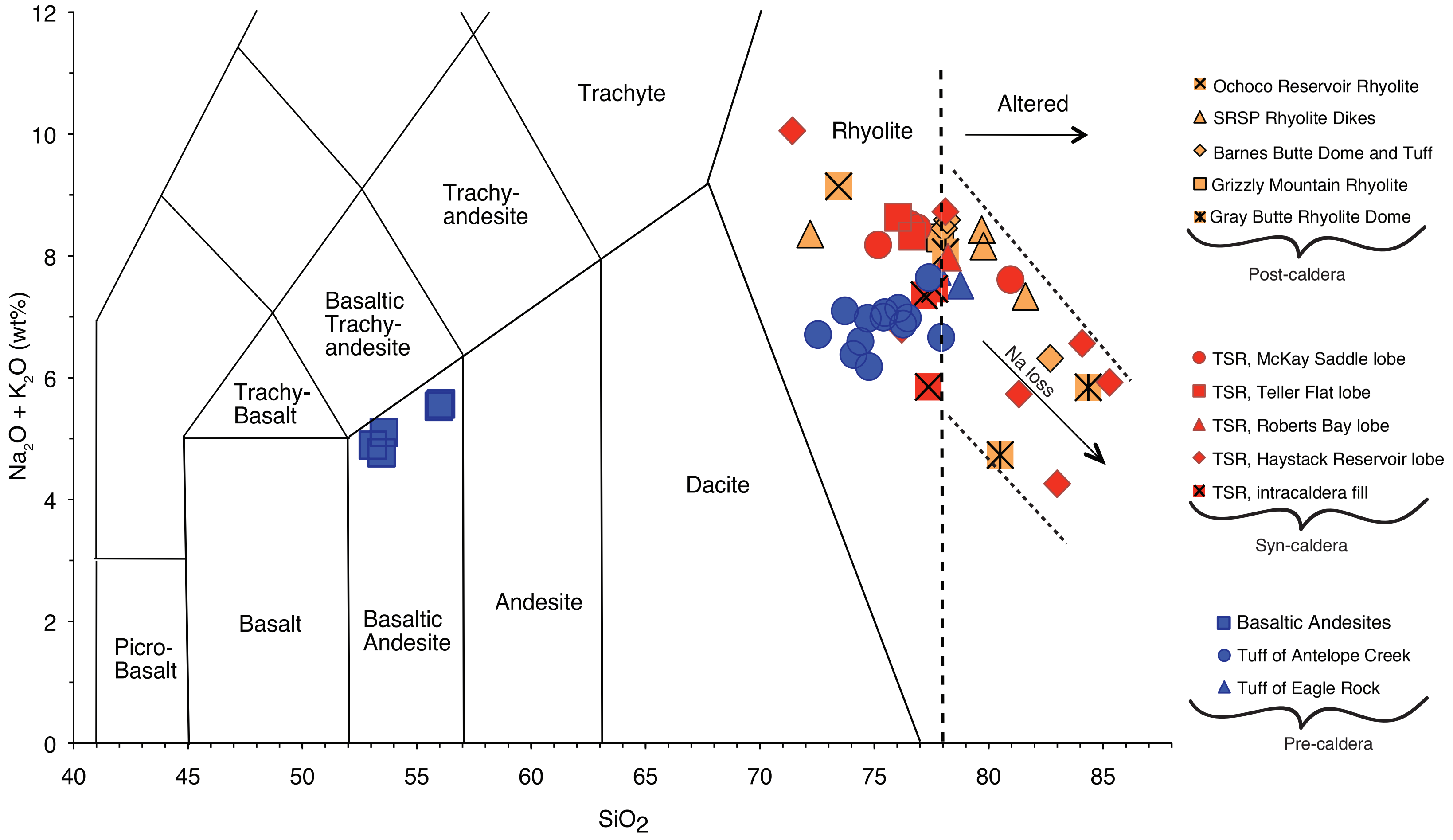

Figure 28. Total alkali versus SiO$_2$ diagram. Rhyolite samples siginificantly depleted in alklalis and exceediing 78% SiO reflect alkali loss and secondary silicification due to post eruptive alteration. Note bomodality of data set. Three different colors denote pre-caldera (blue), syn-caldera (red) and post-caldera (orange) rocks. Refer to legend for individual units. Abbreivations are as follows: TSR = STuff of Smith Rock; SRSP= Smith Rock State Park .

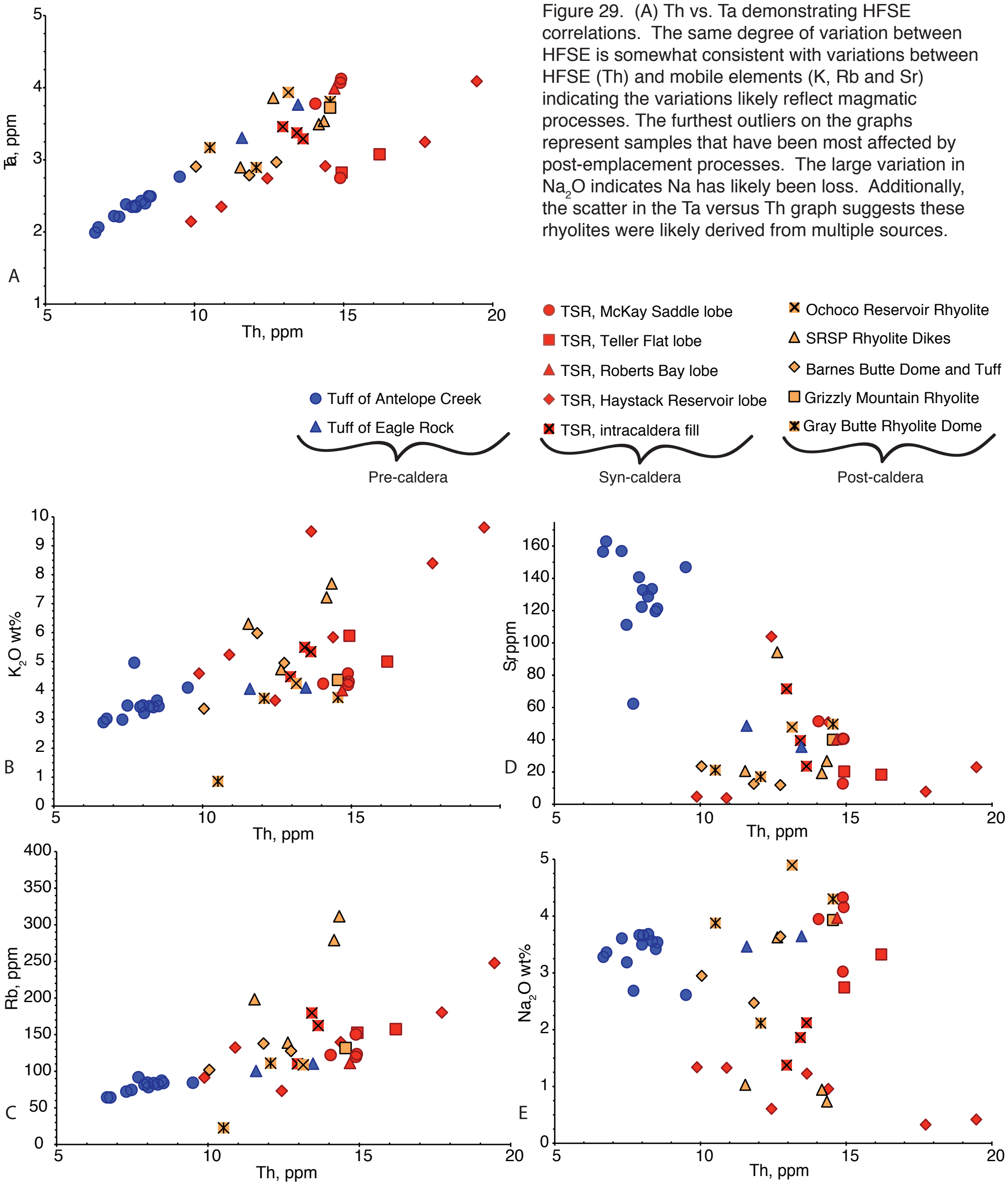

Figure 29. (A) Th vs. Ta demonstrating HFSE correlations. The same degree of variation between HFSE is somewhat consistent with variations between HFSE (Th) and mobile elements (K, Rb and Sr) indicating the variations likely reflect magmatic processes. The furthest outliers on the graphs represent samples that have been most affected by post-emplacement processes. The large variation in Na$_2$O indicates Na has likely been loss. Additionally, the scatter in the Ta versus Th graph suggests these rhyolites were likely derived from multiple sources.

29), indicating the rhyolites have not been severely affected by post-eruptive processes. Only the furthest outliers have likely suffered significant alkali loss. Conversely, the large variations in Na_2O suggest post-eruptive processes have significantly affected Na_2O content. Most of the samples that exceed 77.8 wt% SiO_2 on Figure 28 have notably lower Na_2O, likely as a result of Na_2O loss. Thus, post-eruptive processes have significantly affected Na_2O, but not Sr, Rb, K_2O. Nonetheless, it should be noted that although Sr, Rb and K_2O appear relatively unaffected, devitirification and recrystallization textures suggest they have probably been lowered from original cencentrations on a mole per mole basis.

All but one rhyolite plots within the metaluminous and peraluminous fields on an alumina saturation plot (Fig. 30), and several samples lie on boundaries between the different fields. Thus, clearly defining their compositional affinities with this diagram is difficult when one considers alkalis do not reflect original concentrations. Therefore an alternate method is needed to illustrate the compositional affinities of these rhyolites.

As previously discussed, HFSE are useful indicators in altered rocks, as they are unaffected by post-eruptive processes, but Zr and Hf are particularly useful as they monitor zircon fractionation, which in turn can be indicative of peralkaline compositions. Watson (1979) demonstrated the relationship between zircon solubility and alkali content, and found that zircon solubility is highly sensitive to the molar proportions of $(Na_2O+K_2O)/Al_2O_3$. Thus, the high alkali contents of peralkaline melts greatly increases the concentration of soluble zirconium. This explains why peralkaline melts rarely become saturated with respect to zircon, compared to metaluminous and peraluminous melts ($Al_2O_3 > (Na_2O+K_2O)$) that become saturated with just a few 100 ppm Zr (Watson

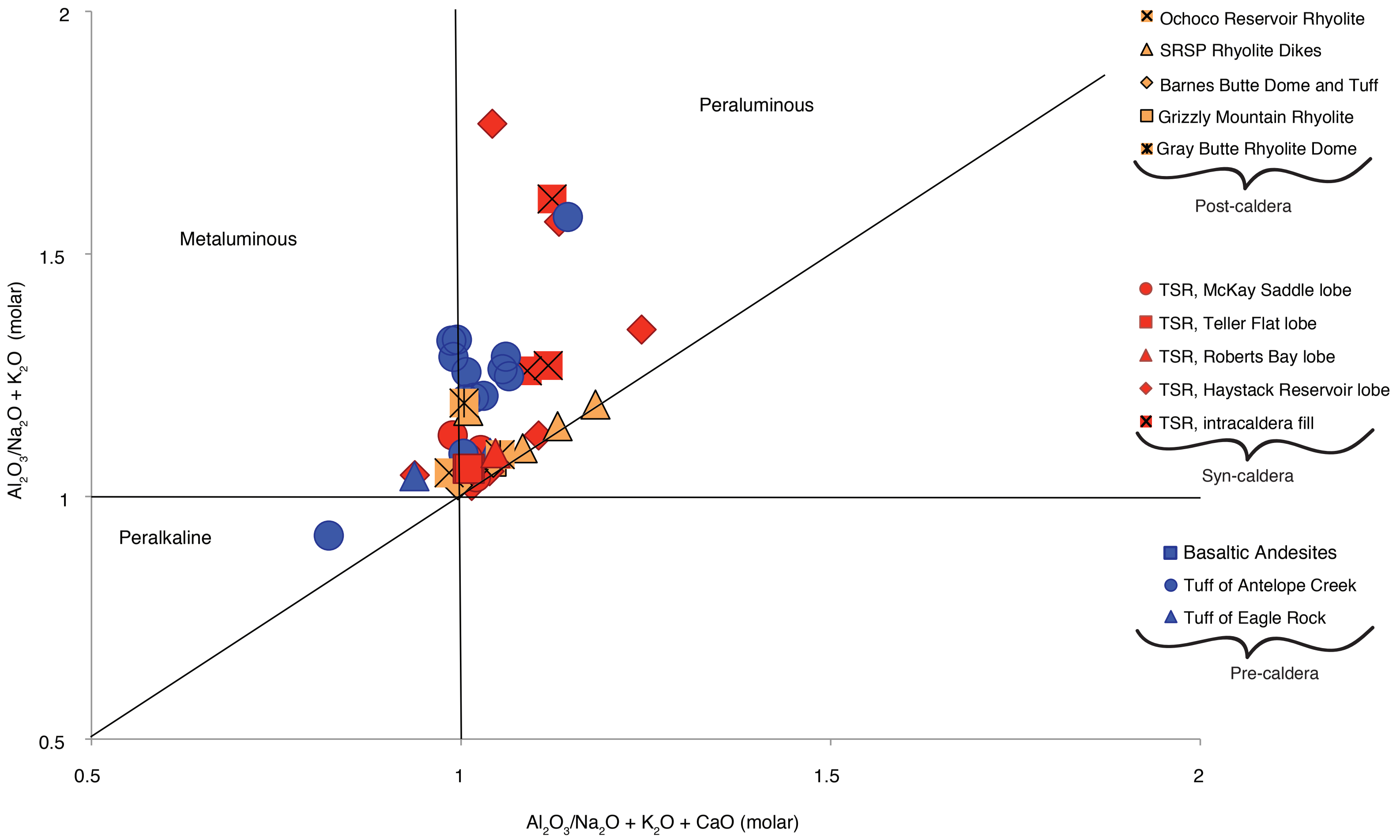

Figure 30. Alumina saturation plot showing the apparent majority metaluminous to peraluminous chemical compositions.

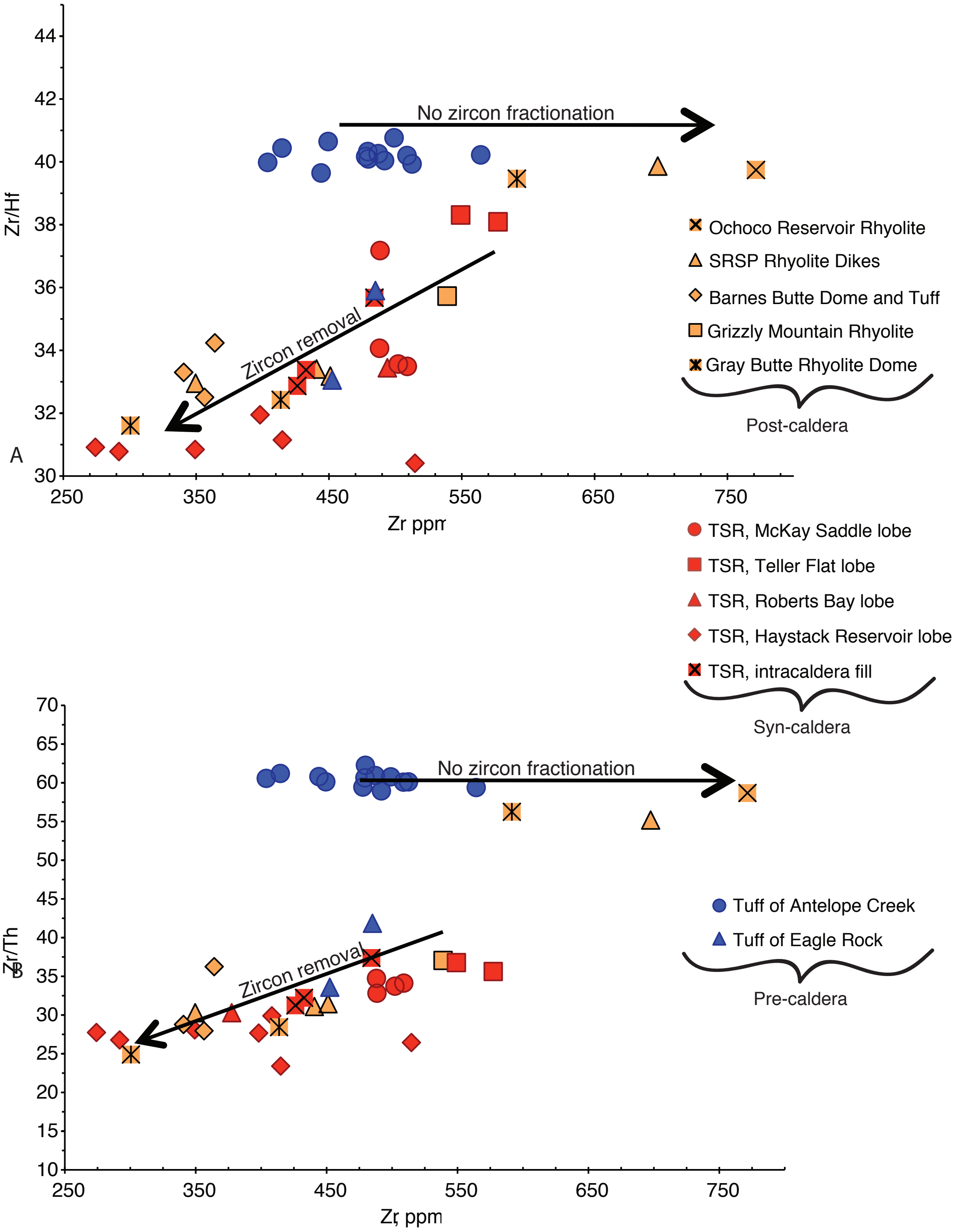

Figure 31. (A) Zr/Hf ratios versus Zr indicating variable zircon fractionation. (B) Zr/Th versus Zr ppm, showing decreasing Zr/Th ratios and Zr abundances as a result of zircon fractionation and higher constant Zr/Th for samples that did not fractionate zircon.

and Harrison, 1983). The increased solubility suppresses zircon crystallization in perakaline melts, which in turn results in constant Zr/Hf ratios and no decoupling of Zr from Hf. Thus, it is reasonable to infer that if rhyolitic magmas have constant Zr/Hf ratios indicating no zircon fractionation they are likely peralkaline.

Plots of Zr/Hf and Zr/Th versus Zr (Fig. 31) reveal the older pre-caldera Tuff of Antelope Creek has constant Zr/Hf and Zr/Th ratios consistent with no zircon fractionation, which indicates they are peralkaline. Additionally, a few post-caldera units consistent with the trend of the Tuff of Antelope Creek indicate they too are peralkaline and their high Zr concentrations further substantiate this conclusion. The rest of the syn- and post-caldera rhyolites show variable Zr/Hf and lie along a trend of decreasing Zr/Th ratios (Fig. 31) indicating of zircon fractionation. However, several samples overlap with the Zr concentrations of the Tuff of Antelope Creek and are consistent with peralkalinity. Thus, there is an inconsistency between Zr concentration and zircon fractionation, which obscures the classification of these particular samples.

The zircon solubility equation of Watson and Harrison (1983; rearranged by Miller and others, 2003):

$$T_{zr} = 12900/[2.95 + 0.85M + \ln(496000/Zr_{melt})]$$, where

T_{Zr} = temperature of melt (in Kelvin)

M = (K + Na + 2Ca)/(Al*Si) in molar proportions

Zr_{melt} = Zr concentration in saturated melt provides a means of determining a hyporthetical Zr_{melt} content needed for the melt to be saturated in zircon, at a given temperature and M value. Thus, variable amounts of Na_2O wt% were added to recalculate M at different temperatures to calculate a hypothetical Zr_{melt} that could be compared the whole rock Zr values. Temperatures were assumed to range from 800-850°C based on (1) the lack of high temperature rheomorphic textures comparable to the Snake River Plain (SRP) rhyolites, which have temperatures upwards of 950-1000°C (Honjo and others, 1992) and (2) temperature estimates for comendite ash flow tuffs of the McDermitt caldera by Conrad (1984). Calculations reveal that at temperatures of 850°C with 3.0 wt% Na_2O added to correct for alkali loss, calculated Zr_{melt} concentrations reach the actual whole rock zircon concentrations (Fig. 32). This strongly suggests these rhyolites were originally peralkaline, but fractionated zircon likely as a result of (1) being less peralkaline than the group that did not fractionate zircon and/or (2) falling temperatures that drove the melt towards conditions in which zircon was stable.

On the peralkaline discrimination diagram of Macdonald (1974) the rhyolites all appear to be comendites that range from high FeO (~4.0 ± 1.0 wt %) wt% to low FeO (~2.0 ± 1.0 wt %; Fig. 33). Thus, the rhyolites can be divided into high-Fe comendites with constant Zr/Th ratios and the low-Fe comendites with decreasing Zr/Th ratios. Discussion of other major, minor and trace element variations between each group will be discussed in the following pages, but it is important to point out the geochemical similarites between the rhyolites.

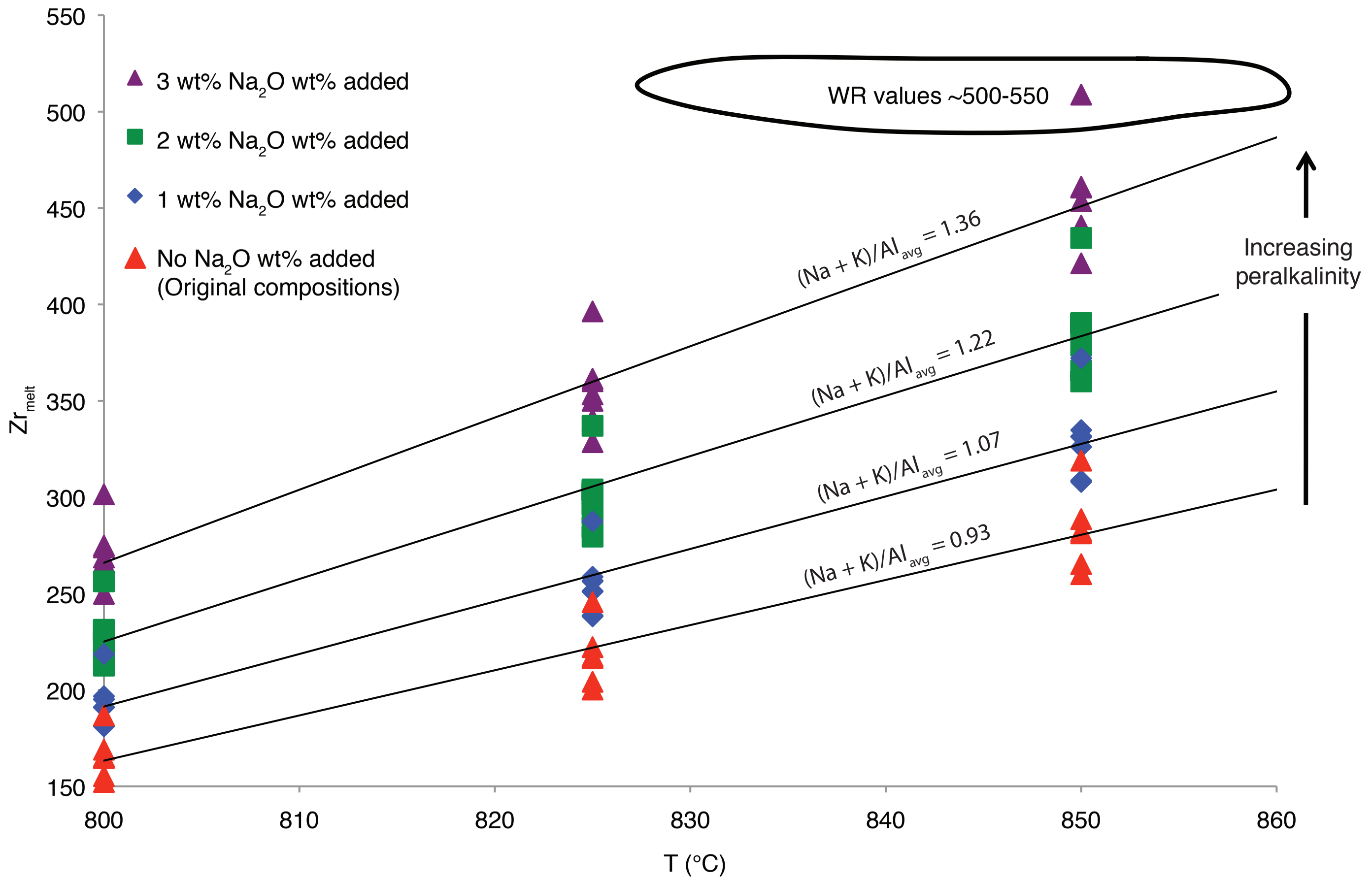

Figure 32. Plot of calculated Zr_{melt} concentrations versus temperatures at 800, 825 and 850 °C. Different symbols represent changing Zr_{melt} concentrations with the addition of Na_2O wt% at assumed temperatures. As indicated, original (Na+K)/Al ratios are not indicative of peralkaline compositions. However, the addition of 1 wt% Na_2O to the rhyolites makes them peralkaline [(Na+K/Al)] >1, which in turn causes Zr_{melt} to increase and trend towards higher and higher values. Thus, the fact that calculated Zr_{mel}t reach whole rock values at reasonable temperatures and Na_2O wt% addition strongly suggests these rhyolites were originally peralkaline.

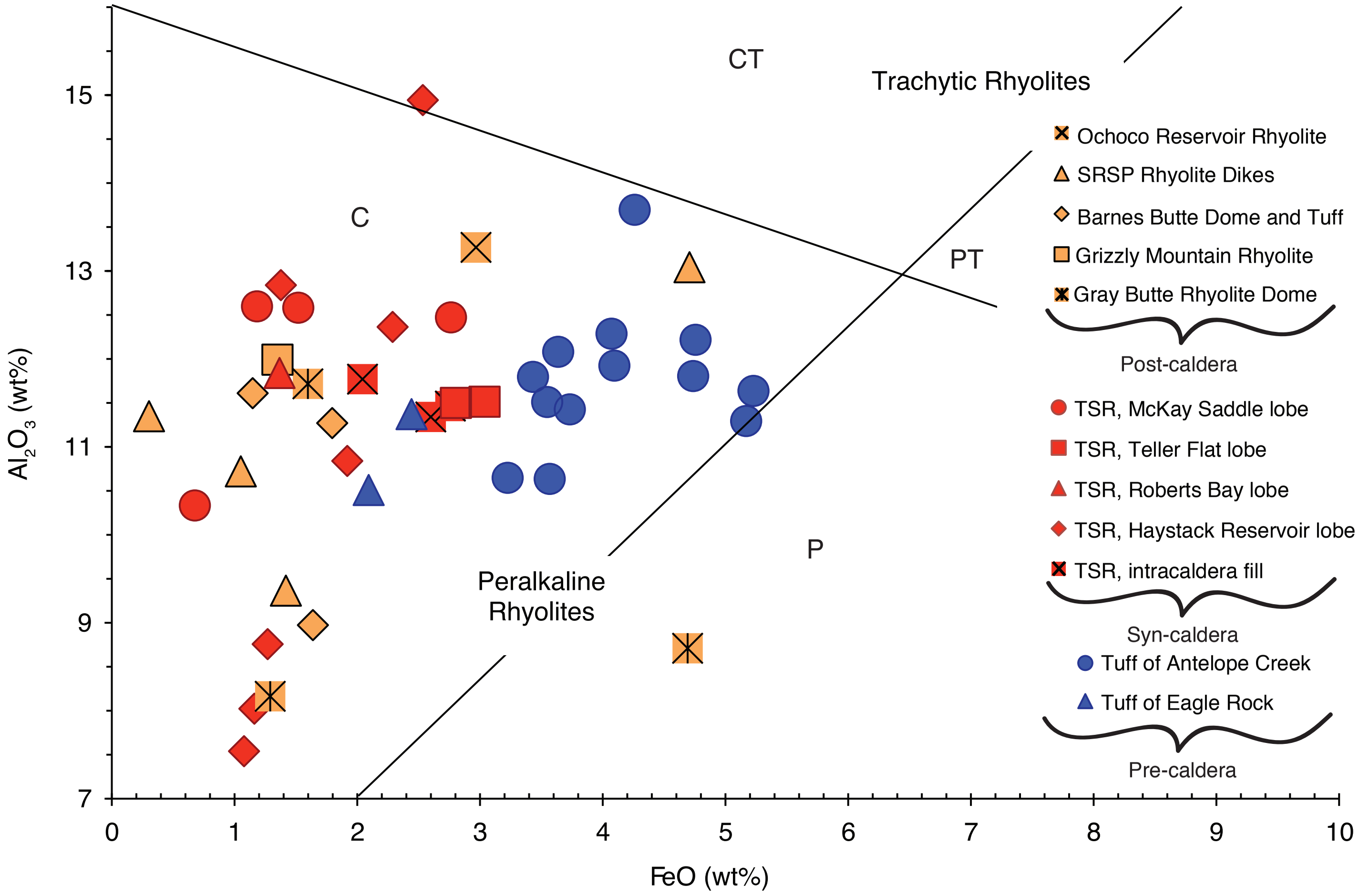

Figure 33. (A) Peralkaline discrimination diagram of Macdonald (1979) showing that most rocks are comendites. Abbeviations as follows: C = Comendite; CT = Comenditic trachyte; PT = Panterlleritic trachyte; P = Pantellerite. .

All the rhyolites share A-type and within-plate granitoid geochemical affinities based on the granitoid discrimination diagrams (Fig. 34A&B) of Whalen and others (1987) and Pearce (1984), which prior to this study A-type granitoid affinities have not been recognized in the JDF. This recognition of A-type affinities opposes the long-held view that John Day volcanism was directly subduction related (Robinson, 1975; Robinson and Brem, 1981; Robinson and others, 1984; Bestland and others, 1999) and raises important questions about John Day volcanism and petrogenesis.

Eby (1990) suggested a two-fold subdivision of A-type granites based on differing Y/Nb ratios (Eby, 1992). He found that A-type granites with low Y/Nb ratios <1.2 (A_1 sub-type) plotted within or fell along fractionation trends emanating from average ocean island basalt (OIB), and suggested these granites represent mantle differentiates derived from OIB sources that were emplaced in continental rifting for intraplate magmatism. Conversely, A-type granites with higher Y/Nb ratios (>1.2) plotted with ratios more consistent with island arc basalts or continental crust. He suggested these magmas were derived from continental crust or underplated crust that has been though a cycle of continent-continent collision or island arc magmatism. The majority of the rhyolites from this study plot in the A_2 field (Fig. 34C) and have Y/Nb ratios >1.2, which suggest they were derived from a source chemically similar to island arc basalts and/or continental crust.

Thus, based on the less Nb-Ta depletions observed in the basaltic andesites and the A_2 characterisitcs, these John Day rhyolites are likely not strictly subduction-related volcanics, but may have relict features of these type of sources in their chemical signature as a result of accreted arc and ocean island terranes being involved in their petrogenesis.

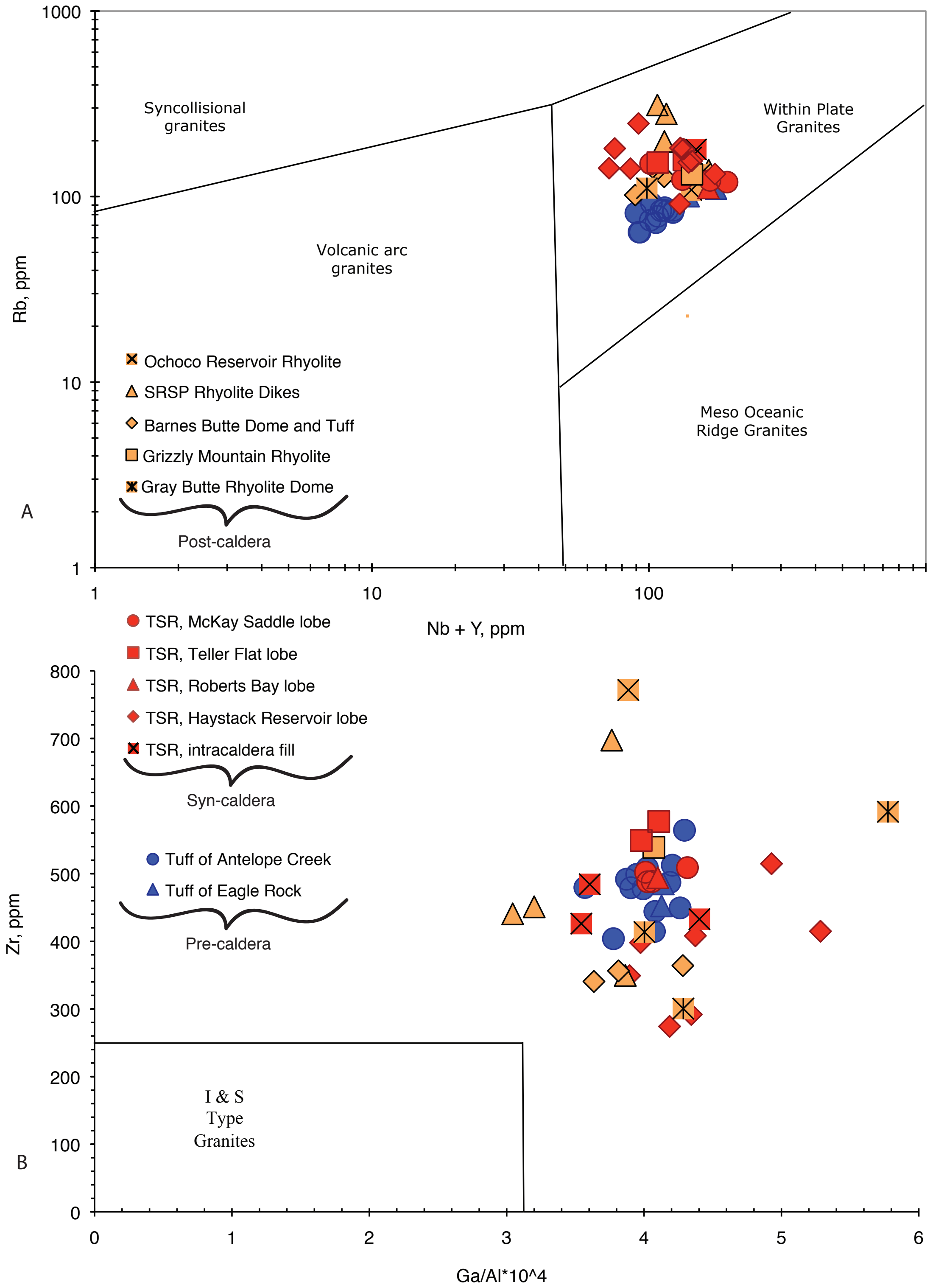

Figure 34. Rhyolite ash flows, dome and flows plotted on A-type discrimination diagrams of (A) Whalen et al., 1987 and (B) Pearce et al., 1984. Some of the scatter in Rb content is probably due to secondary effects, but all samples plot in the within plate granite field nonetheless.

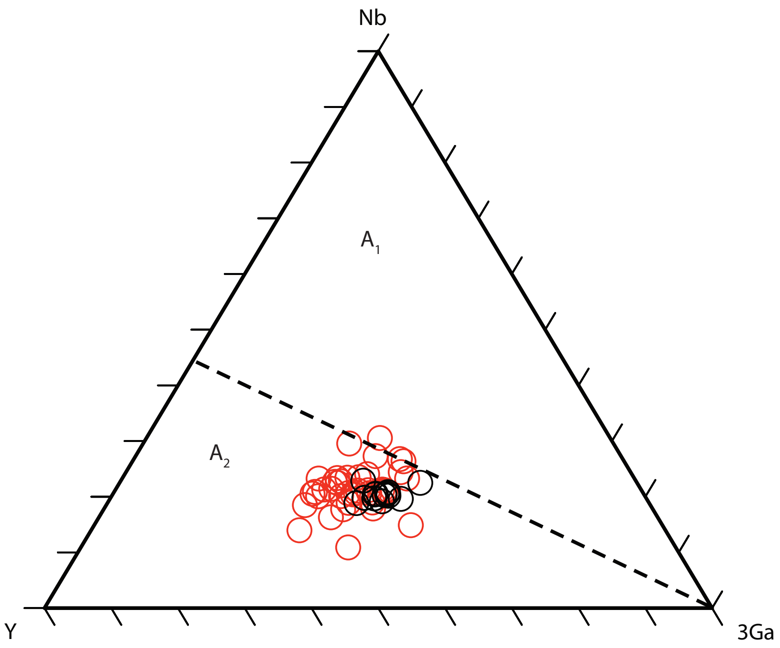

Figure 34C. Ternary diagram (from Eby, 1992) indicating an overall A$_2$ subtype affinity. Dashed line corresponds to Y/Nb ratio of approximately 1.2. Black and red circles correspond to high- and low- Fe groups respectively (described in following pages).

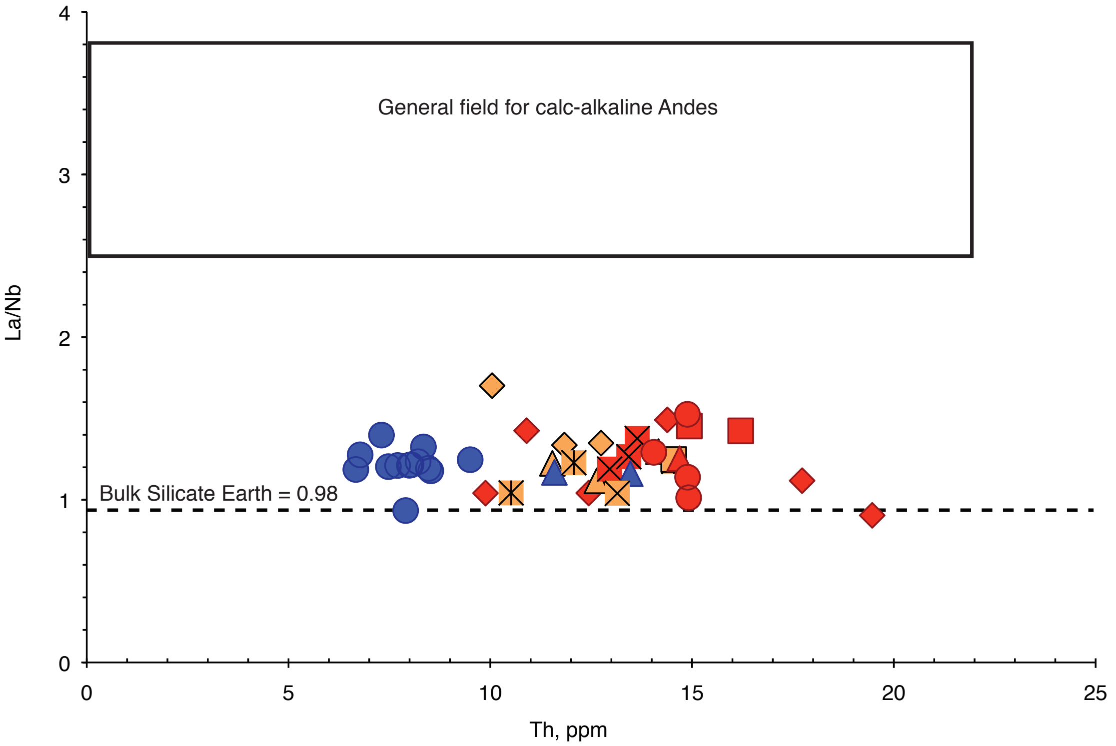

Figure 35. La/Nb ratios versus Th, demonstrates low LILE/HFSE ratios that are typically higher in arc magmas fom melting of sub arc mantle, which is enriched in LILE as a result of metasomatism . This is further evidence that the John Day rocks are not strictly subduction related. Bulk Silicate Earth La/Nb ratio calculated from MDonough and Sun (1995).

Further evidence against a strictly subduction related origin are in the low La/Nb ratios (Fig. 35) of all the samples, which are more consistent with melts generated in an extensional, rather than a compressive subduction setting.

Geochmical differences between Rhyolite groups

As shown, the rhyolites can be divided into high- and low-Fe comenditic groups. The high-Fe group mostly consists of sample from the older Tuff of Antelope Creek, while the low-Fe group includes the younger syn- and post-caldera rhyolites associated with the formation of the Crooker River caldera. However, some overlap does occur, as samples from a few units plot in both groups, and the low-Fe group is chemically diverse.

Major element variations indicate the high-FeO group shares similar Al_2O_3 contents with the low-Fe group, but are generally enriched in CaO and TiO_s at lower SiO_2 (Fig. 36A, B, C and D). Other major element oxides K_2O, and Na_2O are not plotted as they have been affected by post-eruptive alteration, and therefore do no reflect original magmatic values. Pyoxene compositions in the high-Fe group range from ferrohedenbergites (Wo_{44} En_2 Fs_{54}) to ferroaugites (Wo_{42} En_{22} Fs_{36}; Fig. 37A). However, these compostions only represent compositions obtained from two samples, thus may not accurately represent the full compositional range of the high-Fe group. Due to the high degree of alteration, no fresh pyroxenes were found in the low-Fe group. Two feldspar compositions were found in each group and include andesine (An_{30-50}) and sanidine (Or_{35-50}: Figure 37B). However, it should be noted that andesine appears to be more abundant in the high-Fe group, while sanidine appears more abundant in the low-Fe group. Accepted mineral compositions are listed in Table 1.

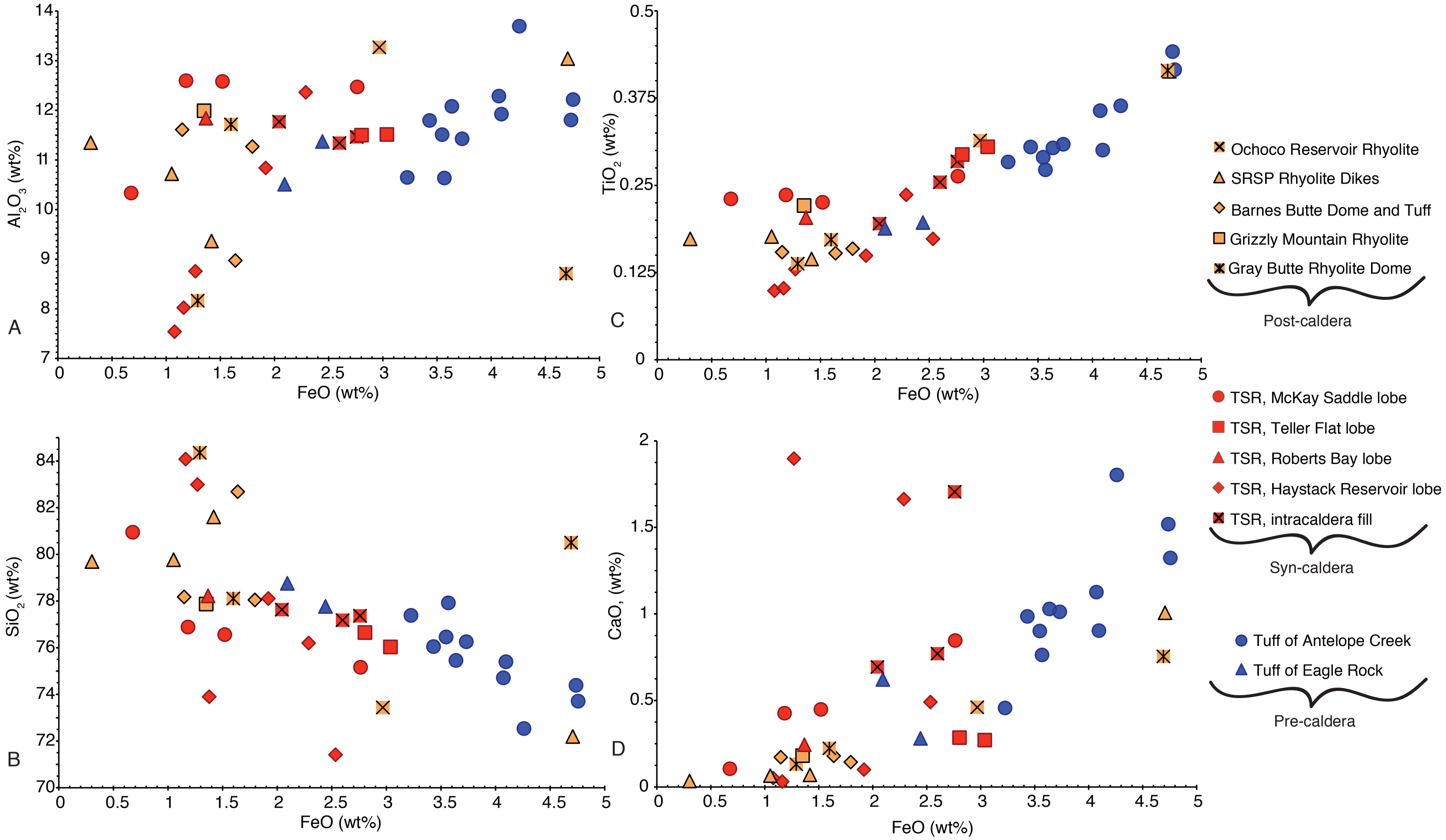

FIgure 36. Major element variation diagrams showing (A) similar Al$_2$O$_3$ contents between the groups, but higher TiO$_2$ (C) and CaO wt% (D) contents of the high-Fe group at generally lower SiO$_2$ contents (B).

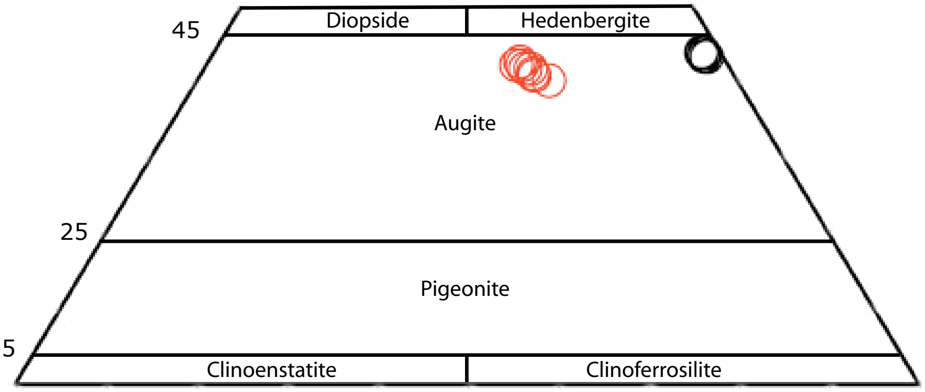

Figure 37a. Pyroxene microprobe data showing high Fe group compositions. Black circles indicate high Fe group and red circles indicate low-Fe group.

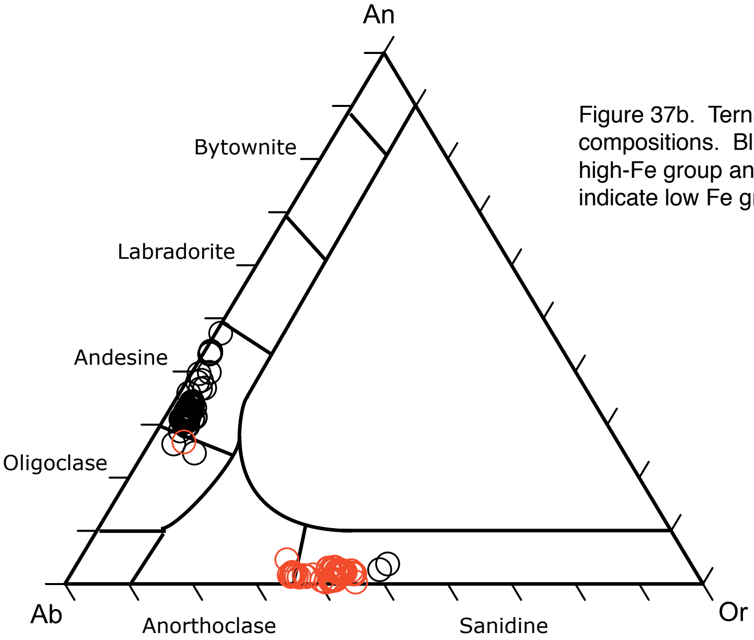

Figure 37b. Ternary plot of feldspar compositions. Black cirlces indicate high-Fe group and red circles indicate low Fe group.

Table 1. Pyroxene and Feldspar end member compositions.

Mineral	Sample ID	Unit	Ca	Na	Mg	K	Fe
Pyx	PH1G	high-Fe group	43.75		1.98		54.26
	OR1		41.69		22.32		35.98
Fs	PP	Intra caldera fill	26.81	68.43		4.76	
	HS2	Out flow at Haystack Reservoir	0.75	59.85		39.40	
	TF2	Outflow at Teller Flat	2.55	55.67		41.77	
	GR1	Grizzly Mt Rhyolite dome	0.42	54.71		44.87	
	PR10	Prineville Reservoir high-Fe Grp	32.59	64.23		3.18	
	PR12	Prineville Reservoir high-Fe Grp	3.76	47.54		48.70	

*McKay Saddle feldspars were albitized

Overall the high-Fe group tends to be less depleted in Sr and Eu and less enriched in Th, Rb and Nb relative to the low-Fe group (Fig. 38A, B, C, D and E). Both groups share similar Zr concentrations (Fig. 38G&H), but the high-Fe group has slightly lower Hf concentrations (Fig. 38G) that generally separate the units into the two groups previously defined by their degree peralkalinity and FeO content. However, because zircon did not fractionation in the high-Fe group (Fig. 38G) as evidences by constant Zr/Th (Fig. 31B) and Zr/Hf (Fig. 38G) ratios, the lower Hg concentrations in the high-Fe group must be a source effect, as only zircon would lower Hf values.

Rare earth element (REE) plots (Fig. 39A&B) indicate slight enrichment in LREE and negative Eu anomalies in both groups, though there are subtle differences between them. The high-Fe group is slightly less enriched in LREE, and has modest Eu anomalies compared to the low-Fe group, which may indicate higher oxygen fugacities, though higher oxygen fugacities are inconsistent with FeO enrichment (Christiansen and McCurry, 2008). Both groups have relatively flat heavy rare earth element patterns (HREE), though the HREE are more variable in the low-Fe group.

Normalized trace element diagrams of both groups (Fig. 40A&B) show Sr, P, Ti depletions, qualitatively consistent with plagioclase, apatite and Fe-Ti oxide fractionation. However, the high-Fe group has less negative Sr depletions consistent with its modest negative Eu anomalies and supports a modest role of plagioclase fractionation or less residual plagioclase in the source. Moreover, the lack of significant fractionation of Eu from Sr (Fig. 41B) substantiates the limited role of plagioclase fractionation during petrogenesis of the high-Fe group. The higher Sr/Eu ratios of the

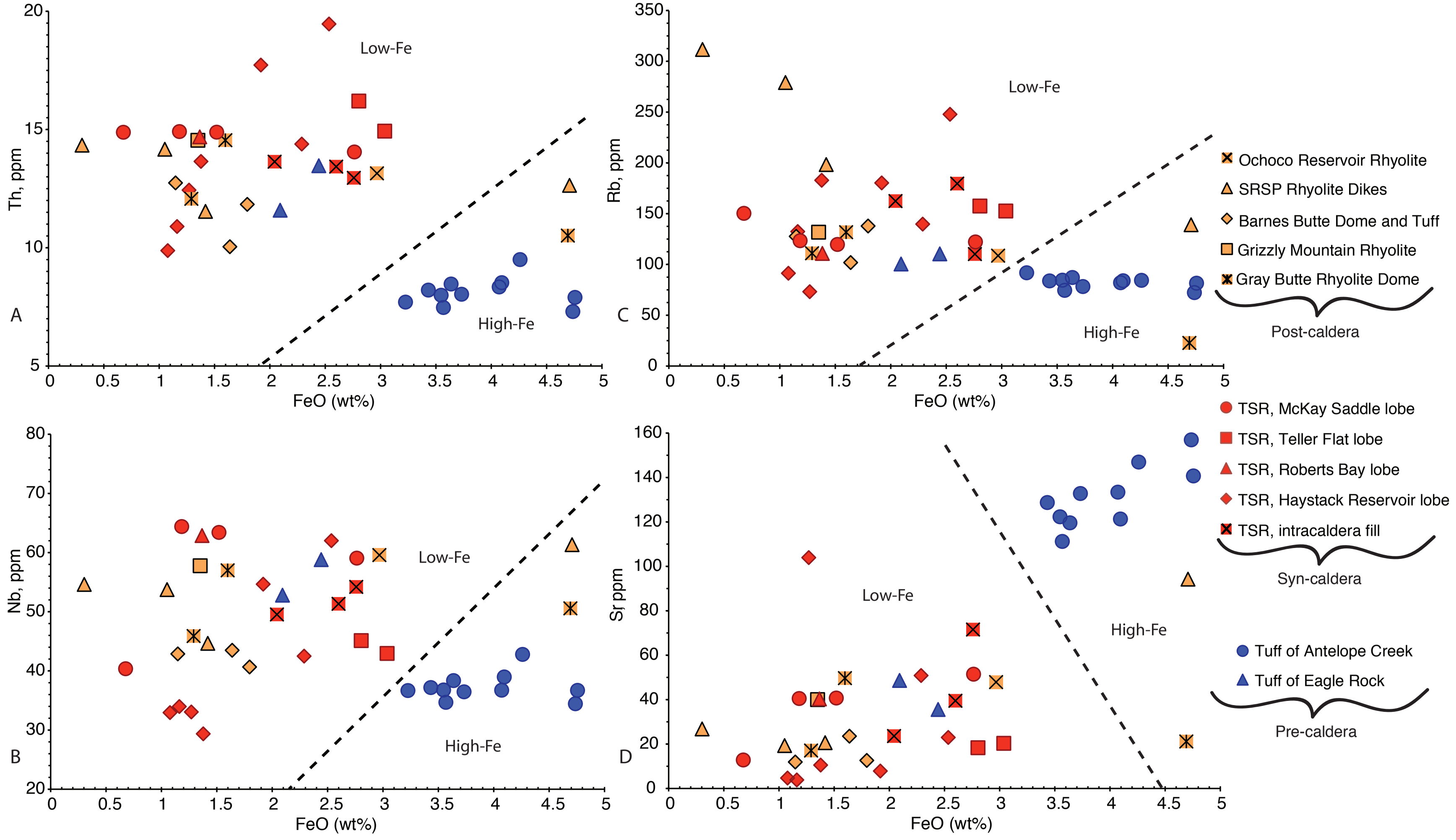

Figure 38. Major and minor trace element abundances showing the compositional differences between the high and low Fe groups. (A) Note higher FeO wt. % correspond to lower Th concentrations, a characteristic of the high Fe group. (B) High Fe group also has (C) lower Rb and (D) Nb, but (B) higher Sr abundances.

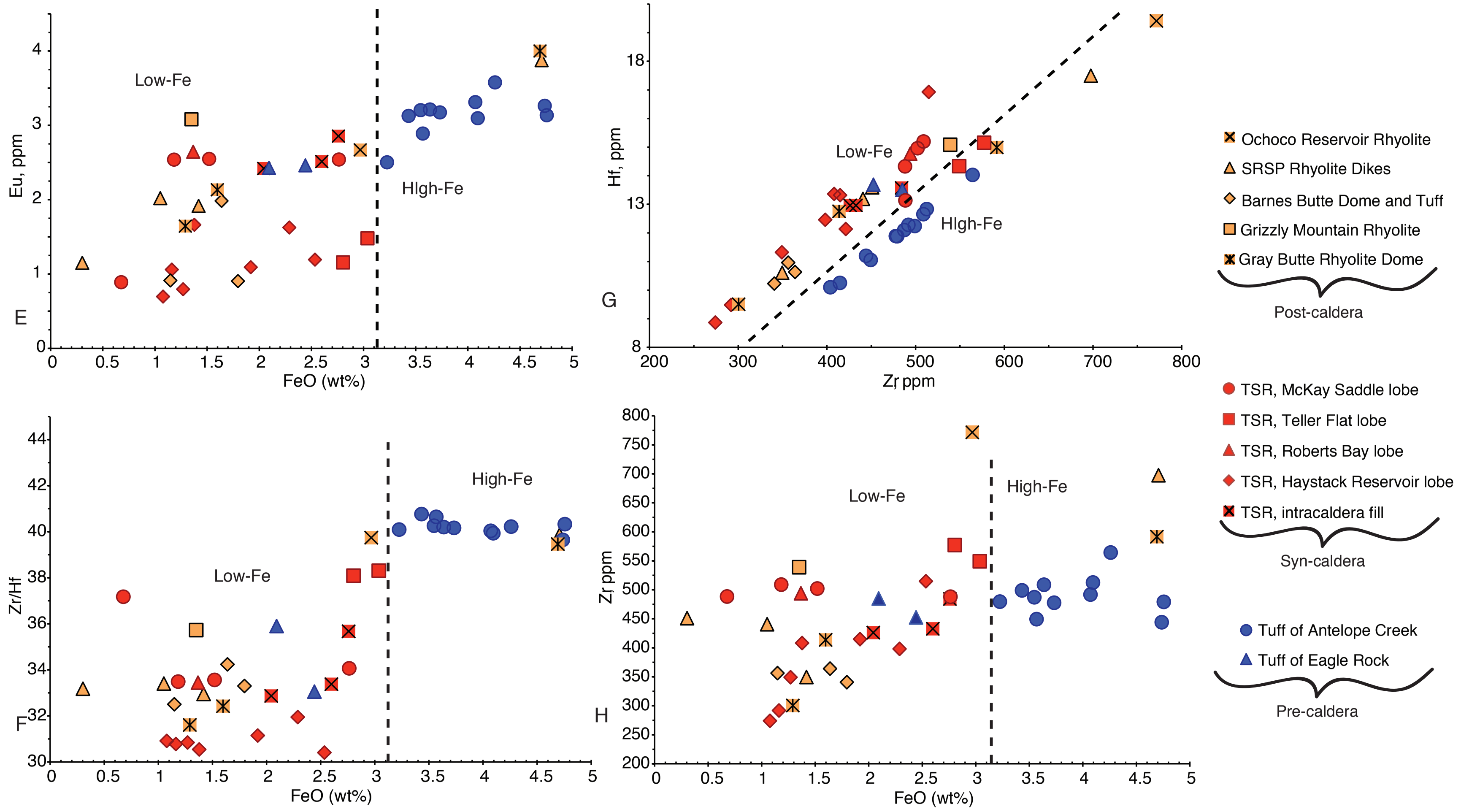

Figure 38 continued.

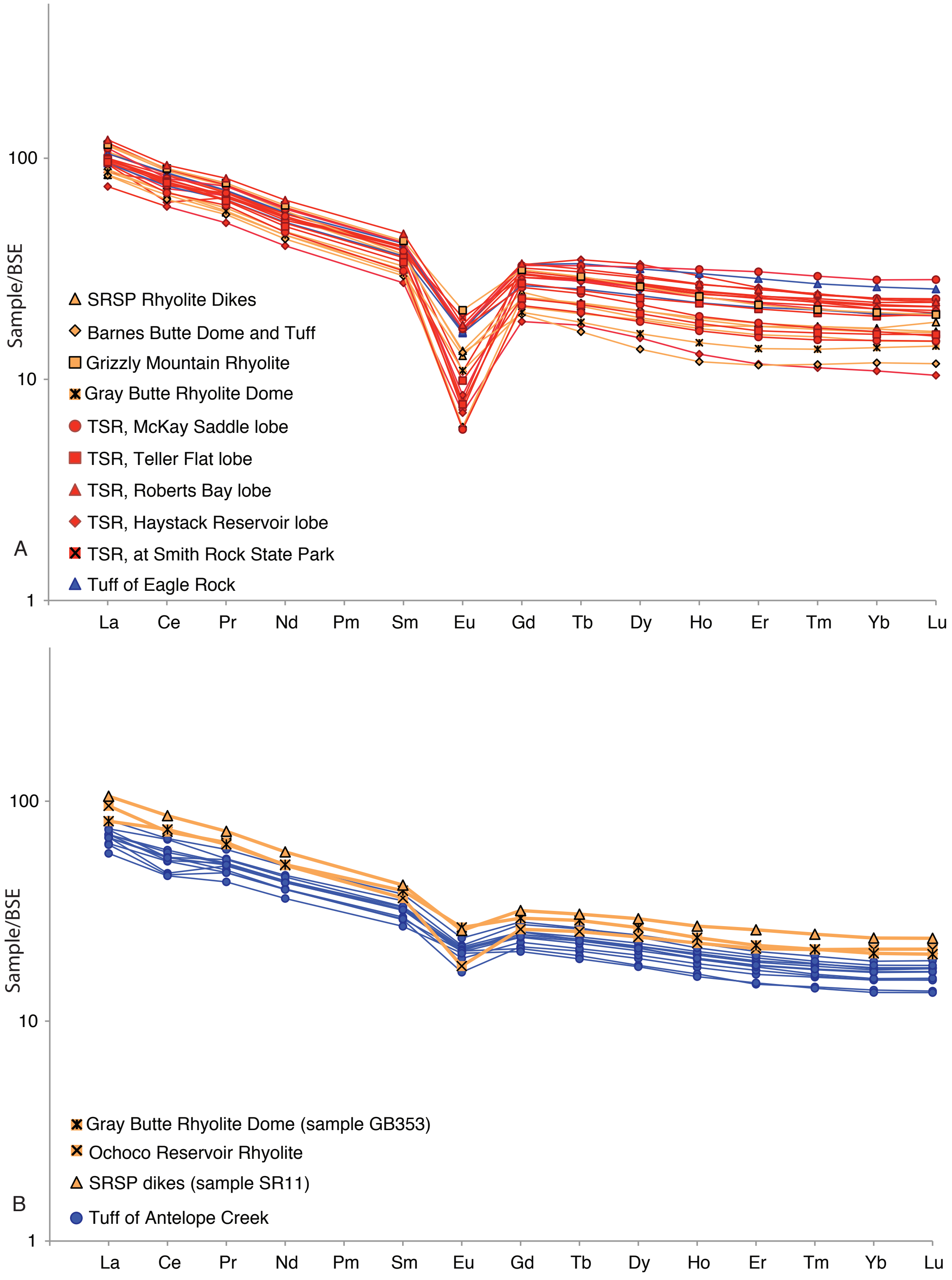

Figure 39 . Rare earth elements of (A) low-Fe and (B) high-Fe groups. Note modest Eu anomaly of the high-Fe group to the low-Fe group indicating more plagioclase fractionation during the petrogenesis of the low-Fe group. SRSP = Smith Rock State Park. The few samples from the low that lie along the higher Zr/Hf trend have been plotted with the more peralkaline Tuff of Antelope Creek.

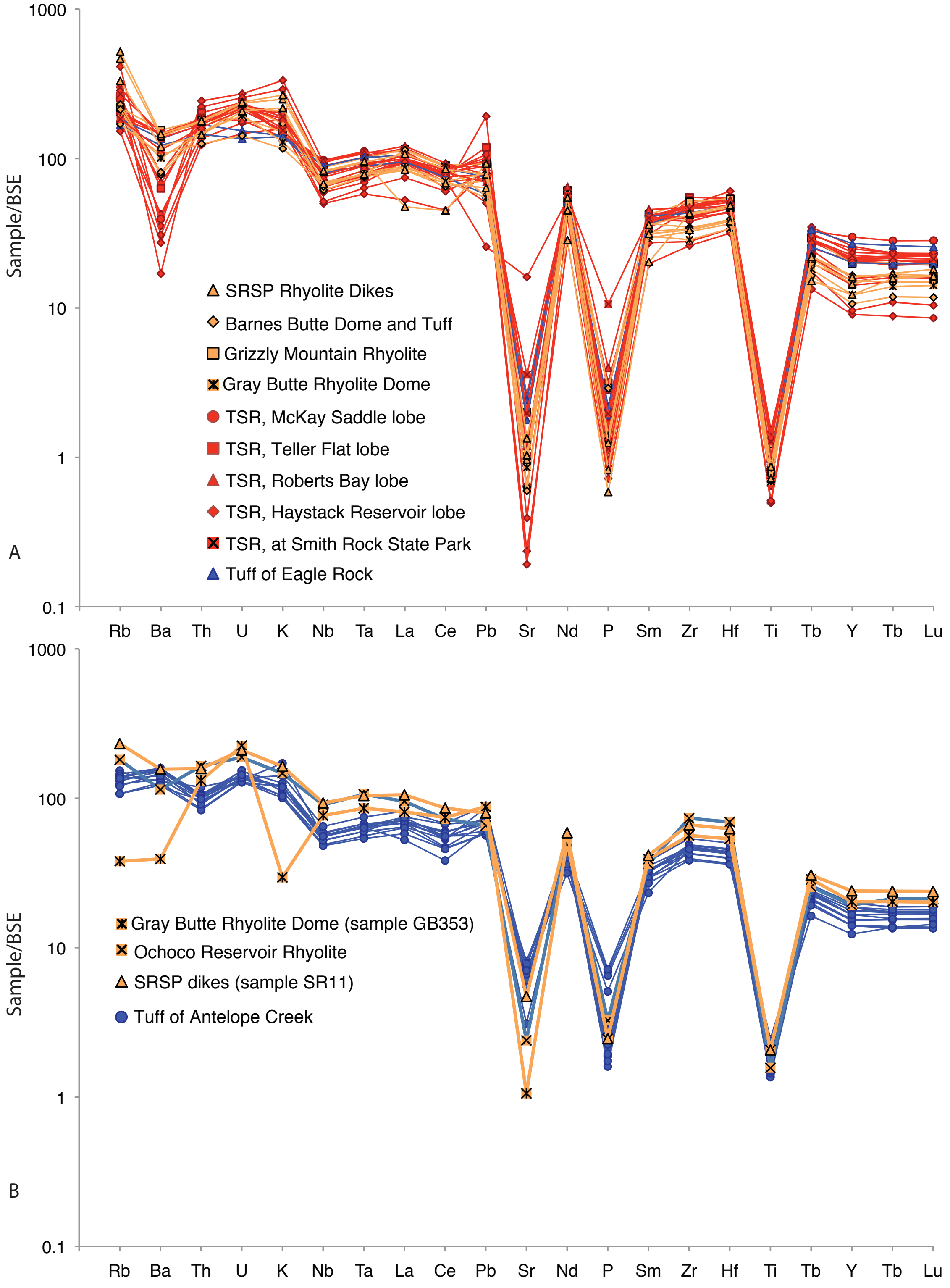

Figure 40. Trace element plots of (A) low- Fe and (B) high- Fe groups. Sr, P and Ti depletion in both groups is consistent with plagioclase, apatite and Fe-Ti oxide fractionation. Note Th depletion and bimodal P in high-Fe group and Ba depletion in low-Fe group. The few samples from the low that lie along the higher Zr/Hf trend have been plotted with the more peralkaline Tuff of Antelope Creek.

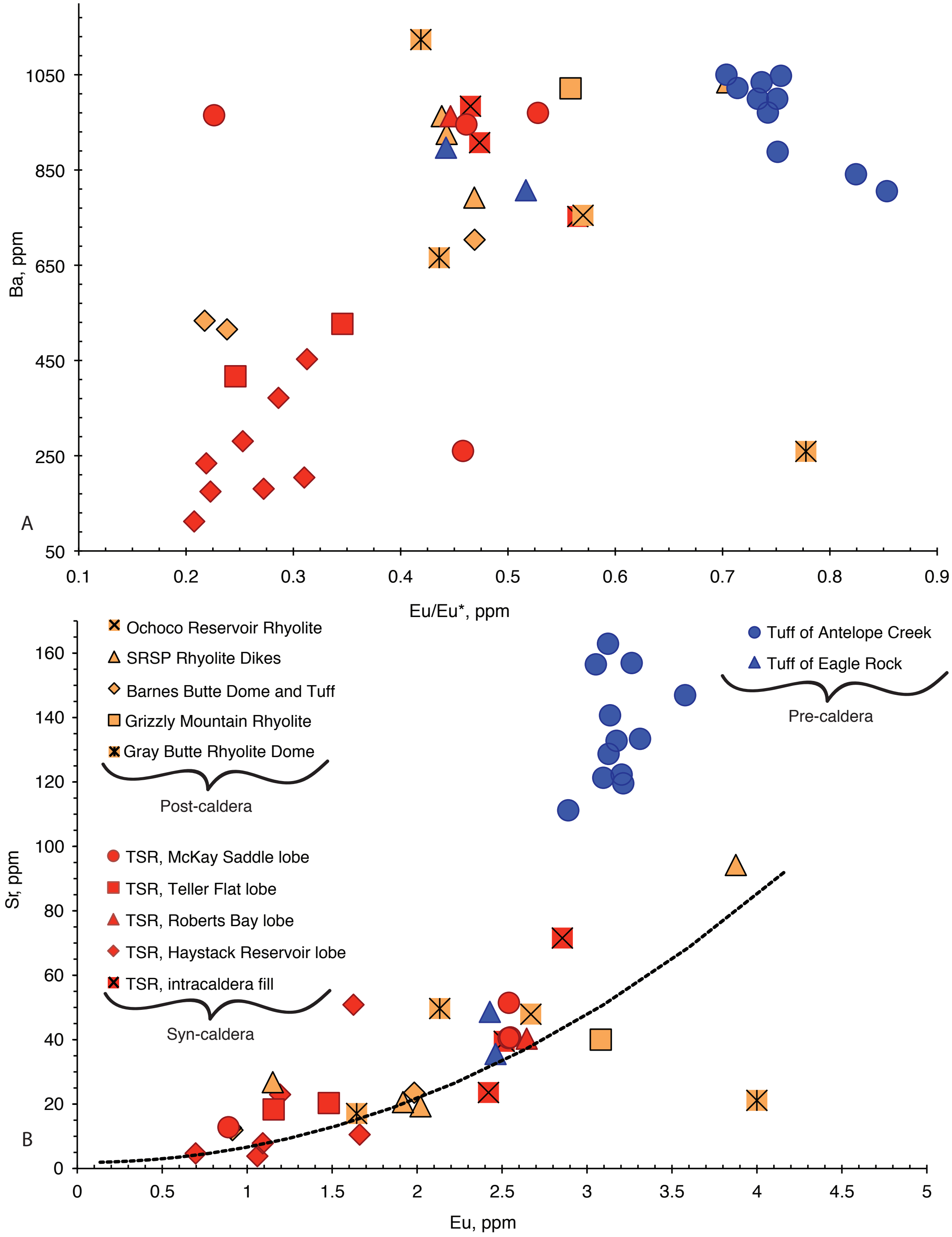

Figure 41. (A) Eu/Eu* versus Ba illustrating the increasing Ba and decreasing Eu/Eu* values of the high-Fe group, and the decreasing Ba and Eu/Eu* values of the low-Fe group. The inverse relationship between Ba and Eu/Eu* in the high-Fe group indicates Ba was likely concentrated as a consequence of plagioclase fractionation and the lack of alkali feldspar fractionation. Note Eu*= (Sm+Gd)/2. (B) Eu versus Sr illustrating decreasing Eu and Sr concentrations of the low-Fe group. Model lines calculated using D values from Bindeman and Davis (2000). Note constant Eu abundances, but decreasing Sr values of the

high-Fe may in fact indicate even lower oxygen fugacities, which would be consistent with the higher FeO contents charactertistic of the high-Fe group. Increasing Ba contents and decreasing Eu/Eu* ratios in the high-Fe group (Fig. 41A) again indicate only plagioclase fractionation, as both plagioclase and alkali feldspar fractionation would decrease Ba and Eu/Eu' values due the compatibility of Ba into alkali and plagioclase feldspars and Eu into plagioclase under reducing conditions. Therefore, alkali feldspar fractionation appears to have been important during the petrogenesis of the low-Fe group, based on Ba depletions shown in the trace element plots (Fig. 40A) and the covariation of decreasing Ba and Eu/Eu* values (Fig 41A). Overall these characteristics point to the high-Fe group being less fractionated than the low-Fe group.

The lower Th concentrations of the high-Fe group appear as Th depletions relative to Ba and U on normalized trace element plots. Th, under most conditions behaves as a highly incompatible element, unless a trace phase like monazite is present. Monazite also controls the distribution of La, which has a significantly higher partition coefficient into monazite compared Th, thus any significant fractionation of La from Th suggests the presence monazite, or another LREE sequestering trace phase like allanite or chevkinite. The fairly cohesive trend of the high-Fe group (Fig. 42A) indicates these trace phases were likely not present in the high-Fe group, and suggests the lower Th values are the results of the source rock from which they were derived. Among the low-Fe group, there are several outliers suggesting the presence of a LREE sequestering trace phases. Low La/Sm ratios and high Th values are suggestive of chevkinite fractionation (Fig. 42B), as La partitions into chevkinite over Sm due to a higher partition coefficient. Additionally, chevkinite is known to crystallize fom peralkaline melts.

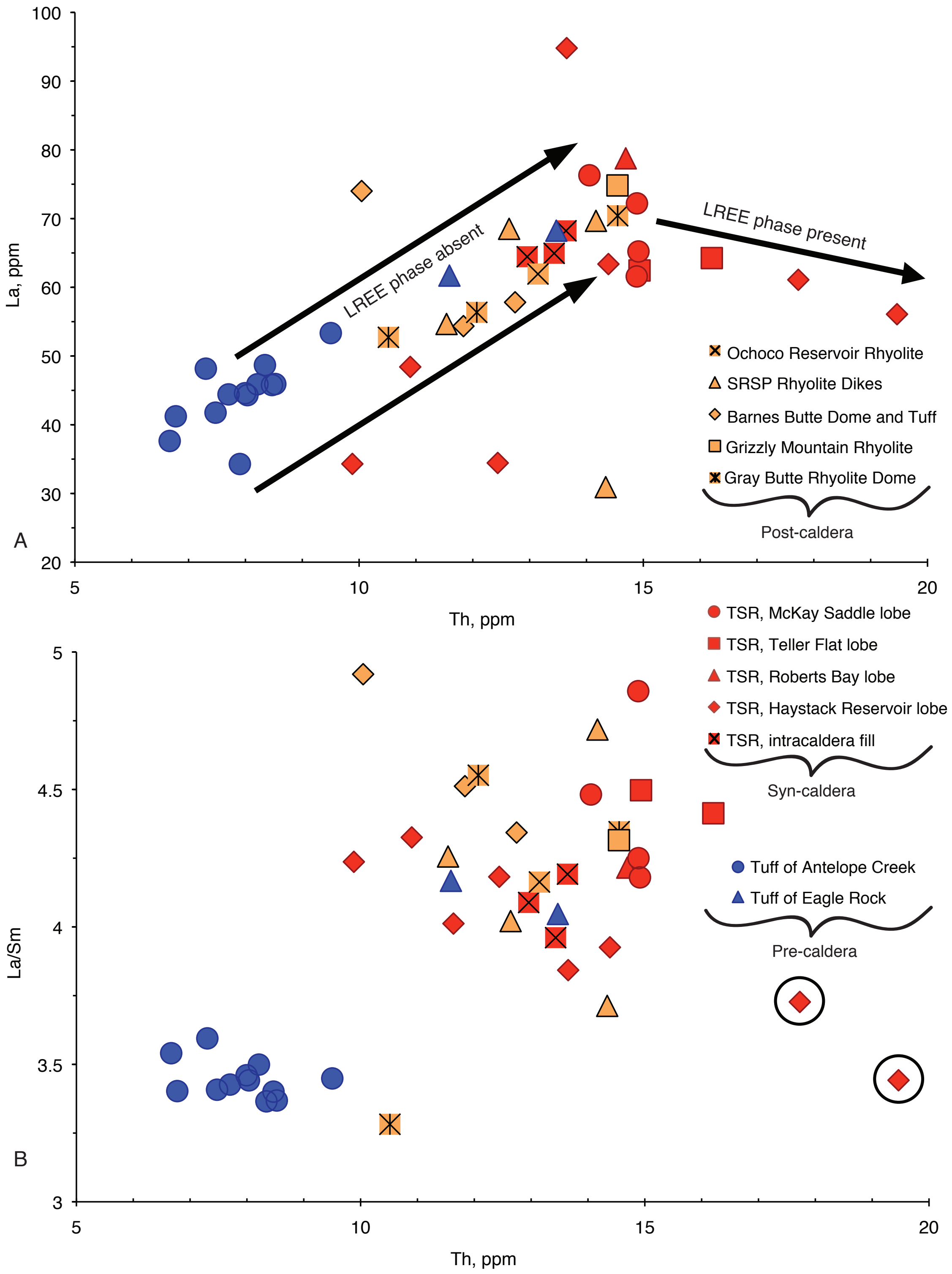

Figure 42. (A) Th versus La indicating no significant fractionation of La from Th, supporting the absence of monazite. Note the same behavior of these elements in the low Fe group, except for a few outliers. (B) La/Sm ratios versus Th illustrating the probable role of chevkinite in the most fractionated samples from the Tuff of Haystack Reservoir (as indicated by the circles).

Chemical correlations between pre-, syn- and post-caldera units

As show, the rhyolites can generally be divided into high- and low-Fe groups; however, the pre-, syn- and post-caldera units do not strictly follow the chemical divisions, as some older pre-caldera units share chemical affinities with syn- and post-caldera units, and vise versa.

Pre-caldera Tuff of Eagle Rock

The ~32.1 ± 0.7 Ma Tuff of Eagle Rock (Robinson and others, 1990) that underlies all the low-Fe syn- and post-caldera units shares very similar trace element abundances with the low-Fe group, like high Th, Nb, La, and low Fe, Sr, Eu, and Zr/Hf (see Figures 36, 38 – 42), which suggest that it was derived from a source or sources similar to the low-Fe group. Thus, a plausible suggestion is the Tuff of Eagle Rock represents an ash flow erupted from the area of the Crooked River caldera prior to the caldera forming eruption. Alternatively, the tuff could just simply represent outflow from a separate unknown vent that was derived from a similar source or sources, but its relation to the Crooked River caldera and associated units remains unclear.

The overlying Tuff of Antelope Creek is clearly chemically distinct from the Tuff of Eagle Rock and the majority of the syn- and post-caldera units. The lack of zircon fractionation in the Tuff of Antelope Creek indicate it was likely derived from a source with more developed peralkaline affinities, or attained higher magmatic temperatures compared to the low-Fe group, which likely fractionated zircon as a result of lower temperatures (see Fig. 31). Whether the Tuff of Antelope Creek represents an ash flow from a separate unknown vent is unclear. It could represent melts tapped from a chemically different system, but that were erupted from the Crooked River center prior to the caldera forming eruption. The fact that some of post-caldera rhyolite domes and lavas share peralkaline chemical similarities with this tuff, suggests they too were tapped from a more peralkaline magma chamber somewhere in the vicinity of the Crooked River caldera.

Variations among low-Fe syn-caldera units

The syn-caldera outflow lobes share overall similar compositional characteristics, and their overlapping ages suggest they are correlative and products of the 29.5 Ma Crooked River caldera, however minor variations in trace element abundances indicate slight differences in their petrogenesis. Thus, their trace element differences may be the result of melts erupted from (1) a single zoned magma chamber or (2) differently evolved magma systems tapped at once/ or within the same time frame of the Crooked River caldera eruption.

Studies of the Bandelier Tuff by Smith and Bailey (1966) and the Bishop Tuff by Hildreth (1979) and Smith (1979) established that some rhyolitic tuffs exhibit chemical zoning within a single eruptive unit. They found that co-eruptive flows showed a progressive decrease in incompatible elements upsection, and interpreted this to represent early tapping of more differentiated material near the top of the magma chamber to less differentiated material at depth in the magma chamber. Thus, if the ash flow tuffs of the Crooked River caldera represent progressive outflow from a single zoned magma chamber, they should show a systematic decrease in incompatible trace elements upsection. If the Teller Flat samples with lowest Nb concentrations are viewed to represent the least differentiated magmas tapped later from the lower parts of the Crooked River caldera magma chamber, then they should have the highest Sr and Eu abundances, however as shown in Figure 41A&B they have higher Sr and Eu abundances. Thus, the outflow does not appear to have derived from a single zoned magma chamber. Moreover, the wide and apparent random variation of Nb and Th (Fig. 43A) and other HFSE of the syn-caldera units further militates against the Crooker River caldera units being derived from a single zoned magma chamber.

Thus, the Crooked River caldera outflow either represents different systems tapped at once during the eruption of the Crooked River caldera or within the time frame of the Crooked River caldera. Either case requires a model that can explain the formation of chemically different magmatic systems within close proximity to one another.

Hildreth (2004) proposed a model to explain variable elemental differences in the Long Valley region that may be applicable to the Crooked River caldera system. His model is nontraditional in the sense that underplated basaltic magma is not the primary locus of partial melting. Rather his model envisages the direct intrusion of basaltic magmas into the crust, which causes partial melting throughout the thickness of the crust. This in turn forms a network of discrete dikes, pods and mushy differentiated intrusions throughout the crust, where ductile deformation could easily remove, add and/or mix different melts, and form several small distinct and separate magma chambers in the shallow upper crust (Fig. 44). This model is a plausible mechanism for derivation of discrete magma systems beneath and within the vicinity of the Crooked River caldera, as a network of dikes and multiple pods would promote variable degress of crustal assimilation, fractionation crystallization and magmas mixing. However, discerning whether the tuffs were erupted from a central vent that tapped multiple systems, or were erupted from multiple vents within the time frame of the Crooked River caldera eruption

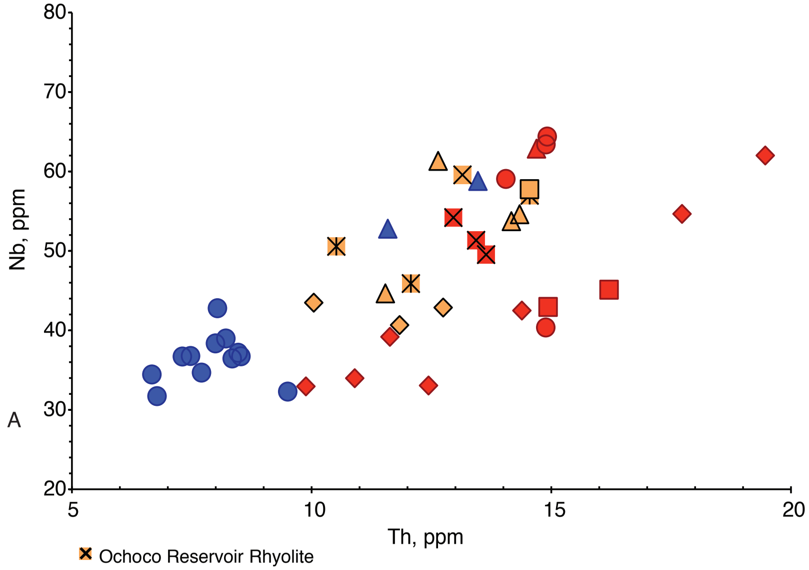

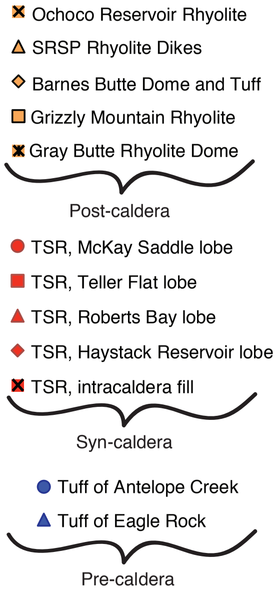

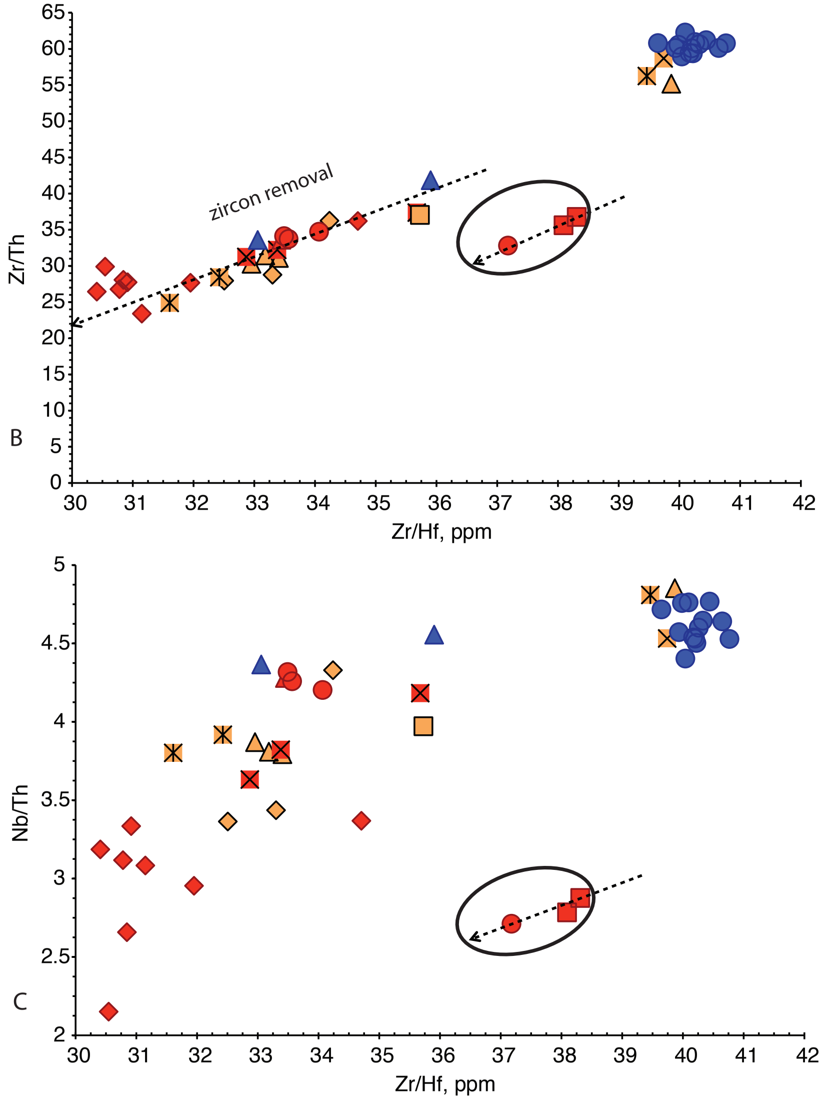

Figure 43. (A) Th versus Nb showing the high variability of Nb concentrations, which indicate the low-Fe group does not presrent products of a single zoned magma chamber. (B) and (C) Zr/Hf ratios versus Zr/Th and Nb/Th illustrating separate trends for Teller Flat lobe and sample MS3 from the McKay Saddle lobe. They mimic the trend of decreasing Zr/Th ratios for the rest of the low-Fe rhyolites, however, their higher Zr/Hf ratios of these samples suggest less zircon fracationation. The lower Nb/Th ratios sugests these units are likely unrelated to the rest of the low-Fe rhyoiltes by simple fractionational crystallization.

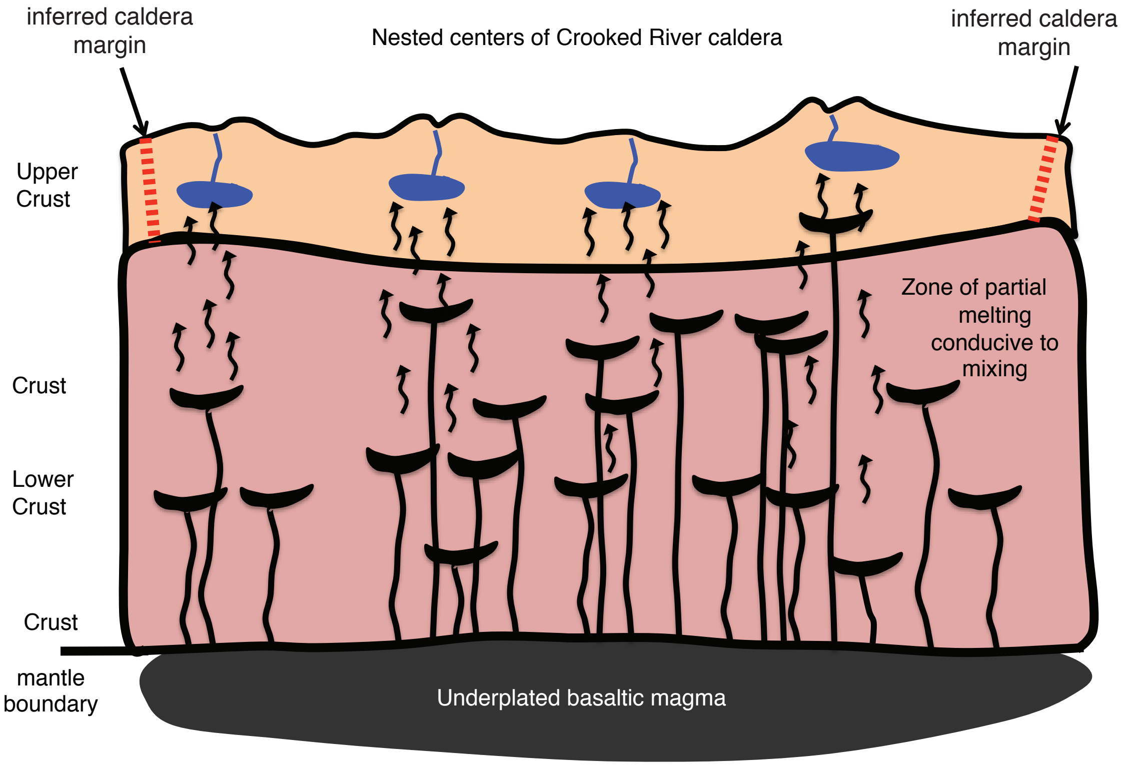

Figure. 44. Schematic illustration of the model proposed by Hildreth (2004). Rather than basaltic melts ponding at the crust-mantle boundary (underplating), the basaltic melts intrude the crust to form a network of dikes and pods, which promotes the formation of numerous chemically different magma systems within proximity to each other. Tapping of these different systems either at once or within the same times frame could explain the chemical diversity of the caldera forming units that likely contributed to the collapse of the Crooked River caldera.

is unclear. One particular chemical variation among the ash flow tuffs occurs in the Teller Flat and McKay Saddle lobes. The 29.61 ± 0.10 Ma (McClaughry and others, 2009) Teller Flat units and sample MS3 from below the 29.56 ± 0.17 Ma (McClaughry and others, 2009) capping tuff at McKay Saddle lie on a separate trend than the rest of the syn- and post-caldera low-Fe rhyolites, having lower Zr/Th (Fig. 44B) and Nb/Th (Fig. 44C) ratios displaced at higher Zr/Hf ratios. On a plot of Zr versus Nb, they lie along the trend consistent with the high-Fe group (Fig. 45A) but have Th contents more consistent with the low-Fe trend (Fig. 45B). The cause for this compositional difference is uncertain, but is consistent with the conclusion that multiple chambers were present during Crooked River time. Thus, the low-Fe syn-eruptive units do not appear to represent units erupted from a single zoned magma chamber based, but rather from a variety of systems that were either tapped at once or within the same time frame of the Crooked River caldera eruption. Additionally, the Crooked River caldera could have formed piecemeal over the course of several eruptions.

Post caldera rhyolite domes and flows

The majority of the post-caldera rhyolite domes and flows are chemical similar to the syn-caldera low-Fe group, however, as shown in Figure 38 E, F & G and 39A-D a few post-caldera samples plot along the same peralkaline trend of the high-Fe group and contain considerably higher Zr concentrations. Their similarities with the Tuff of Antelope Creek coupled with their younger age suggest they may have been tapped from the same system at different times. A plot of Th versus Zr demonstrates these post-caldera units are displaced towards higher Zr concentrations on a trend consistent with

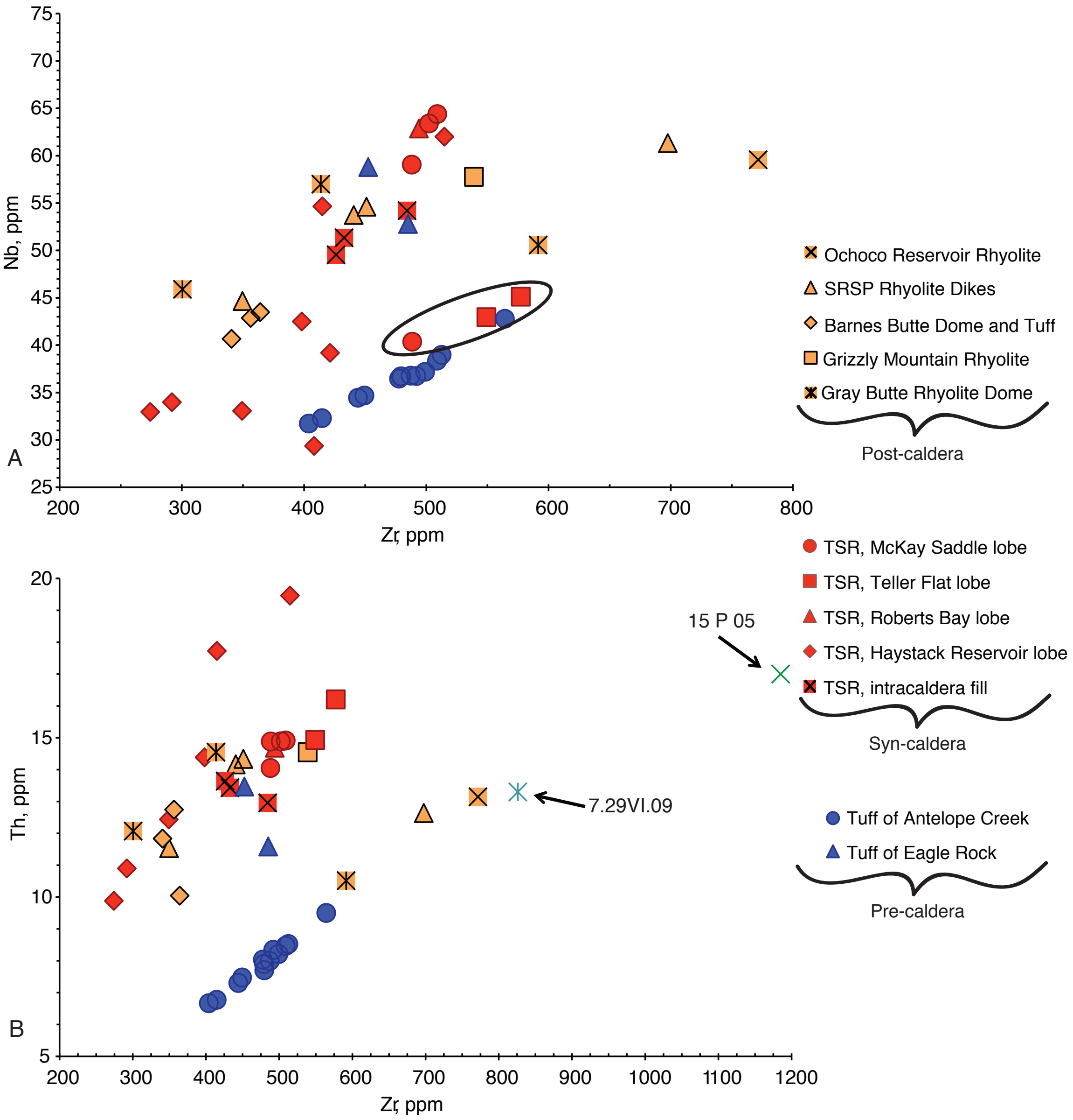

Figure 45. (A) Zr versus Nb showing that the Teller Flat lobe and sample MS3 from the McKay Saddle lobe have low Nb concentrations similar to the Tuff of Antelope Creek. (B) Zr versus Th illustrating that even though the Th contents of post-caldera peralkaline rocks overlaps with the low-Fe group, it is displaced at higher Zr, and lies on the peralkaline trend of the Tuff of Antelope Creek. Thus the Tuff of Antelope Creek appears to be less fractionated than the post-caldera peralkaline rhyolites. Samples 7.29VI.09 and 15 P 05 are from Powell Buttes, and data is from McClaughry and others (2009).

the high-Fe group (Fig. 45B). Thus, the Tuff of Antelope Creek appears to be less fractionated than the post-caldera rhyolites, which is consistent with the lower Sr and Eu concentrations and modest Eu anomalies and reasonable if the peralkaline source evolved over time (Fig. 41B). One notable difference between the more peralkaline post-caldera rhyolites that should be pointed out are the evident Fe-enrichments in samples GB353 and SR11 from the Gray Butte Rhyolite and the Smith Rock State Park Dikes. The presence of feldspar + pyroxene + Fe-oxide glomerocrysts in samples SR11 and GB353 may be relevant to the observed FeO enrichments, as Fe-oxides would increase FeO contents. Other post-caldera rhyolite domes like Powell Buttes (samples 7.29VI. 05 & 15 P 05 from McCaughry and Ferns, 2006a) on the southwest margin of the Crooked River caldera show similar Fe-enrichments (Fig. 44), however were not examined in thin section. Thus, the relation between the glomerocrysts and the Fe-enrichments remains unclear.

Discussion

Although these John Day rhyolitic ash flow tuffs, domes, and lavas are chemically different, they all share compositional affinities with A-type granites. Such compositions, to author's knowledge, have not been previously described in the JDF. This new geochemical data contradicts the long held model that JDF volcanism was directly subduction-related (Robinson, 1975; Robinson and Brem, 1981; Robinson and others, 1984; Robinson and others, 1990; Bestland and others, 1999), and indicates the need for an updated Eocene-Oligocene tectonic model for this part of Oregon.

Review of A-type granites

A-type granites occur all over the world (see Whalen et al., 1987; Eby, 1990; Pearce et al., 1984) and their petrogenesis has been the subject of much debate over the years, since the coining of the term by Loiselle and Wones in 1979. Their common distinctive features include: (1) often high magmatic temperatures (≥900°C) and relatively low magmatic H_2O contents compared to I and S type magmas, although this is not true of all A-type magmas, (2) evolution and/or crystallization in shallow subvolcanic magma chambers as evidenced by their volcanic counterparts, (3) emplacement in extensional, or at least noncompressive tectonic settings that often postdate calc-alkaline magmatism, (4) relatively low Al, Ca, Sr and Eu contents, and (5) elevated alkalis, high field strength elements (HFSE), FeO/MgO, TiO_2/MgO and Ga/Al ratios compared to calc-alkaline granites.

A-type granites are often found in the roots of large caldera volcanoes, and are commonly accompanied by volcanic equivalents that share A-type characteristics; however these volcanic equivalents have not received as much attention over the years. A-type suites are also commonly associated with basalt-rhyolite bimodal volcanism (e.g. Snake River Plain, Trans-Pecos Volcanic Province) which is thought to be the result of underplated basaltic melts at the base of the crust, that either migrate to surface and erupt with very little crustal interaction, or stall in the crust and produce granitic magmas via partial melting of the crust.

Many petrogenetic models for A-type rhyolites rely on mantle derived magmas as the primary heat source for partial melting of lower crustal rocks, but these models struggle to explain (1) diverse isotopic signatures, (2) peralkaline to sometimes peraluminous compositions and (3) significant to slight variations in major, minor and trace elements of A-type rhyolites. The residual source model, which has gained popularity over the years (Collins et al., 1982; Clemens et al., 1986; Whalen et al., 1987), suggests that A-type melts form from the melting of relatively dry, granulitic meta-igneous source rocks previously depleted in hydrous felsic melt. Caveats to this model, provided by Martin (2006), suggest a previous melting event could deplete incompatible trace elements including HFSE, but this depends on accessory phase saturation, which in turn depends on temperature and degree of melting. The importance of F is considered crucial in concentrating HFSE to some (Collins et al., 1982; Skjerlie and Johnston, 1993), but high F contents tend to favor aluminum enrichment and do not produce Al depletions or high Ga/Al ratios characteristic of A-type rhyolites (Dooley and Patino Douce, 1996). Furthermore, as shown by Patino Douce and Beard (1995, 1996), re-melting of these refractory granulitic residues do not necessarily produce granulitic liquids with high alkalis and TiO_2/MgO ratios typical of A-type granites, as these variables are depleted during prior melting. However, accessory phase saturation may play a role in controlling Ti/Mg ratios in subsequent melt generation.

Martin (2006) suggests and alternative model, whereby these refractory sources produce A-type rhyolites if “refertilized” by metasomatic processes. This petrogenetic model rests on the observation that tensional settings are areas of mantle degassing, where mantle-derived fluids rich in F, Cl and other volatiles can transport and re-enrich lower crustal rocks in HFSE, REEs and alkalis, transforming them into A-type granite compositions.

Experimental work by Patino Douce (1997) suggested that low pressure (4 kbar) incongruent melting at 950°C of hornblende- and biotite-bearing H_2O poor calc-alkaline granitoid rocks with residual plagioclase and orthopyroxene can produce granites with A-type characteristics. However, as pointed out by Christiansen and McCurry (2008) only the TiO_2/MgO ratio in Patino Douce (1997) was successful in discriminating between the A-type rhyolites of the Snake River Plain ($TiO_2/MgO>1$) and the "calc-alkaline" rhyolites of the Great Basin ($TiO_2/MgO<1$). They suggested that the high TiO_2/MgO ratios in the experiments were the result of low fO_2 rather than pressure; as low fO_2 impedes the crystallization of titanomagnetite and tends to elevate TiO_2/MgO ratios. Thus they suggest the derivation of A-type magmas are not fully controlled by source composition and/or pressure, but by the low fO_2 under which they were derived.

A-type Comparative Study

The John Day rhyolites in the vicinity of Prineville, including those associated with the Crooked River caldera, share A-type characteristics, as well as a bimodal setting with A-type rhyolites of the Central Snake River Plain (CSRP) of south-central Idaho and Trans-Pecos Volcanic Province (TPVP) of west Texas. These therefore serve as good suites with which to compare A-type characteristics.

All suites plot in the within-plate and A-type fields on granite discrimination diagrams (Fig. 46), but the John Day rhyolites have noticeably higher Ga/Al ratios than the CSRP rhyolites, while the TPVP rhyolites straddle the two groups. The higher Zr concentrations in the TPVP rhyolites are likely due to more peralkaline compositions, which leads to the increased solubility of zircon (Watson and Harrison, 1983; Miller et al., 2003) in silicate melts. Bonin (1988) noted higher Ga/Al ratios in peralkaline over

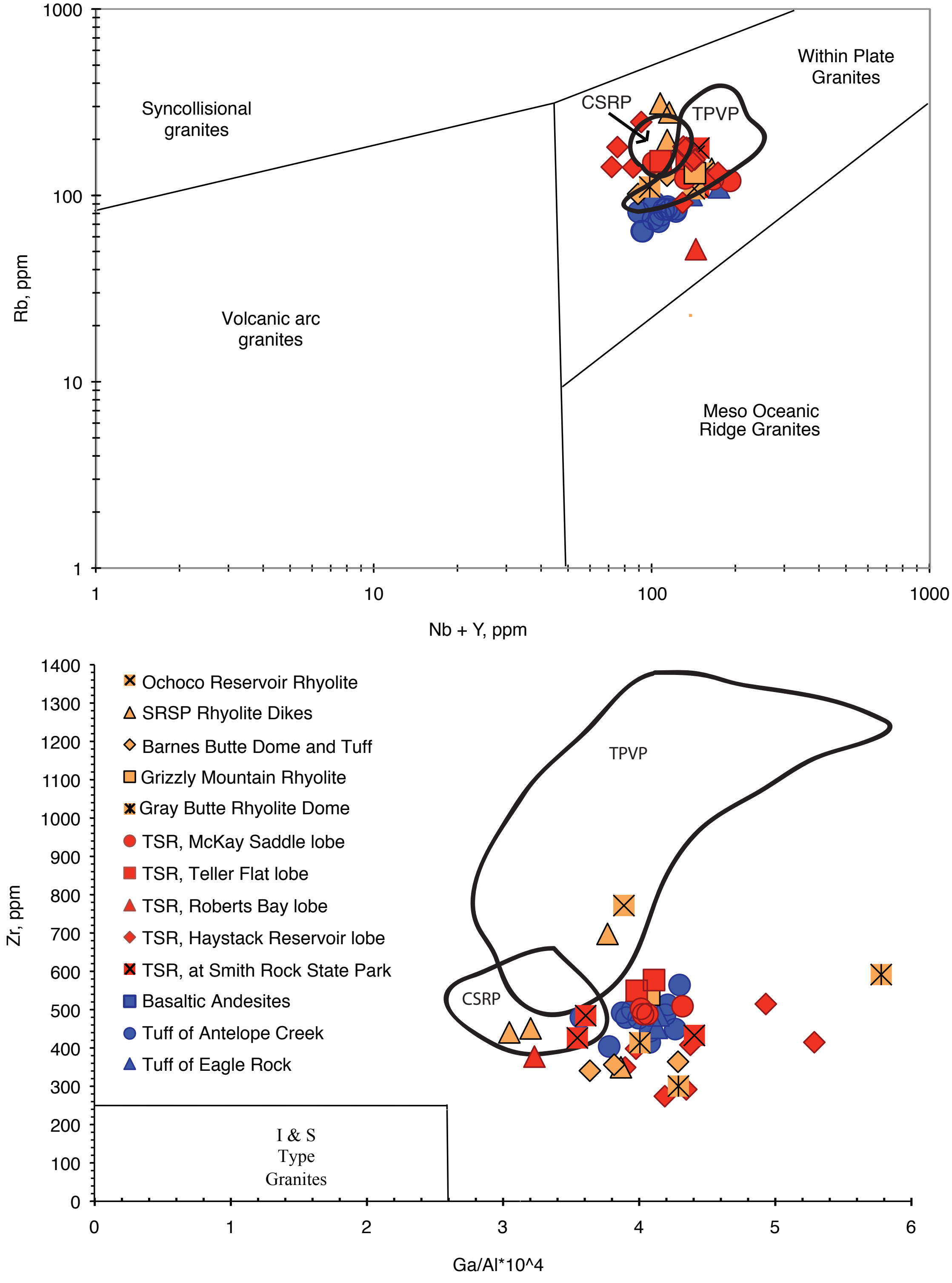

Figure 46. Granitoid discrimination diagrams illustrating overall similarity of these John Day-age rhyolites with CSRP and TPVP rhyolites. CSRP data from Boroughs (2003), Boroughs and others (2005) and TPVP data from Giles (unpublished data). Abbreviations as follows: TSR = Tuff of Smith Rock, SRSP = Smith Rock State Park.

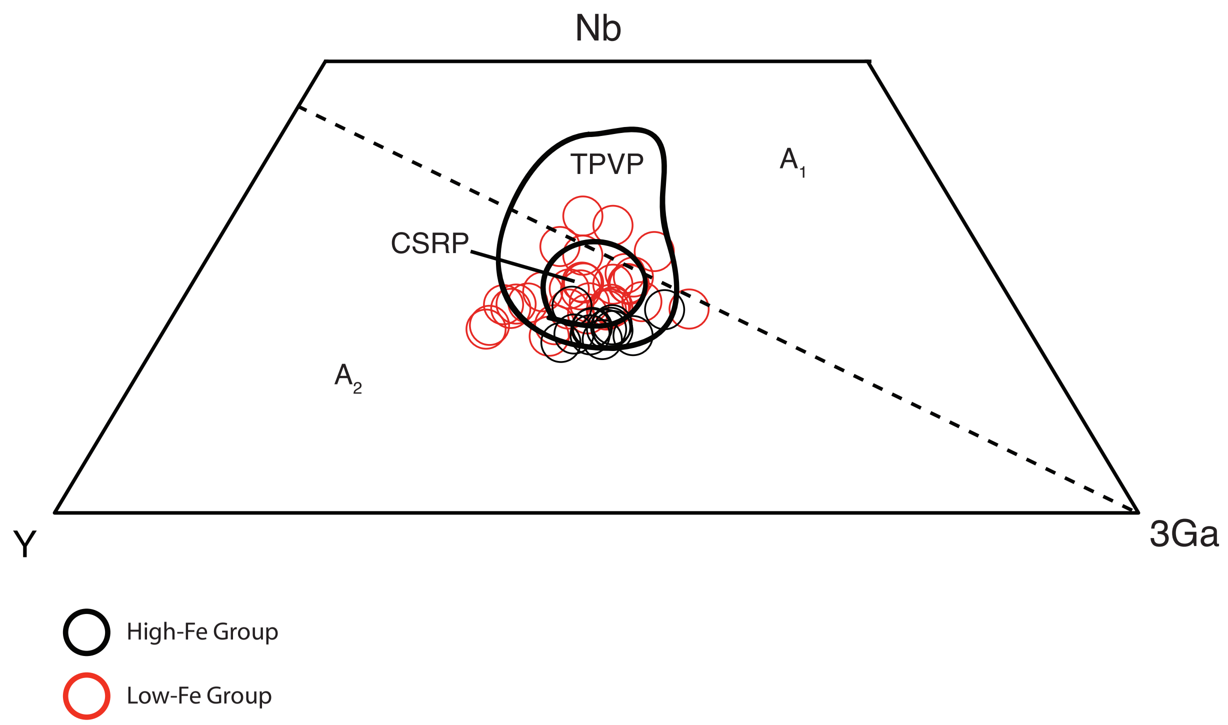

FIgure 47. Ternary Nb-Y-3Ga plot from Eby (1992) indicating a dominant A_2 for the John Day rhyolites, while the CSRP (blue boundary) and TPVP (green boundary) rhyolites staddle the two boundaries.

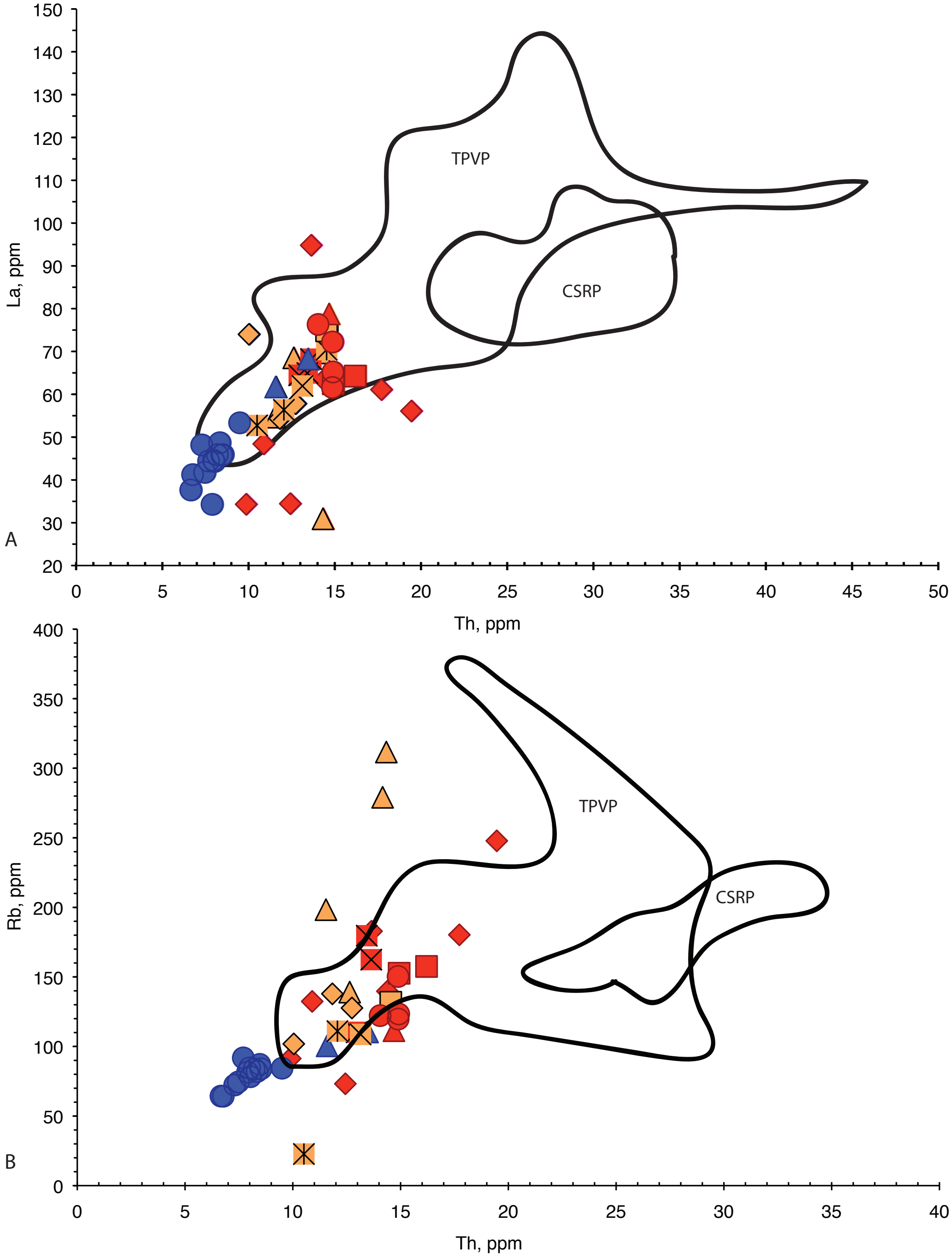

Figure 48. La and Rb versus Th illustrating the chemical differences between the John Day rhyolites and the CSRP and TPVP rhyolites. Note significantly lower La, Rb, and Th abundances for the John Day rhyolites compared to the CSRP rhyolites, while the TPVP rhyolites span values of each suite.

metaluminous granites, which may explain why the John Day and TPVP have higher Ga/Al ratios. On the ternary Nb-Y-3Ga plot (Fig. 47) of Eby (1992) the three suites overlap, but the CSRP rhyolites are less variable than the John Day and TPVP rhyolites and lie within the A_2 field, while the others straddle the A_1-A_2 boundary (see previous chapter for explanation of Eby's classification). In addition to differences on A-type discrimination diagrams, there are notable chemical variations between the suites. The John Day rhyolites have lower large ion lithophile elements (LILE), such as Rb, Th and La (Fig. 48) compared to the CSRP rhyolites, while the TPVP rhyolites span the range of both suites, but are more similar to the John Day rhyolites.

Rare earth element and trace element plots indicate additional differences between the suites. Figure 49A&B illustrates LREE enrichment of the CSRP and TPVP rhyolites compared to the John Day high-Fe rhyolites; however the CSRP rhyolites display an overall steeper REE slope and stronger HREE depletions compared to the TPVP and John Day rhyolites. The CSRP and TPVP rhyolites have more negative Eu anomalies similar to the low-Fe group as a result of more plagioclase fractionation and generally being more fractionated. Trace element plots (Fig. 49C&D) reveal all suites have variable Sr, P and Ti depletions consistent with plagioclase, apatite and Fe-oxide removal, with the high-Fe John Day rhyolites being the least depleted in these elements, and the TPVP and low-Fe group appearing more depleted. Prominent Ba depletions relative to Rb and Th tend to increase from CSRP, to John Day low-Fe, to the TPVP rhyolites, indicating increasing amounts of alkali feldspar fractionation or variable amounts of feldspar in the source region. The degree of Zr and Hf enrichment indicates stronger peralkaline compositions as a result of no zircon fractionation.

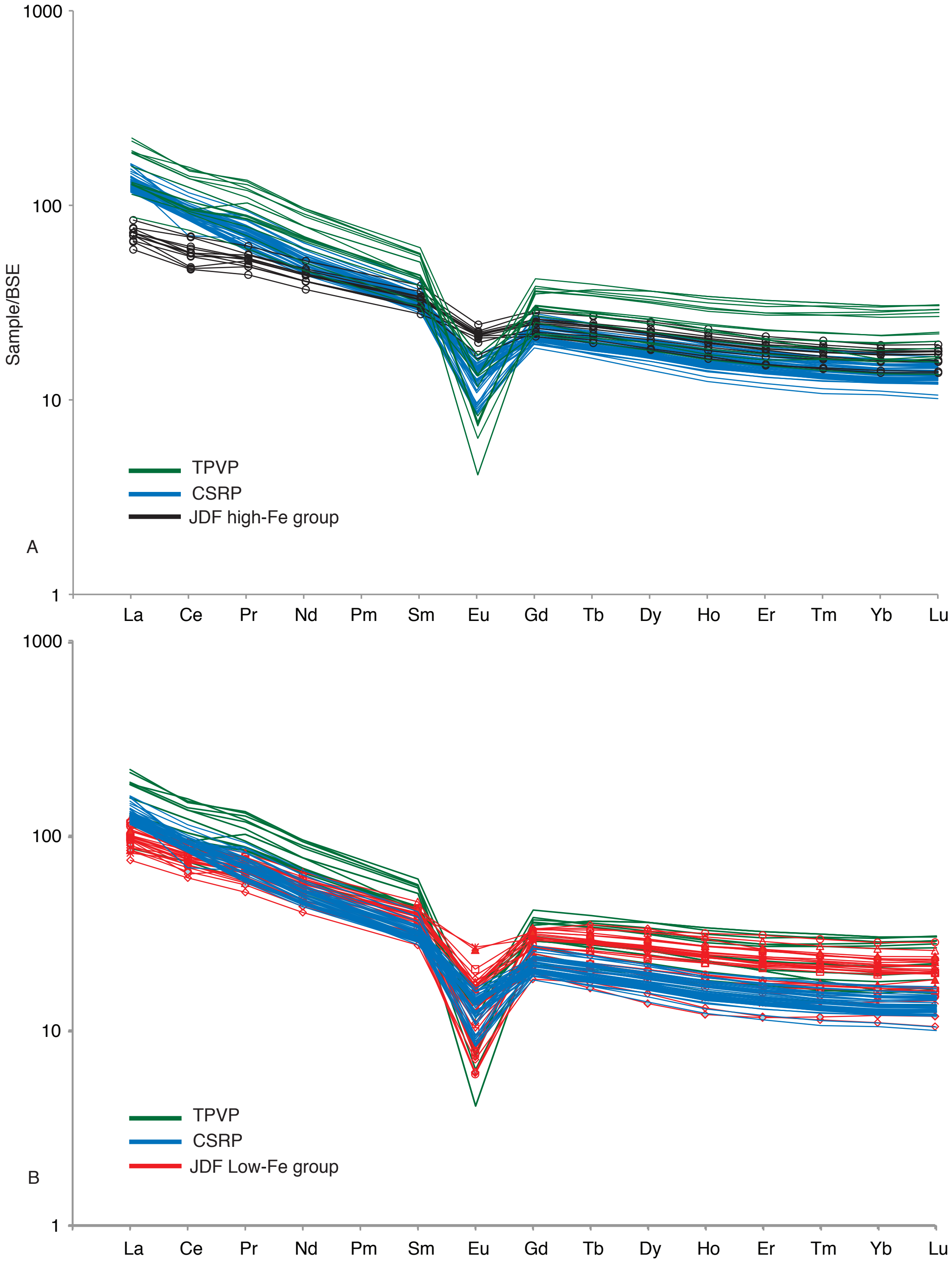

Figure 49. (A) & (B) Rare earth element plots of CSRP, TPVP and John Day high- and low-Fe groups. See text for discussion. Note steeper slope of CSRP rhyolites.

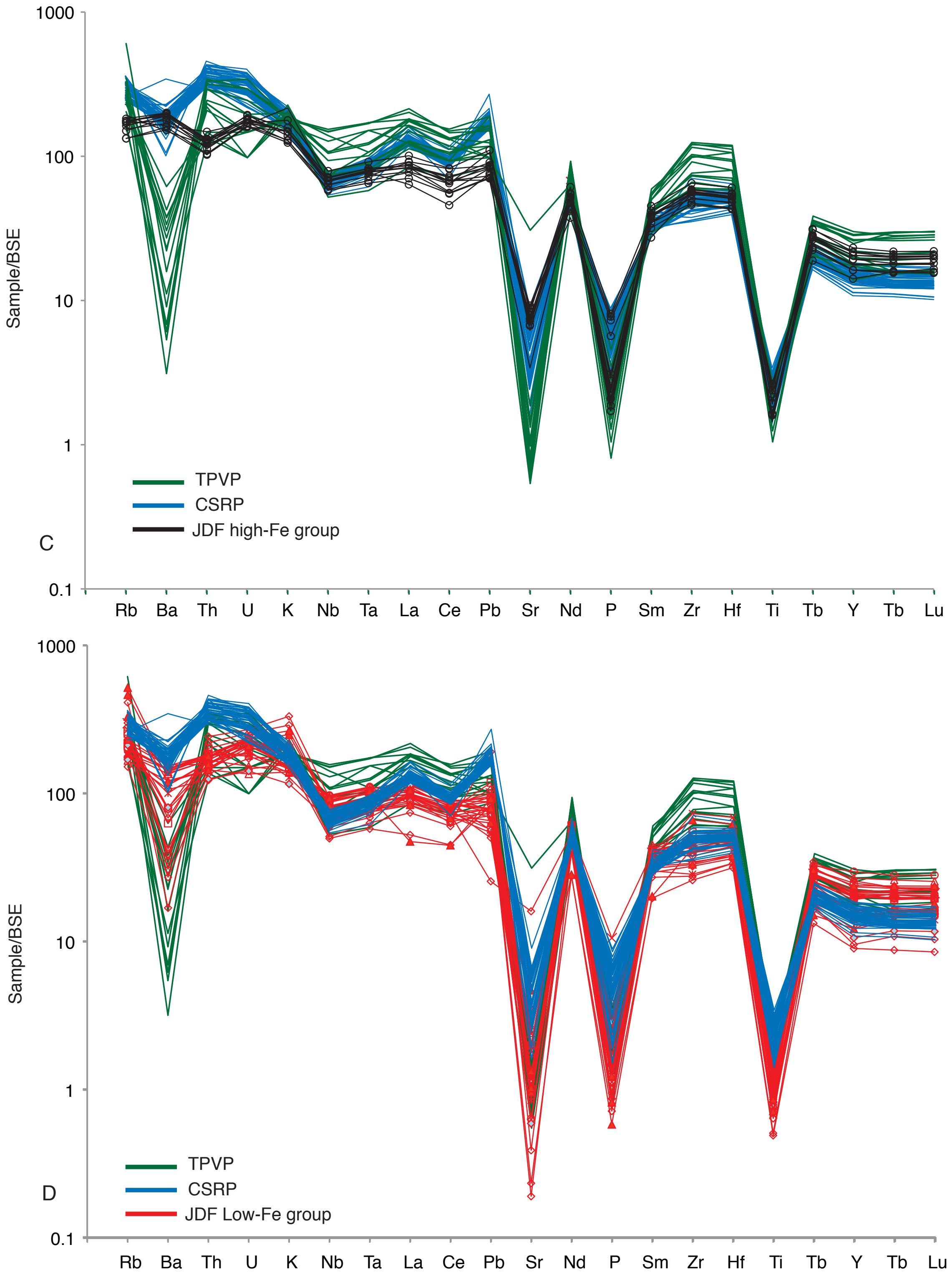

Figure 49 cont. (C) and (D) Trace element plots of CSRP, TPVP and John Day high- and low-Fe groups. See text for discussion.

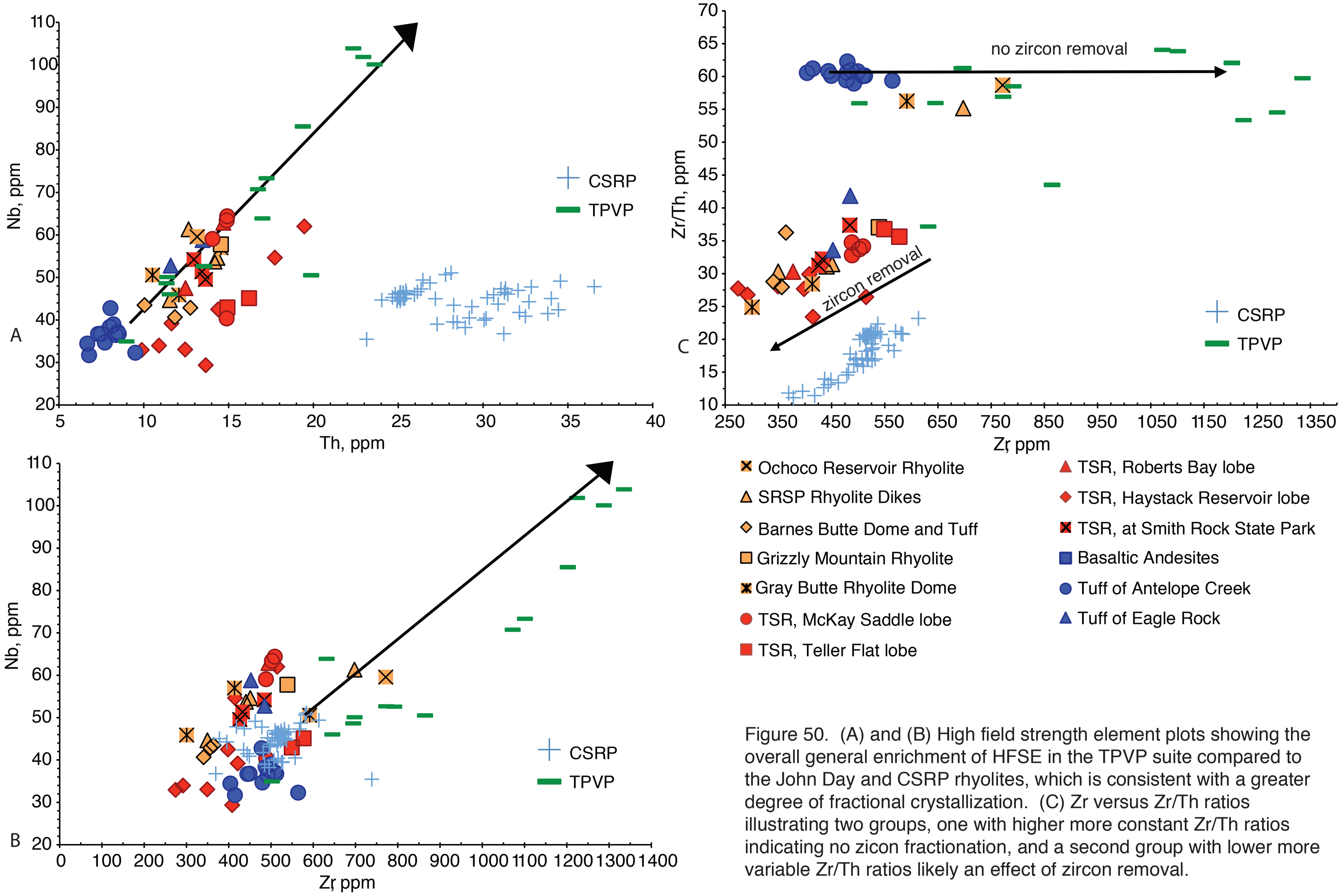

Figure 50. (A) and (B) High field strength element plots showing the overall general enrichment of HFSE in the TPVP suite compared to the John Day and CSRP rhyolites, which is consistent with a greater degree of fractional crystallization. (C) Zr versus Zr/Th ratios illustrating two groups, one with higher more constant Zr/Th ratios indicating no zicon fractionation, and a second group with lower more variable Zr/Th ratios likely an effect of zircon removal.

Overall the John Day rhyolites appear to be more similar to the TPVP rhyolites on HFSE covariation diagrams and degree of slope on REE plots. The higher HFSE abundances, especially Zr of the TPVP rhyolites are likely the result of higher degrees of fractional crystallization. Therefore, the JDF rhyolites overlap with the least evolved TPVP rhyolites. Figure 50 demonstrates the two trends for the John Day rhyolites; one trend with constant Zr/Th ratios consistent with the TPVP rhyolites and a second trend with more variable decreasing Zr/Th ratios consistent with the CSRP rhyolites. The trend with the constant Zr/Th ratios indicates more peralkaline compositions with higher Fe; the slight negative slope may be the result of clinopyroxene fractionation as Zr partitions more strongly into clinopyroxene than does Th in felsic liquids. The less Fe-rich rocks correspond to decreasing Zr/Th ratios indicative of zircon fractionation and are more similar to the CSRP rhyolites, and are likely the result of being less peralkaline.

Tectonic Implications for John Day volcanism

The striking chemical similarities between TPVP and John Day rhyolites suggest similar processes were involved in their petrogenesis; which in turn are likely related to the tectonic setting and stress regime under which each was derived. Both provinces generally formed within the accreted terranes of the western United States, thus both provinces are underlain with accreted terranes that likely influenced the geochemical compositions of the parental melts. The John Day and TPVP rhyolites show high variability on the ternary Nb-Y-3Ga plot of Eby (1990, Fig. 47), straddling the A_1 and A_2 boundary, which are interpreted to represent more OIB sources emplaced in continental rifts or intraplate magmatism, versus derivation from sources that represent continental or underplated crust that has been through a cycle of continent-continent collision or island arc magmatism. Thus, the overlap of the John Day and TPVP rhyolites in both A_1 and A_2 fields suggests the accreted arc terranes were likely contaminants to asthenospheric melts, and the variation from A_1 to A_2 types may be a function of the amount and/or type of accreted terrane involved in the petrogenesis.

The best approximation of pre-Tertiary basement in central Oregon comes from the presence of limestone lithics, some bearing Permian fusulinids in the Tuff of Smith Rock intracaldera fill at Smith Rock State Park. The Permian fusulinids suggests the area is underlain with marine sedimentary rocks of the Baker terrane. However, identiftying specific terrane components are difficult, given the complexity of the Baker terrane. Thus, a clear picture and understanding of subsurface geology in central Oregon is lacking.

The TPVP also shares compositional changes observed from Clarno-John Day volcanism. TPVP studies of Henry and Price (1986), Henry and others (1991) and James and Henry (1991) illustrated that the compositional changes in the TPVP are related to changing stress regimes. Their use of common parameters; e.g. Zr/Nb, Y/Nb and Ba/Nb ratios, for distinguishing arc from intraplate mafic magmatism constrained the stress regime shift in that region to between 31-28 Ma, coincident with collision of the East Pacific Rise with the paleotrench, and a change from a convergent to a transform margin. However, recent work suggests that extension may have began later (~36 Ma), and that "arc-like" rocks reflect passive continental rifting over a foundering subducted slab (Lawton and McMillan, 1999; McMillan and others, 2000; Chapin and others, 2004; McIntosh and Chapin, 2004). This change in stress and tectonic setting are similar to those that have been postulated by White and Robinson (1992) for the transition from

Clarno to John Day volcanism in central and eastern Oregon; however the timing of this event is poorly constrained. Bestland and others (1999) suggested a slab rollback model in which high angle subducted oceanic lithosphere sweeps backward away from the arc region causing the overlying plate to thin and develop back arc extension (Fig. 51). However, their model is too general and lacks the necessary data to support it. More work is needed to constrain and better understand the tectonic and stress regimes changes in central and eastern Oregon during the Eocene and Oligocene.

Stress changes in TPVP and much of the southwestern United States have broadly been attributed to post-Laramide removal of the Farallon slab; though the manner in which the slab was removed from the continental interior is not well explained. Post-Laramide activity in the southwest began at ~40 Ma in west Texas with TPVP volcanism and propagated west-northwest (Christiansen and Yeats, 1992), while activity in the northwest propagated south, starting in northern Washington and central Idaho at 55-50 Ma, passing through northern Nevada and Utah at ~40 Ma, and meeting southwestern activity around ~20 Ma (Armstrong and Ward, 1991, Christiansen and Yeats, 1992). Humphreys (1995) proposed several slab removal models consistent with the magmatic trend, but preferred a model that involving buckled subducted slab. He proposed that tearing of the subducted slab at the northern and southern boundaries of the United States caused the separated edges to move towards one another, creating a central region of downwelling that propagated northward (Fig. 52). The relative timing of tearing is likely related to initial magmatic activity and its progressive propagation. The other models, double sided rollback, or double sided delamination also produces the observed pattern of magmatism. Nonetheless, the removal of the subducted Farallon plate caused an ascent

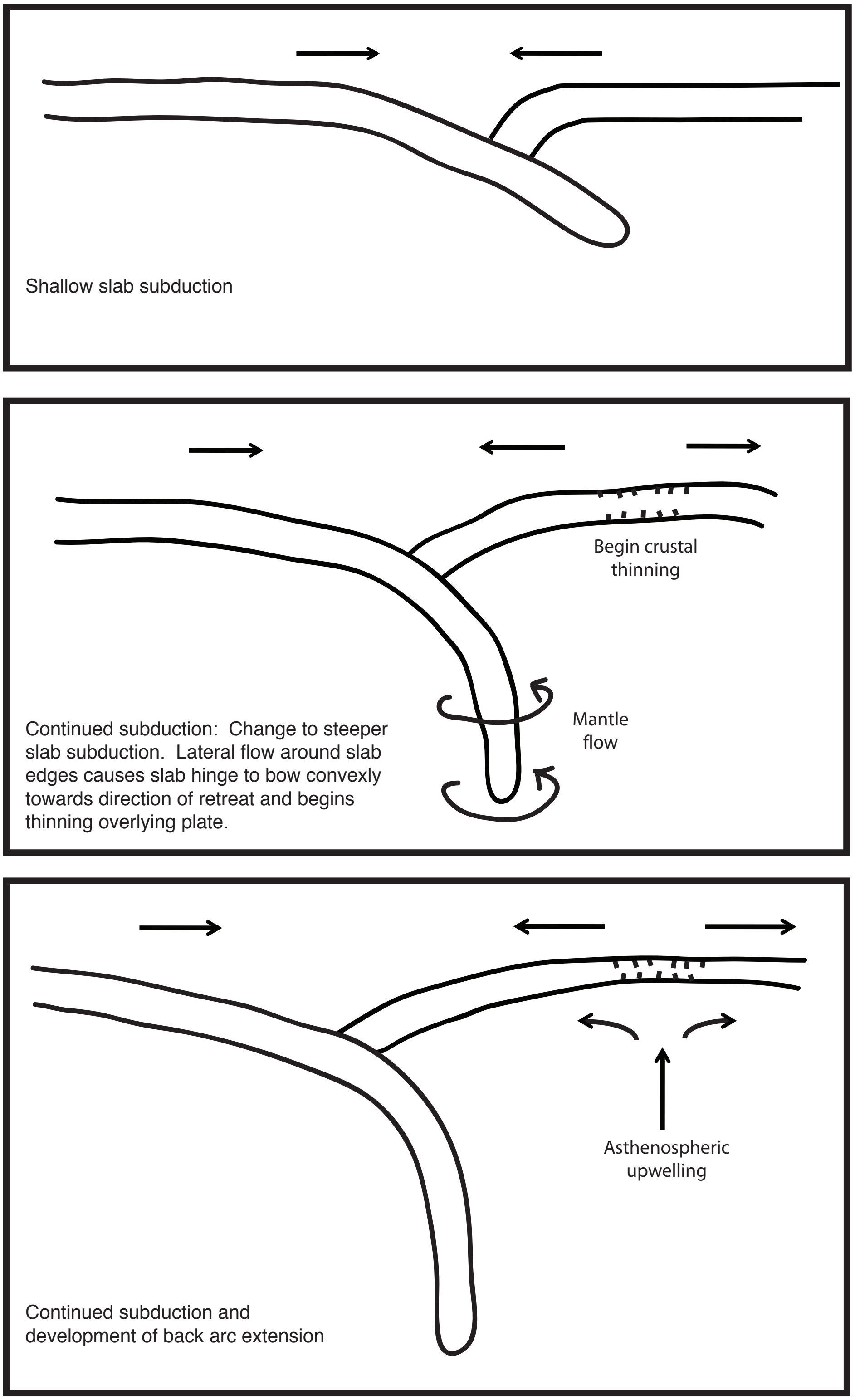
Shallow slab subduction

Continued subduction: Change to steeper slab subduction. Lateral flow around slab edges causes slab hinge to bow convexly towards direction of retreat and begins thinning overlying plate.

Continued subduction and development of back arc extension

Figure 51. Schematic illustrating the progression of slab rollback as a mechanism for developing back-arc extension during the transition from Clarno to John Day volcanism.

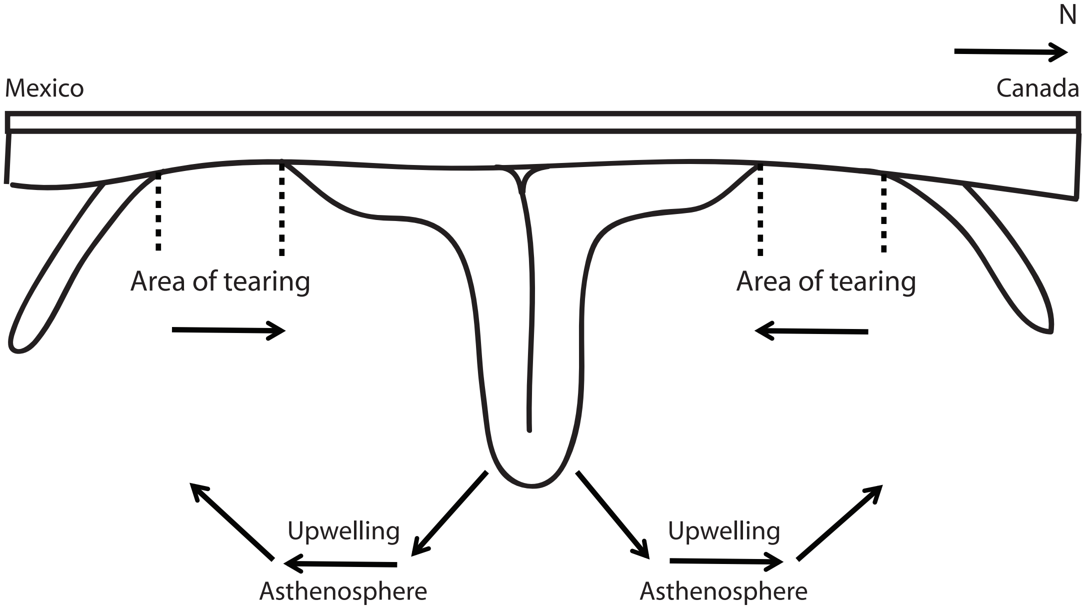

FIgure 52. Schematic of tearing and buckeling of subducted Farallon slab (Modified after Humphreys, 1995). Rate of tearing from S and N directions is directly related to the initiation and progression of magmatic activity in the western United States.

of asthenospheric mantle, which played a significant role in the progression of magmatic history throughout the western United States.

The obvious similarities between John Day and TPVP rocks and magmatism have implications for developing a volcano-tectonic model for Clarno-John Day volcanism. Besides sharing similar geochemical characteristics and tectonic settings, both provinces share transitional “arc-like” to more alkaline mafic rocks in close association with mild to strongly peralkaline rhyolitic compositions in a bimodal setting, and formed numerous large caldera systems that erupted extensive amounts of rhyolitic ash flow tuffs, some of which display A-type characteristics. Moreover, the overlapping ages, and diffuse contact between Clarno and John Day volcanism suggests that Clarno to John Day volcanism should be viewed as a single magmatic province that changed gradually over time, and not as discrete steps. The model for post-collisional and post-orogenic magmatism summarized by Bonin (2004, Fig. 53) was use to describe the tectonic history of the TPVP. Therefore, based on the striking similarities of the TPVP and John Day rhyolites, the same model may be applicable to explain the transition from Clarno to John Day volcanism, with minor adjustments to account for relative differences in peak activity and geochemical compositions as a result of changing stress regimes and magma sources.

The initial “Collision” phase (“Normal subduction” of Lawton and McMillan, 1999) consists of relatively flat slab subduction from <100 Ma to roughly 55 Ma and results in the accretion of pre-Tertiary terranes (see geologic history chapter for descriptions of these terranes) and emplacement of numerous plutons. At roughly 55 Ma,

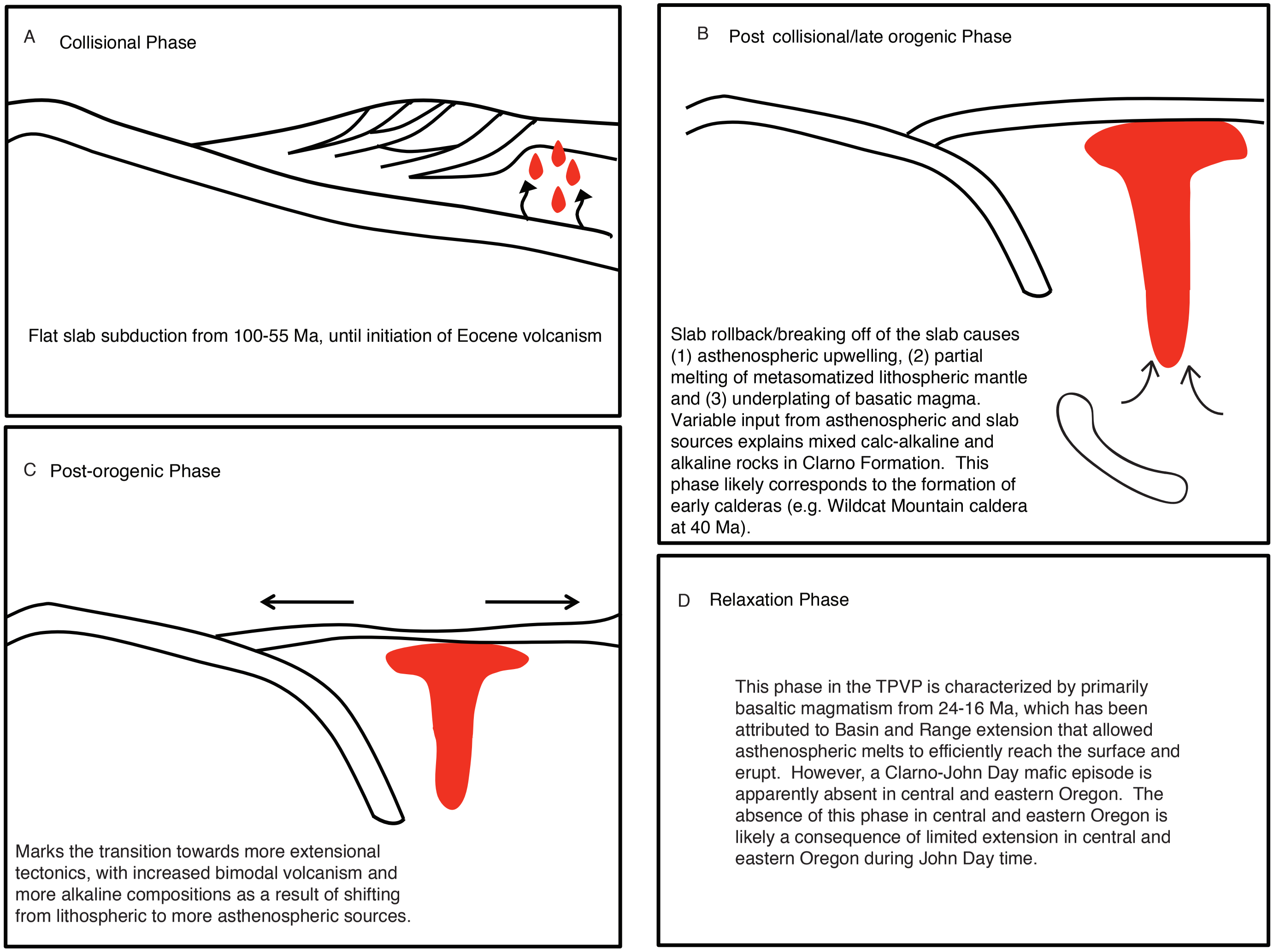

A Collisional Phase

Flat slab subduction from 100-55 Ma, until initiation of Eocene volcanism

B Post collisional/late orogenic Phase

Slab rollback/breaking off of the slab causes (1) asthenospheric upwelling, (2) partial melting of metasomatized lithospheric mantle and (3) underplating of basatic magma. Variable input from asthenospheric and slab sources explains mixed calc-alkaline and alkaline rocks in Clarno Formation. This phase likely corresponds to the formation of early calderas (e.g. Wildcat Mountain caldera at 40 Ma).

C Post-orogenic Phase

Marks the transition towards more extensional tectonics, with increased bimodal volcanism and more alkaline compositions as a result of shifting from lithospheric to more asthenospheric sources.

D Relaxation Phase

This phase in the TPVP is characterized by primarily basaltic magmatism from 24-16 Ma, which has been attributed to Basin and Range extension that allowed asthenospheric melts to efficiently reach the surface and erupt. However, a Clarno-John Day mafic episode is apparently absent in central and eastern Oregon. The absence of this phase in central and eastern Oregon is likely a consequence of limited extension in central and eastern Oregon during John Day time.

Figure 53. Schematic illustrating the post-collisional and post-orogenic model of Bonin (2004) as applied to the Clarno-John Day magmatic episode. Boxes A-D represent the four different phases of the model, refer to text wthin each individual box for explanation of the processes involved in each phase.

Eocene magmatism begins in the continental interior and Clarno magmatism initiates. However, the exact timing of Clarno activity is somewhat unclear as they overlap in age and composition with other Eocene arc volcanics in northern Idaho, Wymoning and Montana.

The next "post-collisional or late orogenic" phase ("Early Slab-Retreat" of Lawton and McMillan, 1999) represents slab roll back or breaking off of the subducting slab, which results in asthenospheric upwelling, partial melting of fluid metasomatized lithospheric mantle, and subsequent melting of lower crustal rocks by underplated basaltic magmas. This phase is likely represented by the formation of early large calderas; e.g. Wildcat Mountain caldera in northeastern Oregon (40 Ma, McClaughry and others, 2009) in northeast Oregon and transition towards more alkaline and less calc-alkaline compositions exemplified by the Clarno Formation. The next "Post-orogenic" ("Early Asthenospheric magmatism" of Lawton and McMillan, 1999) phase overlaps with the previous phase and the shift between these two phases should be considered continual. The "Post-orogenic" phase marks the early stages of extension, though the mechanism of extension is still unclear, and is characterized by notable increases in bimodal volcanism and more peralkaline compositions consistent with John Day volcanism. This phase also coincides with a shift in stress, from compression or neutral to extension, and switch towards more asthenospheric sources.

The last phase, the "Relaxation" phase, is marked primarily in the TPVP by mafic volcanism that occurred between 24-16 Ma (James and Henry, 1991). This mafic magmatism is attributed to Basin and Range extension, which allowed asthenospheric melts to efficiently reach the surface and erupt. However, the Clarno-John Day mafic episode is apparently absent, suggesting that crust in central and eastern Oregon did not experience enough extension to allow large amounts of these melts to reach the surface.

Alternatively, the emplacement of the earliest Columbia River Basalts (CRB, 16.6 Ma) in the Oregon Plateau may be somewhat related to the preceding chain of events. CRB magmatism has largely been attributed to a mantle plume, but Smith (1992) suggested back-arc extension as mechanism for CRB volcanism. He proposed that progressive development of back arc convection beneath the rotated, sheared and attenuated terranes of the Blue Mountains could eventually lead to thermal failure of the subcontinental lithosphere, and pull older Proterozoic subcontinental lithosphere on the east into the area of active melting. This relation of Clarno-John Day-CRB volcanism is purely speculation, but thought provoking to say the least. This relationship, if even plausible, may be better clarified with further investigation of the volcanic activity in the region between 20 and 17 Ma.

Conclusions

Major and minor trace element concentrations indicate that the John Day rhyolites exposed in the vicinity of Prineville are the products of at least two different sources that evolved independently from one another, but share overall diagnostic properties of other A-type rhyolites. Major differences between the groups are:

- The high-Fe group represents more peralkaline melts compared to the low-Fe group, based on the constant Zr/Hf and Zr/Th ratios that indicate no zircon fractionation. While the low-Fe group less peralkaline based on variable Zr/Hf ratios, as well as decreasing Zr/Th ratios.

- The high-Fe group tends to be less depleted in Sr and Eu and less enriched in Th, Rb, Nb, Hf compared to the low-Fe group, which indicates they are derived from at least two different sources.
- Both groups fractionated plagioclase, but the high-Fe group likely fractionated less or had less residual plagioclase in the source as evidenced by their less negative Eu depletions and less depleted Sr and Eu concentrations. Only the low-Fe group appears to have fractionated alkali feldspar based on their significant Ba depletions. Thus, the high-Fe group is less fractionated than the low-Fe group.
- The high-Fe group inherited lower Th and Hf concentrations from the source rock from which they were derived, and not from fractional crystallization of LREE sequestering phases or zircon. Only the low-Fe group shows elemental variations that indicate these phases were present.

More work is needed to better understand the chemical differences in the syn-caldera outflow, and clarify whether or not they represent synchronous tapping of multiple differently evolved magma systems or were tapping from different centers within the time frame of the Crooked River caldera. The occurrence of pre- and post-caldera rhyolites with stronger peralkaline affinities indicates the peralkaline source was persistent in the area before and after the Crooked River caldera-forming eruption.

The striking similarities between Tran-Pecos and Clarno-John Day magmatic evolution suggests the Clarno and John Day Formations should be viewed as a single magmatic province related to changing stress regimes in central and eastern Oregon that are likely related to post-Laramide removal of the Farallon slab; though the manner of slab removal remains unclear. Nonetheless, its removal caused the ascent of asthenospheric mantle, which played a significant role in the progression of magmatic history throughout the western United States.

The major, minor and trace element abundances of these John Day rocks indicate a petrogenetic history that until this study has been poorly understood. Additional work will refine petrogenetic and tectonic models for Late Eocene to Early Miocene John Day volcanism in central Oregon and will provide a context for comparison with similar aged volcanism elsewhere in the western US cordillera.

REFERENCES CITED

Appel, M., 2001. Alkaline and peraluminous intrusives in the Clarno formation around Mitchell, Oregon: Ramifications on magma genesis and subduction tectonics [M.S. thesis] Corvallis,Oregon State University, 222 p.

Armstrong, R. L., Taubeneck, W. H., and Hales, P. O., 1977. Rb-Sr and K-Ar geochronology of Mesozoic granitic rocks and their Sr isotopic composition, Oregon, Washington and Idaho: Geological Society of America Bulletin, v. 88, p. 397-411.

Armstrong, R. L., 1978. Cenozoic igneous history of the U.S. Cordillera from lat 42° to 49° N., chap. 12 of Smith, R.B., and Eaton, G. P., eds., Cenozoic tectonics and regional geophysics of the western Cordillera: Geological Society of America Memoir 152, p. 265-282.

Armstrong, R. L., and Ward, P., 1991. Evolving geographic patterns of Cenozoic magmatism in the North America Cordillera: The temporal and spatial association of magmatism and metamorphic core complexes: Journal of Geophysical Research, v. 96, p. 13,201–13,224.

Best, M .G., and Christian, E. H., 1991. Limted extension during peak tertiary volcanism, Great Basin of Nevada and Utah: Journal of Geophysical Research, v. 96, p. 13509-13528.

Bestland, E. A., Hammond, P. E., Blackwell, D. L. S., Kays, M. A., Retallack, G. J., and Stimac, J., 1999. Geologic framework of the Clarno Unit, John Day Fossil Beds National Monument, Central Oregon: Oregon Geology, v. 61. no. 1, p. 3-19.

Bindeman, I. N., and Davis, A. M., 2000. Trace element partitioning between plagioclase and melt; investigation of dopant influence on partition behavior: Geochimica et Cosmochimica Acta, v. 64, Issue 16, p. 2863-2878.

Bishop, E. M., 1989. Smith Rock and the Gray Butte complex, Oregon Geology, v. 15 no. 4, p. 75-80.

Blome, C. D., and Nestell, M. K., 1991. Evolution of a Permo-Triassic sedimentary mélange, Grindstone terrane, east central Oregon: Geological Society of America Bulletin, v. 103, p. 1280-1296.

Bonin, B., 1988. Peralkaline granites in Corsica: some petrological and geochemical constraints. Rendiconti della Societa italiana di Mineralogia e Petrologia 43, 281-306.

Bonin, B., 2004. Do coeval mafic and felsic magmas in postcollisional to within-plate regimes necessarily imply two contrasting, mantle and crustal, sources? A review: Lithos v. 78, p. 1–24.

Bonin, B., 2007. A-type granites and related rocks: Evolution of a concept, problems and prospects: Lithos, v. 97, p. 1-29.

Boroughs, S. P., 2003. Large Scale Low $\partial^{18}O$ Rhyolite Volcanism, Bruneau-Jarbridge Volcanic Field Idaho [M.S. thesis] Pullman, Washington, Washington State University.

Boroughs, S. P., Wolff, J. A., Bonnichsen, B., Godchaux, M., Larson, P., 2005. Large-volume, low-$\partial^{18}O$ rhyolites of the central Snake River Plain, Idaho: Geology, v. 33, Issue 10, p. 821-824.

Brooks, H. C., 1979a. Geologic map of the Huntington and part of the Olds Ferry quadrangles, Baker and Malheur Counties, Oregon: Oregon Department of Geology and Mineral Industries Geological Map Series GMS-13, scale 1:62,500.

Brooks, H. C., 1979b. Plate tectonics and geologic history of the Blue Mountains: Oregon, Geology, v. 41, no. 5, p. 71-80.

Brooks, H. C., and Vallier, T. L., 1978. Mesozoic rocks and tectonic evolution of eastern Oregon and western Idaho, *in* Howell, D. G., and McDougall, K. A., [eds], Mesozoic paleogeography of the Western United States (Pacific Coast Paleogeography Symposium 2): Los Angles, Society of Economic Paleontologists and Mineralogists, Pacific Section, p. 133-145.

Brown, D. E., Black, G. L., McLean, G. D., and Petros, J. R., 1980. Preliminary geology and geothermal resource potential of the Powell Buttes area, Oregon: Oregon Department of Geology and Mineral Industries Open-File Report O-80-8, 117 p.

Chapin, C.E., Wilks, M., McIntosh, W.C., 2004. Space-time patterns of Late Cretaceous to present magmatism in New Mexico—comparison with Andean volcanism and potential for future volcanism: New Mexico Bureau of Geology and Mineral Resources, Bulletin, v. 160, p. 13–40.

Christiansen, R.L., and Yeats, R.S., 1992. Post-Laramide geology of the U.S. Cordilleran region: *in* Burchfield, B.C., Lipman, P.W., and Zoback, M.L., [eds], The Cordilleran Orogen: Conterminous U.S.: Geological Society of America, The Geology of North America, v. G-3, p. 261-406

Christiansen, E. H. and McCurry, M., 2008. Constrating origins of Cenozoic silicic volcanic rocks from the western Cordillera of the United States: Bulletin of Volcanology, v. 70, p. 251-267.

Clemens, J. D., Holloway, J. R., White, A. J. R., 1986. Origin of A-type granite: Experimental constraints: American Mineralogist, v. 71, p. 317-314.

Conrad, W. K., 1984. The mineralogy and petrology of compositionally zoned ash flow tuffs, and related silicic volcanic rocs, from the McDermitt Caldera complex, Nevada-Oregon: Journal of Geophysical Research, v. 89, Issue B10, p. 8639-8664.

Collins, W. J., Beams, S. D., White, A. J. R., Chappell, B. W., 1982. Nature and Origin of A-type Granites with Particular Reference to Southeastern Australia: Contributions to Mineralogy and Petrology, v. 80, p. 189-200.

Dickinson, W. R., 1979. Mesozoic fore-arc basin in central Oregon: Geology, v. 7, p. 166-170.

Dickinson, W. R., 2004. Evolution of the western Cordillera of North America: Annual Review of Earth and Planetary Sciences, v. 32, p. 13-45.

Dickinson, W. R., and Thayer, T. P., 1978. Paleogeographic and paleotectonic implications of Mesozoic stratigraphy and structure in the John Day inlier of central Oregon, *in* Howell, D. G., and McDougall, K. A., [eds], Mesozoic paleogeography of the Western United States (Pacific Coast Paleogeography Symposium 2): Los Angles, Society of Economic Paleontologists and Mineralogists, Pacific Section, p. 147-161.

Dooley, D. F., and Patino Douce, A. E., 1996. Vapor absent melting of F- and Ti-rich phlogopite + quartz: Effects on phlogopite stability and melt compositions: American Mineralogist, v. 81, p. 202-212.

Dorsey, R. J. and LaMaskin, T. A., 2007. Stratigraphic record of Triassic-Jurassic Collisional Tectonics in the Blue Mountains Province, Northeastern Oregon: American Journal of Science, v. 307, p. 1167-1193.

Evans, S. H., and Brown, F. H., 1981. Summary of potassium/argon dating —1981: U.S. Department of Energy, Division of Geothermal Energy DE-AC07-80-ID-12079-45, p. 29.

Eby, G. N., 1990. The A-type granitoids: A review of their occurrence and chemical characteristics and speculations on their petrogenesis: Lithos, v. 26, p. 115-134.

Eby, G. N., 1992. Chemical subdivision of the A-type granitoids: Petrogenetic and tectonic implications: Geology, v. 20, p. 641-644.

Ferns, M. L. and Brooks, H. C., 1995. The Bourne and Greenhorn subterranes of the Baker Terrane, northeastern Oregon; implications for the evolution of the Blue Mountains island-arc system *In* Vallier, T. L. and Brooks, H C. [eds], Geology of the Blue Mountains region of Oregon, Idaho, and Washington; petrology and tectonic evolution of pre-Tertiary rocks of the Blue Mountains region: U.S. Geological Survey Professional Paper 1438, p. 331-558.

Ferns, M. L., Madin, I. P, and Taubeneck, W. H., 2001. Reconnaissance Geologic Map of the La Grande 30’ • 60’ quadrangle, Baker, Grant, Umatilla, and Union Counties, Oregon: Oregon Department of Geology and Mineral Industries Reconnaissance Map Series, RMS-1, 52 p., scale 1:100,000.

Fisher, R. V., 1964. Resurrected Oligocene Hills, eastern Oregon: American Journal of Science, v. 262, no. 6, p. 713-725.

Fisher, R. V., 1966a. Geology of a Miocene ignimbrite layer, John Day Formation, eastern Oregon: University of California Publications in Geological Sciences, v. 67, p. 1-57.

Fisher, R. V., and Rensberger, J. M., 1972. Physical Stratigraphy of the John Day Formation, central Oregon, University of California Publications in Geological Sciences, v. 101, p. 45.

Fuller, R. F., 1931. The geomorphology and volcanic sequence of Steens Mountain in southeastern Oregon: Washington University Geology Publications, v. 3, no. 1, p. 1-130.

Ghiorso, M. S. and Sack, R. O., 1995. Chemical mass transfer in magmatic processes; IV, A revised and internally consistent thermodynamic model for the interpolation and extrapolation of liquid-solid equilibria in magmatic systems at elevated temperatures and pressures: Contributions to Mineralogy and Petrology, v. 119, Issue 2-3, p. 197-212.

Goldstrand, P. M., 1994. The Mesozoic geologic evolution of the norther Wallowa Terrane, northeastern Oregon and western Idaho, *In* Vallier, T. L. and Brooks, H. C., [eds], Geology of the Blue Mountains region of the Oregon, Idaho, and Washington; stratigraphy, physiography, and mineral resources of the Blue Mountains region: U. S. Geological Survey Professional Paper 1439, p. 29-53.

Grand, S. P., 1994. Mantle shear structure beneath the Americas and surrounding oceans: Journal of Geophysical Research, v. 99, p. 11,591-1,621.

Gromme, C. S., Beck, M. E., Jr., Wells, R. E., and Engebreston, D. C., 1986. Paleomagnetism of the Tertiary Clarno Formation of central Oregon and its significance for the tectonic history of the Pacific Northwest: Journal of Geophysical Research, v. 91, p. 14,089-14,103.

Hay, R. L., 1962a. Origin and Diagenetic alteration of the lower part of the John Day Formation near Mitchell, Oregon, *in* Engle, A. E. J., James, H. L., and Leonard, B. F., [eds], Petrologic studies – A volume in honor of A. F. Buddington: New York, Geological Society of America, p. 191-216.

Hay, R. L., 1962b. Soda-rich sanidine of pyroclastic origin from the John Day Formation of Oregon: American Mineralogist, v. 47, no. 7-8, p. 968-971.

Hay, R. L., 1963. Stratigraphy and zeolite diagenesis of the John Day Formation of Oregon: University of California Publications in Geological Sciences, v. 42, no. 5, p. 199-262.

Hearn, T. M., Beghoul, N., and Barazangi, M., 1991. Tomography of the western United States from regional arrival times: Journal of Geophysical Research, v. 96, p. 16,369-16,381.

Henry, C. D., and Price, J. G., 1986. Early Basin and Range development in Trans-Pecos Texas and Chihuahua: Magmatism and orientation, timing and style of extension: Journal of Geophysical Research, v. 91, p. 6213-6224.

Henry, C. D., Price, J. G., and James, E. W., 1991. Mid-Cenozoic Stress Evolution and Magmatism in the Southern Cordillera, Texas and Mexico: Transition from Continental Arc to Intraplate Extension: Journal of Geophysical Research, v. 96, no. B8, p. 13545-13560.

Hildreth, W., 1979. The Bishop Tuff; evidence for the origin of compositional zonation in silicic magma chambers *In* Chapin, C. E. and Elston, W. E., Geological Society of America Special Paper, Issue 180, p. 43-75.

Hildreth, W. 2004. Volcanological perspectives on Long Valley, Mammoth Mountain, and Mono Craters; several contiguous but discrete systems: Journal of Volcanology and Geothermal Research, v. 136, Issue 3-4, p. 169-198.

Honjo, N., Bonnichsen, B., Leeman, W. P., and Stormer, J. C., Jr., 1992. Mineralogy and geothermometry of high-temperature rhyolites from the central and western Snake River Plain: Bulletin of Volcanology, v. 54, Issue 3, p. 220-237.

Humphreys, E. D., 1995. Post-Laramide Removal of the Farallon slab, western United States: Geology, v. 23, p. 987-990.

Humphreys, E. D., and Dueker, K. G., 1994a. Western U. S. Upper mantle structure: Journal of Geophysical Research, v. 99, p. 9615-9634.

James, E. W. and Henry, C. D., 1991. Compositional changes in Trans-Pecos Texas magmatism coincident with Cenozoic stress alignment: Journal of Geophysical Research, v. 96, p. 13561-13575.

Johnson, D. M., Hooper, P. R., 1999. XRF analysis of rocks and minerals major and trace elements on single low dilution Li-tetraborate fused bead: Advances in X-ray Analysis, v. 4, p. 843-867.

Kays, M. A., Stimac, J. P., and Goebel, P. M., 2006. Permian-Jurassic growth an amalgamation of the Wallowa composite terrane: Geological Society of America Special Paper 410.

Knaack, C., Cornelius, S., and Hooper, P. R., 1994. Trace element analysis of rocks and minerals by ICP-MS: Pullman, Washington State University Department of Geology Open File Report, 18 p.

LaMaskin, T. A., Schwartz, J. J., Dorsey, R. J., Snoke, A. W., Johnson, K., Vervoort, J. D., 2009. Mesozoic sedimentation, magmatism and tectonics in the Blue Mountains Province, northeastern Oregon, *in* O'Connor, L. E., Dorsey, R. J. and Madin, I. P. [eds], Volcanoes to Vineyards, Geologic Field Trips through the Dynamic Landscape of the Pacific Northwest, Field guide 15, p. 187-202.

Lawton, T.F., McMillan, N.J., 1999. Arc abandonment as a cause for passive rifting: comparison of the Jurassic Mexican borderland rift and the Cenozoic Rio Grande rift: Geology v. 27, p. 779–782.

Lee, R. G., 2004. The geochemistry, stable isotopic composition and U-Pb geochronology of tonalitic-trondhjemites within the accreted terranes, near Greer, north-central Idaho, [M.S. thesis]; Pullman, Washington, Washington State University.

Leeman, W. P., Smith, D. R., Hildreth, W., Palacz, Z., and Rogers, N., 1990. Compositional diversity of late Cenozoic basalts in a transect across the southern Washington Cascades; implications for subduction zone magmatism: Journal of Geophysical Research, November 10, 1990, v. 95, Issue B12, p.19,561-19,582.

Lipman, P. W., and Glazner, A. F., 1991. Introduction to Middle Tertiary Cordilleran volcanism; magma srouces and relations to regional tectonics: Journal of Geophysical Research, v. 96, Issue B8, p. 13,193-13,199.

Lipman, P. W., Prostka, H. J., Christiansen, R. L., 1971. Evolving subduction zones in the western United States as interpreted from igneous rocks, Science, 174, 821-825.

Loiselle, M.C., Wones, D.R., 1979. Characteristics and origin of anorogenic granites. Geological Society of America Abstracts with Programs v. 11 no. 7, p. 468.

Macdonald, R., 1974. Nomenclature and petrochemistry of the peralkaline oversaturated extrusive rocks: Bulletin of Volcanology, v. 38, p. 498-516.

Manduca, C .A., Kuntz, M. A., and Silver, L .T., 1993. Emplacement and deformation history of the western margin of the Idaho batholith near McCall: Influence of a major terrane boundary: Geological Society of America Bulletin, v. 105, p. 749-765.

Martin, R. F., 2006. A-type granites are ultimately results of open system fenitization-type reactions in a rift environment: Lithos, v. 91, p. 125-136.

McClaughry, J. D., and Ferns, M. L., 2006a. Preliminary geologic map of the Prineville 7.5' quadrangle, Crook County, Oregon, Oregon Department of Geology and Mineral Industries Open-File Report O-06-22, scale 1:24,000.

McClaughry, J. D., and Ferns, M. L., 2006b. Preliminary geologic map of the Ochoco Reservoir 7 .5' quadrangle, Crook County, Oregon. Oregon Department of Geology and Mineral Industries Open-File Report O-06-23, scale 1:24,000.

McClaughry, J. D., and Ferns, M. L., 2007. The Crooked River Caldera: Identification of an early Oligocene eruptive center in the John Day Formation of central Oregon: Geological Society of America Abstracts with Programs, v. 39, no. 4, p. 10.

McClaughry, J. D., Ferns, M. L., Gordon, C. L., and Patridge, K. A., 2008. Field trip guide to the Oligocene Crooked River caldera: Central Oregon's Supervolcano, Crook, Deschutes, and Jefferson Counties, Oregon: Oregon Geology, v. 69, no. 1, p. 25-44.

McClaughry, J. D., Ferns, M. L., Streck, M., Patridge, K. A., and Gordon, C. L., 2009. Paleogene calderas of central and eastern Oregon: Eruptive sources of widespread tuffs in the John Day and Clarno Formations *in* O'Connor, L. E., Dorsey, R. J. and Madin, I. P. [eds], Volcanoes to Vineyards, Geologic Field Trips through the Dynamic Landscape of the Pacific Northwest, Field guide 15, p. 407-443.

McClaughry, J. D., 2009, per communication, 1/2009.

McClelland, W. C., and Oldow, J. S., 2007. Late Cretaceous truncation of the western Idaho shear zone in the central North American Cordillera: Geology, v. 35, p. 723-726.

McDonough, W. F. and Sun, S.-s., 1995. The composition of the Earth: Chemical Geology, v. 120, Issue 3-4, p. 223-253.

McIntosh, W.C., Chapin, C.E., 2004, Geochronology of the central Colorado volcanic field: New Mexico Bureau of Geology and Mineral Resources, Bulletin, v. 160, p. 2058–2237.

McIntyre, D.H., Ekren, E.B., and Hardyman., R.F., 1982, Stratigraphic and structural framework of the Challis volcanics in the eastern half of the Challis 10' x 20' quadrangle, Idaho: *In* Bonnichsen, W., and Breckenridge, R.M., [eds], Cenozoic Geology of Idaho: Idaho Bureau of Mines and Geology, Bulletin 26, p. 3-22.

McMillan, N.J., Dickin, A.P., Haag, D., 2000. Evolution of magma source regions in the Rio Grande rift, southern New Mexico: Geological Society of America Bulletin 112, 1582–1593.

Merriam, J. C., 1901. A contribution to the geology of the John Day Basin [Oreg.]: University of California Publications, Department of Geology Bulletin, v. 2, p. 260-314.

Miller, C. F., McDowell, S. M. and Mapes, R. W., 2003. Hot and cold granites? Implications of zircon saturation temperatures and preservation of inheritance: Geology, v. 31, p. 529-532.

Moye, F. J., Hackett, W. R., Blakley, J. D., and Snider, L. G., 1988. Regional geologic setting and volcanic stratigraphy of the Challis volcanic field, central Idaho *In* Link, P. K. and Hackett, W. R., [eds], Guidebook to the geology of central and southern Idaho: Idaho Geological Survey, p. 87-99.

Mullen, E. D., and Sarewitz, D. M., 1983. Paleozoic and Triassic terranes of the Blue Mountains, northeast Oregon. Discussion and field trip guide, Part I. A new consideration of old problems: Oregon Geology, v. 45, p. 65-68.

Obermiller, W. A., 1987. Geologic structure, and geochemical features of basaltic and rhyolitic volcanic rocks of the Smith Rock/Gray Butte area, central Oregon: [M.S. thesis] Corvallis, Oregon, University of Oregon.

Parker, K. O., Schwartz, J. J., Johnson, K., 2008. Petrology and age of Dixie Butte plutonic rocks, Blue Mountains, NE Oregon [abs]: Geological Soceity of America Abstracts with Programs, v. 40, no. 6, p. 154-155.

Patino Douce, A. E., and Beard, J. S., 1995. Dehydration melting of biotite gneiss and quartz amphibolite from 3 to 15 kbar: Journal of Petrology, v. 36, p. 707-738.

Patino Douce, A. E., and Beard, J. S., 1996. Effects of P, $f(O_2)$ and Mg/Fe ratio on dehydration melting of model metagraywackes: Journal of Petrology, v. 37, p. 999-1024.

Patino Douce, A. E., 1997. Generation of metaluminous A-type granites by low-pressure melting of calc-alkaline granitoids: Geology, v. 25, no. 8, p. 743-746.

Pearce, J. A., Harris, N. B. W., Tindle, A. G., 1984. Trace element discrimination diagrams fro the tectonic interpretation of granitic rocks: Journal of Petrology, v. 25, part 4, p. 956-983.

Peck, D., 1964. Geological reconnaissance of the Antelope-Ashwood area, north-central Oregon, with emphasis on the John Day Formation of late Oligocene and early Miocene age: U.S. Geological Survey Bulletin 1661-D, D1-D25.

Retallack, G. J., Orr, W. N., Prothero, D. R., Duncan, R. A., Kester, P. R., and Ambers, C. P., 2004, Ecoene-Oligocene extinction and plaeoclimatic change near Eugene, Oregon: Geological Society of America Bulletin, v. 116, p. 817-839.

Riddihough, R., Finn, C. and Couch, R., 1986. Klamath-Blue Mountain lineament, Oregon: Geology, v. 14, p. 528-531.

Robinson , P. T., 1969. High titania alkali olivine basalts of north-central Oregon, U.S.A.: Contributions to Mineralogy and Petrology, v. 22, no. 4, p. 349-360.

Robinson , P. T., 1975. Reconnaissance geologic map of the John Day Formation in the southwestern part of the Blue Mountains and adjacent areas, north-central Oregon: U.S. Geological Survey Miscellaneous Investigations Series Map I-872, scale 1:125,000.

Robinson , P. T., 2006. Early Teritary volcanism in the Pacific Northwest: Implications for continental margin evolution [abs.]: Geological Society of America Abstracts with Programs, v. 38, no. 7, p. 213.

Robinson, P. T., and Brem, G. F., 1981. Guide to geologic field trip between Kimberly and Bend Oregon, with emphasis on the John Day Formation, *in* Johnston, D. A., and Donnelly-Nolan, Julie, [eds.], Guides to some volcanic terranes in Washington, Idaho, Oregon and northern California: U.S. Geological Survey Circular 838, p. 29-40.

Robinson, P. T., Brem, G. F., and McKee, E. H., 1984. John Day Formation of Oregon: a distal record of early Cascade volcanism, Geology, v. 12, p. 229–232.

Robinson, P. T., and Stensland, D. H., 1979. Geologic map of the Smith Rock area, Jefferson, Deschutes, and Crook Counties, Oregon: U.S. Geological Survey Miscellaneous Investigations Series Map I-1142, scale 1:48,000.

Robinson, P. T., Walker, G. W., and McKee. E. H., 1990. Eocene(?), Oligocene and lower Miocene rocks of the Blue Mountains region, *in* Walker, G. W., [eds], Geology of the Blue Mountains region of Oregon, Idaho, and Washington: U.S. Geological Survey Professional Paper 1437, p. 29–62.

Sherrod, D. R., Taylor, E. M., Ferns, M. L., Scott, W. E., Conrey, R. M., and Smith, G. A., 2004. Geologic map of the Bend 30 • 60 minute quadrangle, central Oregon: U.S. Geological Survey Geologic Investigations Series I-2683, 48 p., scale 1:100,000.

Silberling, N. J., Jones, D. L., Blake, M. C., and Howell, D. G., 1984. Lithotectonic terranes map of the western conterminous United States, Pt. C *In* Silberling, N. J., and Jones, D. L., [eds], Lithotectonic terrane maps of the North American Cordillera: U.S. Geological Survey Open-File Report 84-523, 43 p.

Skjerlie, K. P. and Johnston, A. D., 1993. Fluid absent melting behavior of an F-rich tonalitic gneiss at mid-crustal pressures: Implications for the generation of anorogenic granites: Journal of Petrology, v. 34, p. 785-815.

Smith, A. D., 1992, Back-arc convection model for Columbia River basalt genesis: Tectonophysics, v. 207, p. 269-285.

Smith, G. A., Manchester, S. R., Ashwill, M., McIntosh, W. C., and Conrey, R. M., 1998. Late Eocene-early Oligocene tectonism, volcanism, and floristic change near Gray Butte, central Oregon: Geological Society of America Bulletin, v. 110, p. 759–778.

Smith, R. L., 1979. Ash-flow magmatism *In* Chapin, C. E. and Elston, W. E. [eds] Ash-flow tuffs: Geological Society of America Special Paper, Issue 180, p. 5-27.

Smith, R. L., and Bailey, R. A., 1966. The Bandelier Tuff; a study of ash-flow eruption cycles from zoned magma chambers: Bulletin of Volcanology, v. 29, p. 83-103.

Streck, M. J., and Grunder, A. L., 1995. Crystallization and welding variations in a widespread ignibrite sheet; the Rattlesnake Tuff; eastern Oregon, USA: Bulleting of Volcanology, v. 57, p. 151-169.

Swanson, D. A., 1969. Reconnaissance geologic map of the east half of Bend quadrangle, Crook, Wheeler, Jefferson, Wasco, and Deschutes Counties, Oregon, *in* Geological Survey Research, 1968: U.S. Geological Survey Miscellaneous Geologic Investigations Map I-568, scale 1:250,000.

Synder, W. S., Dickinson, W. R., and Silberman, M. L., 1976. Tectonic implications of space-time patterns of Cenozoic magmatism in the Western United States: Earth and Planetary Science Letters, v. 32, no. 1, p. 91-106.

Taylor, E. M., 1990. Volcanic history and tectonic development of the Central High Cascade Range, Oregon: J. of Geophysical Research, v. 95, p. 19,611-19,622.

Tuttle, O. F., and Bowen, N.L., 1974, Origin of granite in light of experimental studies in the system $NaAlSi_3O_8$-$KAlSi_3O_8$-SiO_2-H_2O: Geological Society of America, Memoir 74.

Unruh, D. M., Lund, K., Kuntz, M. A., and Snee, L. W., 2008. Uranium-lead zircon ages and Sr, Nd, and Pb isotope geochemistry of select plutonic rocks from western Idaho: U.S. Geological Survey Open-File Report 2008-1142.

Urbanzyk , K. M., 1994. Geology of the Eastern part of the Clarno Formation, Northeast Oregon, [Ph. D dissertation] Pullman WA, Washington State University.

Vallier, T. L., 1995. Petrology of pre-Tertiary igneous rocks in the Blue Mountains Region, *in* Vallier, T. L., and Brooks, H. C., [eds], Geology of the Blue Mountains Region of Oregon, Idaho and Washington: Petrology and Tectonic Evolution of Pre-Tertiary Rocks of the Blue Mountains Region: U.S. Geological Survey Professional Paper 1438, p. 125-209.

Vallier, T. L., and Brooks, H. C., 1986. Paleozoic and Mesozoic faunas of the Blue Mountains province- A review of their geologic implications and comments on papers in the volume, *in* Vallier, T. L., and Brooks, H. C., [eds], Geology of he Blue Mountains region of Oregon, Idaho, and Washington – Geologic implications of Paleozoic and Mesozoic paleontology and biostratigraphy, Blue Mountains province, Oregon and Idaho: U.S. Geological Survey Professional Paper, 1435, p. 1-6.

Vallier, T. L., and Brooks, H. C., and Thayer, T. P., 1977. Paleozoic rocks of eastern Oregon and western Idaho, *in* Stewart, J. H., Stevens, C. H., and Fritsche, A. E., [eds], Paleozoic paleogeography of the western United States (Pacific Coast Paleography Symposium 1): Los Angles, Society of Economic Paleontologists and Mineralogists, Pacific Section, p. 455-466.

Vallier, T. L., and Engebretson, D. C., 1984. The Blue Mountains island arc of Oregon, Idaho and Washington – An allochthonous coherent terrane from the ancestral western Pacific Ocean? *in* Howell, D. G., Jones, D. L., Cox, Allan, Nur, Amos, [eds], Circum-Pacific Terrane Conference, Stanford, Calif., 1983, Proceedings, Standford University Publications/Geological Sciences, v. 18, p. 197-199.

Vance, J. A., 1982. Cenozoic stratigraphy and tectonics of the Washington Cascades: Geological Society of America Abstracts with Programs, v. 14, no. 4, p. 241.

Walker, G. W., and Robinson, P. T., 1990. Cenozoic Tectonism and volcanism of the Blue Mountains region, *in* Walker, G. W., [eds], Geology of the Blue Mountains region of Oregon, Idaho, and Washington: U.S. Geological Survey Professional Paper 1437, p. 119-135.

Walker, G. W., and MacLeod, N. S., 1991. Geologic map of Oregon: U.S. Geological Survey, scale, 1:500,000.

Walker, G. W., 1977. Rhyolitic volcanism in southeastern Oregon and the Snake River plain, Idaho; similarities and contrast: Abstracts with Programs - Geological Society of America, v. 9, Issue 7, p.1215-1216.

Walker, G. W., 1986. U/Pb geochronologic and petrologic studies in the Blue Mountains terrane, northeastern Oregon and western-most central Idaho: Implications for pre-Tertiary tectonic evolution. [Ph. D dissertation] Santa Barbra, University of California.

Walker, G. W., 1989. Early Cretaceous initiation of post-tectonic plutonism and the age of the Connor Creek fault, northeastern Oregon [abs.] Geological Society of America Abstracts with Programs, v. 21, no. 5, p. 155.

Waters, A. C., and Vaughn. R. H., 1968b. Reconnaissance geologic map of the Ochoco Reservoir quadrangle, Crook County, Oregon: U.S. Geological Survey Miscellaneous Geologic Investigations Map I-541, scale 1: 62,500.

Watson, E. B. and Harrison, T. M., 1983. Zircon saturation revisted: Temperature and composition effects in a variety of crustal magma types: Earth and Planetary Science Letters, v. 64, p. 295-304.

Wernicke, W. M., Christiansen, R. L., England, P. C., Sonder, L. J., 1987. Tectonomagmatic evolution of Cenozoic extension in the North American Cordillera *In* Coward, M. P., Dewey, J. F., and Hancock, P. J., [eds], Continental Extension Tectonics: Geological Society of American Special Publication 28, p. 203-221.

White, J. D. L., and Robinson, P. T., 1992. Intra-arc sedimentation in a low-lying marginal arc, Eocene Clarno Formation, central Oregon: Sedimentary Geology, v. 80, p. 89-114.

White, J. D. L., White, D. L, Vallier, T. L., Stanley, G. D. Jr., and Ash, S. R., 1992. Middle Jurassic strata link Wallowa, Olds Ferry and Izee terranes in the accreted Blue Mountains island arc, northeastern Oregon: Geology, v. 20, p. 729-732.

White, D. L. and Vallier, T. L., 1994. Geologic evolution of the Pittsbug landing area, Snake River Canyon, Oregon and Idaho *In* Vallier, T. L. and Brooks, H. C., [eds], Stratigraphy, Physiography and Mineral Resources of the Blue Moutains Region: U. S. Geological Survey, Reston, VA: Professional Paper 1439, p. 55-74.

Williams , Howel, 1957. A geologic map of the Bend quadrangle, Oregon and a reconnaissance geologic map of the central portion of the High Casacade Mountains: Portland, Oregon Department of Geology and Mineral Industries, scale 1:125,000 and 1:62,000.

Whalen, J. B., Currie, K. L., Chappell, B. W., 1987. A-type granites: geochemical characteristics, discrimination and petrogenesis: Contributions to Mineralogy and Petrology, v. 95, p. 407-419.

APPENDIX A

MAJOR, MINOR AND TRACE ELEMENT XRF DATA

whole rock XRF							
UNIT	Tjth	Tjth	Tjth	Tjth	Tjth	Tmr	Tjts
SAMPLE #	PAT HS5.1A	PAT HS5.2	PAT HS5.3	PAT HS10	PAT HS5.4	PAT GG	PAT 395
Normalized major element oxides (wt%)							
SiO_2	77.99	80.27	75.95	77.80	81.27	76.47	81.32
TiO_2	0.17	0.15	0.19	0.16	0.148	0.16	0.13
Al_2O_3	11.57	10.71	13.20	11.33	10.26	12.18	9.80
FeO	1.25	1.09	0.82	1.71	0.83	1.49	1.36
MnO	0.01	0.03	0.00	0.02	0.004	0.09	0.02
MgO	0.05	0.01	0.00	0.01	0.02	0.22	0.70
CaO	0.15	0.02	0.04	0.06	0.05	0.60	0.93
Na_2O	3.21	3.12	3.70	1.29	2.71	3.60	0.39
K_2O	5.53	4.58	6.06	7.60	4.65	5.06	5.35
P_2O_5	0.07	0.02	0.04	0.04	0.069	0.12	0.02
XRF trace elements (ppm)							
Ni	0.00	0.00	0.00	0.00	0.00	5.61	0.03
Cr	3.10	2.70	1.50	3.30	5.40	2.30	2.00
Sc	2.10	0.60	1.40	2.50	1.90	4.30	1.60
V	14.30	7.60	5.60	9.50	4.90	5.30	1.80
Ba	388.50	339.30	424.10	246.40	313.60	593.20	266.00
Rb	150.30	142.70	181.60	147.30	136.50	88.40	103.80
Sr	9.50	4.60	11.80	4.80	10.40	23.20	311.50
Zr	475.00	448.80	574.30	444.00	431.90	275.60	404.30
Y	90.30	42.50	73.50	79.70	76.10	87.90	87.40
Nb	44.40	42.30	54.30	40.10	41.70	27.30	36.40
Ga	26.20	24.80	29.30	24.30	24.00	20.20	17.80
Cu	5.50	0.50	0.80	7.60	0.50	3.70	9.40
Zn	65.30	65.00	46.40	96.80	44.10	101.20	97.60
Rb	7.20	10.00	13.00	10.90	13.00	18.10	2.70
La	33.20	28.70	69.90	45.70	75.50	37.50	60.80
Ce	119.50	84.60	153.70	111.80	122.70	89.20	117.80
Th	17.30	16.30	20.40	15.30	15.20	8.20	13.60
Nd	35.80	33.90	77.50	50.30	71.20	44.30	63.00
U	4.80	3.50	4.00	3.50	3.00	4.60	5.20

UNIT	Tjts	Tjts	Tjts	Tjts	Tjts	Tjts	Tjts
SAMPLE #	PAT HS4	PAT HS2	PAT HS9	PAT 393	PAT 394	PAT HS7.2	PAT HS19
Normalized major element oxides (wt%)							
SiO_2	82.99	76.20	73.90	71.42	78.11	85.28	84.08
TiO_2	0.13	0.24	0.14	0.17	0.15	0.099	0.103
Al_2O_3	8.76	12.36	12.84	14.94	10.84	7.54	8.02
FeO	1.27	2.29	1.38	2.53	1.92	1.08	1.16
MnO	0.02	0.03	0.01	0.04	0.03	0.008	0.007
MgO	0.64	0.38	0.21	0.33	0.11	0.00	0.01
CaO	1.90	1.66	0.77	0.49	0.10	0.05	0.03
Na_2O	0.61	0.96	1.23	0.42	0.33	1.34	1.33
K_2O	3.65	5.84	9.50	9.63	8.40	4.59	5.23
P_2O_5	0.04	0.04	0.03	0.02	0.02	0.015	0.017
XRF trace elements (ppm)							
Ni	0.00	0.00	0.00	0.00	0.00	0.00	0.00
Cr	1.60	1.40	0.60	2.80	1.00	2.70	2.40
Sc	1.60	2.60	0.60	0.90	0.00	0.40	0.30
V	4.70	8.10	14.60	7.00	16.60	1.10	6.10
Ba	356.20	437.00	167.50	227.20	110.50	173.70	197.90
Rb	70.60	137.10	176.00	237.60	180.00	89.40	129.50
Sr	101.70	49.80	9.70	22.40	7.70	4.40	4.60
Zr	332.70	393.10	392.90	496.10	419.50	262.70	288.70
Y	57.50	89.00	94.90	105.90	89.60	39.00	42.90
Nb	31.00	39.90	27.00	58.20	53.60	31.30	33.40
Ga	16.70	24.20	28.00	36.90	29.70	16.30	18.20
Cu	1.80	3.50	1.90	2.80	4.60	0.90	1.90
Zn	100.20	137.60	132.00	210.60	123.60	77.10	74.80
Rb	10.60	15.30	5.60	5.60	28.30	11.50	13.10
La	31.00	59.30	90.30	52.50	60.00	31.40	44.90
Ce	64.10	127.30	101.20	124.50	107.60	72.80	102.10
Th	14.10	16.50	15.10	20.20	20.30	12.20	11.90
Nd	33.30	62.90	100.70	59.80	68.50	34.20	48.00
U	2.50	5.20	5.30	4.40	5.20	2.50	3.20

UNIT	Tjts	Tjts	Tjts	Tjts	Tjts	Tjts	Tjts
SAMPLE #	PAT MS1	PAT MS2	PAT MS4	PAT MS3	PAT TF1	PAT TF2	PAT PP
Normalized major element oxides (wt%)							
SiO_2	76.89	75.16	76.56	80.95	76.65	76.03	77.37
TiO_2	0.236	0.263	0.226	0.231	0.294	0.305	0.28
Al_2O_3	12.60	12.47	12.58	10.33	11.50	11.51	11.46
FeO	1.18	2.76	1.52	0.68	2.80	3.04	2.76
MnO	0.014	0.051	0.017	0.012	0.040	0.030	0.06
MgO	0.17	0.23	0.10	0.05	0.05	0.11	0.47
CaO	0.43	0.85	0.45	0.11	0.29	0.27	1.71
Na_2O	4.16	3.95	4.33	3.02	3.32	2.74	1.38
K_2O	4.30	4.23	4.19	4.59	5.00	5.89	4.47
P_2O_5	0.031	0.035	0.027	0.031	0.058	0.065	0.04
XRF trace elements (ppm)							
Ni	0.77	0.00	0.09	0.00	0.00	0.00	0.00
Cr	3.10	4.00	2.90	2.90	5.60	3.40	3.10
Sc	3.00	4.40	3.00	1.60	3.80	3.70	3.90
V	4.90	7.00	3.70	3.50	32.00	16.40	4.10
Ba	956.80	923.90	956.10	257.80	415.80	516.50	718.00
Rb	122.40	119.60	119.50	147.50	155.40	149.30	105.30
Sr	44.40	53.30	41.20	13.70	18.30	20.10	68.60
Zr	512.60	483.20	507.10	485.00	582.50	548.50	465.40
Y	69.50	107.10	130.20	61.70	89.50	63.80	89.60
Nb	64.60	58.80	63.80	40.20	44.70	42.60	50.50
Ga	28.40	25.60	26.40	21.90	24.50	23.70	19.90
Cu	2.20	4.60	3.20	1.30	6.30	4.70	2.30
Zn	124.50	153.70	197.80	77.50	122.40	120.20	114.50
Rb	12.30	13.60	12.60	10.80	13.90	17.40	11.00
La	67.80	73.60	71.90	57.90	61.40	61.70	59.90
ce	124.80	148.80	135.20	117.20	134.10	126.70	126.50
Th	16.40	14.50	16.50	15.10	16.40	14.80	14.70
Nd	65.20	68.40	72.00	57.00	63.10	58.20	63.10
U	4.00	4.00	5.00	3.70	4.30	5.30	3.70

UNIT	Tjts	Tjts	Tjts lithic	Tjrgm	Tjtt	Tjtt	Tjtt
SAMPLE #	PAT 352	PAT SR10.2	PAT SR13	PAT GR1	PAT PR 16	PAT PR18	PAT PR20
Normalized major element oxides (wt%)							
SiO_2	77.63	77.18	85.77	77.87	72.20	74.34	77.02
TiO_2	0.20	0.25	0.14	0.221	0.555	0.387	0.378
Al_2O_3	11.77	11.34	7.42	11.99	13.33	11.78	11.38
FeO	2.04	2.60	1.08	1.35	3.97	3.05	2.94
MnO	0.05	0.10	0.02	0.008	0.060	0.035	0.047
MgO	0.13	0.19	0.06	0.02	0.41	0.25	0.58
CaO	0.69	0.77	0.27	0.18	1.68	0.19	1.51
Na_2O	2.12	1.86	2.30	3.93	1.28	0.19	1.33
K_2O	5.34	5.49	2.91	4.36	6.45	9.75	4.75
P_2O_5	0.02	0.22	0.02	0.060	0.056	0.031	0.061
XRF trace elements (ppm)							
Ni	0.00	1.70	1.50	0.77	6.22	0.32	1.00
Cr	1.40	2.60	1.90	1.90	13.10	7.90	10.80
Sc	2.50	3.00	1.70	2.50	9.60	6.20	5.30
V	1.40	2.10	1.30	0.10	26.00	23.20	20.40
Ba	956.30	872.40	544.80	994.30	363.50	51.50	426.00
Rb	161.40	175.60	77.70	128.40	110.70	143.90	95.30
Sr	23.60	38.70	27.80	39.70	90.60	4.00	86.00
Zr	419.20	421.00	252.10	545.50	297.00	290.20	291.90
Y	93.10	95.60	58.00	86.20	60.90	50.00	80.30
Nb	48.10	49.50	30.90	57.00	31.00	31.60	31.10
Ga	20.90	25.10	14.80	25.30	20.70	17.90	19.70
Cu	2.10	4.90	1.30	2.30	17.30	7.30	10.00
Zn	121.10	150.30	51.20	115.40	92.60	67.90	117.50
Rb	13.00	14.80	6.80	13.80	14.00	9.50	15.40
La	66.40	59.30	35.10	71.10	50.00	43.70	45.70
Ce	138.30	134.70	81.10	145.80	102.40	91.20	94.40
Th	16.00	13.60	7.80	16.20	10.10	9.40	9.50
Nd	69.00	64.80	39.50	73.80	52.40	42.70	47.50
U	4.90	3.00	3.60	2.60	3.80	3.70	5.00

UNIT	Tjtt	--	--	--	Tjte	Tjte	Tjro
SAMPLE #	PAT PR 24	PAT PR25	PAT PR 27	PAT PR28	PAT ER2	PAT ER3	PAT OR1
Normalized major element oxides (wt%)							
SiO_2	75.10	71.16	78.22	74.45	78.76	77.77	73.44
TiO_2	0.540	0.779	0.204	0.391	0.19	0.197	0.31
Al_2O_3	12.85	13.82	11.84	13.35	10.51	11.37	13.27
FeO	2.99	4.50	1.37	3.28	2.09	2.44	2.97
MnO	0.048	0.168	0.021	0.034	0.03	0.077	0.07
MgO	0.32	0.92	0.04	0.80	0.23	0.08	0.27
CaO	0.84	2.34	0.24	0.62	0.62	0.28	0.46
Na_2O	4.75	2.88	3.97	5.20	3.46	3.65	4.90
K_2O	2.46	3.31	4.01	1.80	4.06	4.10	4.24
P_2O_5	0.092	0.118	0.082	0.074	0.05	0.040	0.07
XRF trace elements (ppm)							
Ni	0.00	1.09	0.00	0.00	0.00	0.00	3.64
Cr	5.20	11.80	5.60	6.90	2.20	2.60	2.60
Sc	10.70	13.40	1.20	7.10	2.50	2.00	4.40
V	38.10	56.70	8.10	27.40	8.30	8.90	9.70
Ba	163.40	675.60	940.60	153.20	792.30	878.90	734.70
Rb	52.10	81.20	110.30	48.40	101.10	110.50	108.40
Sr	44.80	184.50	40.20	26.30	48.80	35.40	46.50
Zr	324.50	287.40	498.40	379.60	479.20	463.90	763.20
Y	52.60	41.40	102.50	94.60	87.30	116.90	82.10
Nb	17.10	20.00	62.60	45.10	52.10	58.90	58.90
Ga	10.40	18.40	25.20	20.90	22.20	24.30	26.30
Cu	19.20	19.60	1.50	7.70	1.10	2.40	4.10
Zn	69.50	98.10	158.80	118.40	156.30	140.80	123.90
Rb	10.10	7.90	11.80	12.30	8.50	11.60	9.80
La	26.30	20.50	79.10	61.90	59.60	69.40	61.20
Ce	58.20	42.70	153.70	129.70	128.20	138.10	120.30
Th	10.20	5.90	15.90	13.50	13.00	14.30	14.60
Nd	33.00	24.60	74.40	68.50	62.80	67.90	59.90
U	3.40	1.80	4.70	3.40	3.50	3.60	2.90

UNIT	Tjtb	Tjrb	Tjrb	Tjrg	Tjrg	Tjrg	Tjrg
SAMPLE #	PAT BB3	PAT BB1	PAT OR2A	PAT GB1	PAT GB353	PAT GB3L	PAT GB2L
Normalized major element oxides (wt%)							
SiO_2	82.68	78.05	78.18	84.35	80.50	78.11	80.94
TiO_2	0.15	0.16	0.15	0.14	0.41	0.17	0.15
Al_2O_3	8.97	11.27	11.61	8.16	8.71	11.72	8.96
FeO	1.64	1.80	1.15	1.29	4.69	1.60	1.74
MnO	0.03	0.02	0.01	0.02	0.06	0.05	0.03
MgO	0.00	0.09	0.08	0.04	0.08	0.05	0.10
CaO	0.18	0.14	0.17	0.13	0.75	0.22	0.60
Na_2O	2.95	2.47	3.64	2.12	3.88	4.30	0.16
K_2O	3.37	5.98	4.95	3.73	0.85	3.76	7.30
P_2O_5	0.03	0.02	0.06	0.03	0.05	0.02	0.03
XRF trace elements (ppm)							
Ni	3.56	7.13	0.00	3.25	0.00	2.57	2.39
Cr	2.20	3.90	2.00	1.00	1.80	2.00	2.60
Sc	1.40	0.70	2.30	0.40	10.00	1.60	2.30
V	2.50	13.80	4.00	2.00	0.40	1.30	2.30
Ba	682.40	503.20	520.20	652.60	259.70	1092.50	371.80
Rb	99.60	134.80	124.40	109.30	21.90	132.70	104.40
Sr	23.50	12.50	11.40	16.20	20.20	49.10	5.90
Zr	364.10	334.60	340.50	309.30	579.70	410.60	294.40
Y	47.20	66.80	69.30	53.20	86.80	96.50	62.00
Nb	43.00	40.00	40.50	45.50	49.40	56.50	36.10
Ga	19.80	21.00	22.90	17.90	25.50	24.00	18.70
Cu	2.00	4.90	3.80	2.80	3.80	2.40	6.80
Zn	84.20	98.50	93.00	111.10	143.20	151.90	99.30
Rb	8.30	10.90	12.00	8.00	12.40	17.40	11.30
La	72.30	53.80	54.30	55.70	51.80	61.10	42.50
Ce	141.90	102.70	110.80	113.20	122.00	143.60	93.00
Th	10.80	12.40	14.90	12.60	12.40	15.70	10.30
Nd	68.90	51.90	54.70	53.90	63.10	68.80	46.60
U	2.10	3.50	4.70	3.30	4.40	4.20	3.60

UNIT	Tjrg	Tjir	Tjir	Tjir	Tjir	Tjta	Tjta
SAMPLE #	PAT GB2R	PAT SR1	PAT SR5	PAT SR8	PAT SR11	PAT PR8	PAT PR9
Normalized major element oxides (wt%)							
SiO_2	72.04	79.77	81.60	79.69	72.20	73.24	77.38
TiO_2	0.24	0.18	0.14	0.17	0.41	0.84	0.28
Al_2O_3	13.05	10.72	9.37	11.35	13.04	11.87	10.65
FeO	2.82	1.05	1.42	0.30	4.71	6.28	3.23
MnO	0.07	0.00	0.03	0.00	0.13	0.05	0.07
MgO	0.24	0.02	0.02	0.00	0.09	1.06	0.24
CaO	0.84	0.07	0.07	0.03	1.01	3.10	0.46
Na_2O	0.53	0.94	1.03	0.74	3.63	1.68	2.69
K_2O	10.12	7.22	6.30	7.70	4.73	1.71	4.96
P_2O_5	0.05	0.03	0.02	0.01	0.05	0.18	0.05
XRF trace elements (ppm)							
Ni	2.85	0.00	3.30	5.83	3.70	4.69	3.90
Cr	2.50	4.30	0.60	1.20	1.30	19.40	1.60
Sc	2.50	2.40	1.20	0.30	8.00	16.30	3.60
V	5.10	0.60	0.20	2.10	0.60	76.70	33.50
Ba	1389.90	891.30	768.00	935.10	1006.80	507.70	770.00
Rb	216.70	269.30	195.70	306.80	136.50	53.90	90.60
Sr	16.40	18.00	20.00	26.30	92.00	344.10	60.90
Zr	438.80	421.20	353.10	438.40	691.90	133.60	474.00
Y	96.10	60.10	70.70	53.50	100.70	25.90	66.00
Nb	51.80	50.70	44.00	53.60	59.20	9.10	35.90
Ga	26.70	16.70	18.70	18.70	25.20	16.30	19.40
Cu	6.60	3.60	2.70	1.70	3.60	20.20	4.40
Zn	169.80	61.80	82.70	51.60	165.60	139.50	122.70
Rb	17.30	11.20	9.30	13.40	11.10	9.60	8.60
La	57.80	64.90	51.80	26.60	68.50	12.00	45.00
Ce	125.50	138.20	112.80	75.00	134.80	19.80	93.00
Th	14.20	14.40	12.70	15.60	12.80	1.70	7.30
Nd	63.80	66.60	52.30	33.70	68.90	17.10	48.30
U	2.80	4.60	3.20	3.90	4.20	1.60	1.90

UNIT	Tjta	Tjta	Tjta	Tjta	Tjta	Tjta	Tceb
SAMPLE #	PAT PH1G	PAT PH1TA	PAT PH1LTA	PAT PH3	PAT 454	PAT PH1W	PAT MG
Normalized major element oxides (wt%)							
SiO_2	72.54	74.09	74.76	74.39	73.71	70.79	50.97
TiO_2	0.36	0.49	0.47	0.44	0.42	0.39	0.86
Al_2O_3	13.70	11.64	11.29	11.81	12.22	18.03	15.29
FeO	4.26	5.23	5.17	4.74	4.76	3.43	8.66
MnO	0.10	0.16	0.09	0.06	0.05	0.04	0.19
MgO	0.48	0.28	0.30	0.30	0.32	0.89	9.11
CaO	1.80	1.60	1.59	1.52	1.32	2.65	11.52
Na_2O	2.61	3.36	3.28	3.61	3.67	1.81	2.11
K_2O	4.10	3.02	2.90	2.99	3.43	1.92	1.03
P_2O_5	0.05	0.14	0.13	0.15	0.11	0.04	0.25
XRF trace elements (ppm)							
Ni	4.23	5.03	0.00	0.00	0.00	4.66	74.25
Cr	2.90	7.20	9.70	11.40	5.30	3.40	393.20
Sc	4.90	11.40	10.80	9.70	8.50	6.20	41.00
V	11.70	62.90	67.30	83.30	83.10	15.50	258.00
Ba	815.20	822.60	801.30	953.90	908.30	1541.30	488.70
Rb	80.30	62.60	63.90	68.40	81.10	25.40	15.90
Sr	141.10	158.80	156.90	152.10	138.10	588.70	565.60
Zr	547.00	408.10	401.40	425.30	472.60	614.90	69.10
Y	77.40	58.90	60.50	68.90	52.80	44.90	20.80
Nb	41.20	31.40	30.50	31.80	34.90	38.30	4.40
Ga	28.50	23.90	21.70	24.50	24.50	30.50	13.30
Cu	5.00	7.00	6.80	12.20	7.80	3.20	75.80
Zn	175.70	134.50	132.40	155.60	145.50	156.30	66.60
Rb	12.80	7.60	7.80	8.20	9.40	9.70	3.30
La	46.30	40.30	37.10	51.50	35.60	48.40	12.80
Ce	107.30	74.70	75.30	92.60	66.80	97.50	27.30
Th	9.70	6.20	7.70	9.00	10.00	10.90	3.50
Nd	58.40	46.60	45.00	54.70	38.20	57.40	13.60
U	2.50	1.30	1.80	2.50	3.60	1.20	0.90

UNIT	Tjba	Tjba	Tjba	Tjba	Tjba	Tjba
SAMPLE #	PAT PR7	PAT PR3	PAT PR 29	PAT PR1	PAT PR6	PAT PR4
Normalized major element oxides (wt%)						
SiO_2	53.46	53.08	53.57	55.97	56.05	57.18
TiO_2	2.68	2.82	2.765	1.98	1.99	1.71
Al_2O_3	14.62	14.74	14.58	14.40	14.49	13.13
FeO	12.21	11.87	11.84	12.07	11.85	13.91
MnO	0.24	0.24	0.225	0.24	0.24	0.34
MgO	3.46	3.78	3.78	2.61	2.47	1.39
CaO	7.57	7.87	7.46	6.29	6.40	6.23
Na_2O	3.91	3.88	3.91	4.15	4.18	3.80
K_2O	0.86	1.01	1.19	1.38	1.39	1.59
P_2O_5	0.99	0.70	0.683	0.93	0.94	0.72
XRF trace elements (ppm)						
Ni	5.22	7.64	2.81	1.36	4.40	4.19
Cr	0.70	2.40	1.80	0.00	1.40	0.30
Sc	30.90	33.50	32.50	29.90	29.30	39.80
V	180.50	281.80	276.50	106.00	105.10	14.00
Ba	398.60	369.50	369.50	420.90	426.40	613.40
Rb	12.10	10.40	23.40	28.90	28.10	22.20
Sr	334.40	321.70	311.90	282.40	289.20	268.80
Zr	219.80	220.90	221.50	229.90	229.80	426.60
Y	48.20	44.30	43.10	50.10	51.10	60.50
Nb	18.50	18.10	18.00	17.70	18.20	30.00
Ga	20.60	20.00	20.60	21.40	22.10	23.50
Cu	11.60	13.60	17.00	3.70	9.70	13.80
Zn	125.80	125.00	130.80	131.10	129.40	177.60
Rb	3.90	4.10	5.00	4.70	4.00	6.20
La	25.60	26.20	22.20	24.60	30.10	36.00
Ce	58.50	52.30	51.40	60.10	59.40	82.80
Th	2.20	3.10	2.50	3.00	2.80	4.90
Nd	41.20	30.60	34.00	38.30	38.50	48.40
U	1.00	2.00	0.80	2.00	1.10	2.80

APPENDIX B

WHOLE ROCK

ICP TRACE ELEMENT DATA

whole rock ICP trace

UNIT	Tjth	Tjth	Tjth	Tjth	Tjth	Tmr	Tjts
SAMPLE #	PAT HS5.1A	PAT HS5.2	PAT HS5.3	PAT HS10	PAT HS5.4	PAT GG	PAT 395
(ppm)							
La	32.99	32.57	74.92	50.76	76.94	39.46	62.80
Ce	124.15	87.34	158.45	118.46	123.03	89.70	122.40
Pr	9.22	9.31	21.15	13.51	18.97	11.91	16.95
Nd	36.81	34.80	80.94	52.75	76.10	47.96	67.07
Sm	9.10	7.80	17.84	12.16	16.85	12.77	15.65
Eu	0.86	0.67	1.37	1.08	1.24	1.44	1.27
Gd	11.24	6.47	15.10	12.11	15.45	13.14	15.61
Tb	2.27	1.23	2.53	2.26	2.51	2.47	2.78
Dy	15.74	8.18	15.30	14.74	14.71	15.96	17.41
Ho	3.42	1.74	3.06	3.13	3.09	3.40	3.53
Er	9.63	5.19	8.63	8.91	8.39	9.66	9.71
Tm	1.40	0.83	1.31	1.35	1.26	1.48	1.42
Yb	8.49	5.21	8.22	8.56	7.81	9.38	8.63
Lu	1.29	0.76	1.23	1.31	1.20	1.49	1.32
Ba	388.94	344.47	429.29	253.00	329	610.85	280.48
Th	14.63	14.34	18.24	14.14	14.02	8.12	11.63
Nb	46.93	43.18	54.82	43.07	42.36	28.31	39.19
Y	92.28	42.55	72.60	82.27	75.63	88.60	90.77
Hf	14.77	13.61	17.48	13.78	12.84	8.98	12.14
Ta	3.24	3.00	3.81	2.88	2.97	1.79	2.56
U	4.67	3.88	4.72	3.38	3.94	3.63	4.44
Pb	7.32	10.19	14.02	11.67	12.03	17.74	3.85
Rb	155.77	142.17	181.69	152.69	141.4	90.95	107.53
Cs	2.83	3.32	2.65	1.13	2.81	3.30	9.70
Sr	10.47	5.30	11.79	5.08	10	24.40	322.11
Sc	1.31	1.15	1.34	1.64	1.0	4.72	1.01
Zr	492.64	456.33	584.65	460.43	426	283.89	421.24

UNIT	Tjts	Tjts	Tjts	Tjts	Tjts	Tjts	Tjts
SAMPLE #	PAT HS4	PAT HS2	PAT HS9	PAT 393	PAT 394	PAT HS7.2	PAT HS19
(ppm)							
La	34.44	63.38	94.81	56.08	61.09	34.30	48.42
Ce	73.53	134.11	106.47	131.06	106.26	75.83	101.58
Pr	9.06	16.98	25.75	16.77	16.56	8.90	12.75
Nd	35.09	67.84	106.84	65.56	67.69	34.76	50.22
Sm	8.24	16.15	24.67	16.29	16.39	8.10	11.19
Eu	0.80	1.63	1.66	1.19	1.09	0.70	1.06
Gd	9.17	16.17	21.22	17.81	16.28	7.76	9.86
Tb	1.72	2.76	3.41	3.48	2.81	1.34	1.76
Dy	10.89	17.01	20.18	22.24	17.59	8.12	10.31
Ho	2.10	3.53	4.00	4.41	3.64	1.60	1.95
Er	4.91	9.81	10.88	11.45	10.32	4.28	5.16
Tm	0.57	1.47	1.63	1.65	1.51	0.64	0.77
Yb	2.79	9.16	10.36	10.25	9.16	3.88	4.80
Lu	0.36	1.39	1.55	1.55	1.36	0.58	0.71
Ba	371.47	452.78	174.71	234.00	112.01	180.57	204
Th	12.44	14.39	13.65	19.46	17.73	9.88	10.90
Nb	33.06	42.50	29.36	62.01	54.66	32.95	33.98
Y	58.66	91.01	99.82	111.18	88.11	38.87	41.32
Hf	11.32	12.46	13.36	16.93	13.32	8.87	9.48
Ta	2.74	2.91	3.20	4.09	3.25	2.15	2.35
U	3.62	4.24	6.16	5.43	5.12	2.94	3.46
Pb	12.24	15.98	7.23	7.57	28.78	12.53	11.99
Rb	73.20	139.71	182.87	247.82	180.28	91.34	132.4
Cs	7.20	6.23	10.33	11.36	7.46	1.01	2.36
Sr	103.93	50.85	10.53	22.97	7.85	4.70	4
Sc	1.08	2.62	1.00	1.05	0.84	0.67	0.5
Zr	349.24	398.12	408.16	514.76	414.90	274.16	292

UNIT	Tjts	Tjts	Tjts	Tjts	Tjts	Tjts	Tjts
SAMPLE #	PAT MS1	PAT MS2	PAT MS4	PAT MS3	PAT TF1	PAT TF2	PAT PP
(ppm)							
La	65.21	76.30	72.21	61.58	64.25	62.45	64.45
Ce	126.78	149.88	136.11	117.18	131.76	130.10	135.17
Pr	17.40	18.93	18.67	15.32	16.21	16.04	16.91
Nd	68.32	74.86	73.72	57.87	63.59	61.46	67.09
Sm	15.60	17.03	16.99	12.68	14.56	13.89	15.76
Eu	2.54	2.54	2.55	0.89	1.16	1.48	2.85
Gd	14.07	17.23	17.67	11.64	14.65	12.55	15.62
Tb	2.44	3.06	3.27	2.01	2.52	2.18	2.83
Dy	14.61	19.31	21.56	12.23	15.63	13.29	18.02
Ho	2.89	4.03	4.71	2.49	3.31	2.68	3.73
Er	7.92	11.29	13.49	6.84	9.16	7.29	10.46
Tm	1.16	1.64	1.99	1.03	1.36	1.10	1.58
Yb	7.23	10.22	12.39	6.60	8.49	7.03	9.80
Lu	1.07	1.57	1.92	1.01	1.34	1.08	1.52
Ba	969.95	945.60	964.99	260.04	416.79	526.90	752.32
Th	14.91	14.05	14.89	14.88	16.21	14.93	12.96
Nb	64.40	59.06	63.41	40.37	45.12	42.95	54.20
Y	67.69	107.18	128.26	61.02	88.60	64.73	93.47
Hf	15.20	14.33	14.96	13.14	15.15	14.33	13.57
Ta	4.12	3.78	4.07	2.75	3.08	2.82	3.46
U	4.57	4.45	4.71	4.57	4.75	4.52	4.21
Pb	11.70	13.27	13.29	11.04	14.22	17.83	10.43
Rb	123.40	122.18	119.70	150.32	157.52	152.62	110.22
Cs	3.06	4.86	3.21	2.13	3.72	1.27	2.98
Sr	40.50	51.45	40.71	12.83	18.34	20.32	71.55
Sc	3.61	4.22	3.44	2.32	4.15	4.85	3.79
Zr	508.96	488.08	502.16	488.45	577.27	549.14	484.25

UNIT	Tjts	Tjts	Tjts lithic	Tjrgm	Tjtt	Tjtt	Tjtt
SAMPLE #	PAT 352	PAT SR10.2	PAT SR13	PAT GR1	PAT PR 16	PAT PR18	PAT PR20
(ppm)							
La	68.22	64.95	38.53	74.82	50.44	46.84	50.30
Ce	143.04	140.40	83.93	150.97	104.45	95.97	98.35
Pr	17.78	17.44	9.79	19.31	13.33	11.89	12.91
Nd	70.36	69.98	39.10	76.49	55.19	46.12	52.47
Sm	16.27	16.40	9.07	17.34	12.83	10.31	12.51
Eu	2.42	2.51	1.44	3.08	1.63	1.07	1.28
Gd	16.03	16.61	9.20	16.90	12.23	9.77	13.43
Tb	2.85	2.88	1.65	2.92	2.11	1.70	2.35
Dy	17.80	18.18	10.58	17.61	12.73	10.22	14.55
Ho	3.67	3.77	2.20	3.56	2.56	2.05	3.02
Er	10.21	10.51	6.23	9.56	7.06	5.53	8.09
Tm	1.52	1.54	0.93	1.41	1.05	0.82	1.14
Yb	9.45	9.58	5.76	8.82	6.70	5.32	6.95
Lu	1.45	1.45	0.88	1.33	1.02	0.82	1.04
Ba	983.89	907.37	562.46	1021	380.38	52.36	443.54
Th	13.64	13.43	7.65	14.55	9.73	9.60	9.73
Nb	49.54	51.34	30.99	57.77	32.54	31.96	33.23
Y	92.64	96.62	56.44	85.31	62.06	48.79	80.93
Hf	12.97	12.97	7.81	15.08	8.94	8.67	8.94
Ta	3.29	3.37	1.86	3.72	2.08	2.13	2.30
U	4.33	4.65	3.39	3.74	3.66	3.87	5.01
Pb	14.46	15.09	6.28	13.93	14.53	10.32	17.07
Rb	162.41	179.61	78.61	131.8	113.99	144.64	100.17
Cs	4.87	28.07	2.30	2.60	3.05	1.93	2.67
Sr	23.59	39.48	27.08	40	93.66	3.47	89.09
Sc	2.20	3.12	1.68	2.2	9.33	7.09	5.74
Zr	426.17	432.75	260.40	539	295.73	285.74	293.97

UNIT	Tjtt	--	--	--	Tjte	Tjte	Tjro
SAMPLE #	PAT PR 24	PAT PR25	PAT PR 27	PAT PR28	PAT ER2	PAT ER3	PAT OR1
(ppm)							
La	30.17	23.61	78.77	66.04	61.70	68.24	61.94
Ce	61.59	49.90	156.35	135.19	125.80	144.39	122.08
Pr	8.18	6.41	20.29	17.30	16.25	17.91	16.22
Nd	34.12	26.16	80.86	71.67	64.16	71.18	63.94
Sm	8.25	6.50	18.68	16.71	14.81	16.86	14.88
Eu	1.51	1.70	2.64	2.28	2.43	2.46	2.67
Gd	8.26	6.94	18.04	16.15	14.34	17.87	14.13
Tb	1.44	1.24	3.15	2.81	2.56	3.34	2.55
Dy	9.20	8.05	19.68	17.67	16.02	21.17	16.17
Ho	2.02	1.68	4.05	3.70	3.33	4.52	3.40
Er	5.81	4.65	11.19	10.04	9.30	12.56	9.40
Tm	0.86	0.71	1.66	1.46	1.40	1.84	1.44
Yb	5.50	4.48	10.10	9.12	8.69	11.51	9.35
Lu	0.84	0.70	1.52	1.36	1.35	1.74	1.44
Ba	169.36	698.13	962.86	158.96	807.51	896.87	754.82
Th	9.13	6.92	14.69	12.46	11.59	13.47	13.15
Nb	17.21	20.97	62.88	47.50	52.80	58.81	59.57
Y	53.69	41.82	101.22	96.73	86.41	115.97	82.78
Hf	9.23	7.76	14.77	11.41	13.51	13.69	19.41
Ta	1.28	1.37	3.99	3.14	3.31	3.77	3.93
U	2.95	1.88	3.60	3.18	2.72	3.07	3.76
Pb	9.78	8.60	11.66	12.36	8.60	11.23	9.85
Rb	53.30	82.91	111.35	51.46	100.45	110.42	108.66
Cs	7.24	2.87	1.56	10.42	1.91	1.68	1.64
Sr	46.13	190.83	40.32	27.27	48.64	35.56	47.89
Sc	10.17	13.68	2.10	7.63	2.47	2.87	4.71
Zr	330.20	282.97	493.97	377.47	484.99	452.43	771.51

UNIT	Tjtb	Tjrb	Tjrb	Tjrg	Tjrg	Tjrg	Tjrg
SAMPLE #	PAT BB3	PAT BB1	PAT OR2A	PAT GB1	PAT GB353	PAT GB3L	PAT GB2L
(ppm)							
La	74.01	54.35	57.82	56.36	52.72	70.41	47.17
Ce	147.24	109.29	118.29	118.72	124.97	147.03	99.49
Pr	18.75	13.92	14.89	14.44	15.91	18.20	12.57
Nd	72.22	53.92	58.29	56.13	64.36	71.19	50.21
Sm	15.04	12.05	13.31	12.38	16.06	16.20	11.79
Eu	1.98	0.90	0.91	1.64	4.00	2.13	1.75
Gd	10.64	11.48	12.73	10.85	15.87	15.34	11.73
Tb	1.64	1.98	2.21	1.81	2.87	2.78	2.04
Dy	9.17	12.47	13.74	10.77	17.83	17.50	12.40
Ho	1.80	2.55	2.79	2.20	3.60	3.62	2.54
Er	5.10	7.00	7.64	6.06	9.73	9.94	6.90
Tm	0.79	1.06	1.14	0.93	1.44	1.47	1.05
Yb	5.23	6.56	7.20	6.12	8.95	9.21	6.74
Lu	0.80	1.01	1.11	0.96	1.37	1.40	1.03
Ba	703.55	515.35	533.52	665.75	259.09	1123.79	389.40
Th	10.04	11.84	12.74	12.07	10.52	14.55	10.03
Nb	43.49	40.67	42.87	45.89	50.57	57.00	37.63
Y	45.80	65.48	70.74	52.51	87.42	95.79	63.19
Hf	10.63	10.23	10.96	9.51	14.99	12.76	9.41
Ta	2.91	2.79	2.97	2.89	3.17	3.81	2.57
U	2.84	4.36	4.57	3.89	4.50	4.02	3.28
Pb	8.49	10.66	11.94	8.20	13.15	17.30	11.35
Rb	101.87	137.86	127.67	111.02	22.71	131.75	107.59
Cs	2.19	1.35	2.77	1.40	0.23	1.90	0.18
Sr	23.54	12.63	11.92	17.08	21.15	49.67	7.05
Sc	0.90	1.65	1.28	1.67	10.13	1.94	2.34
Zr	364.10	340.64	356.34	300.51	591.50	413.69	305.22

UNIT SAMPLE #	Tjta PAT PR10	Tjta PAT PR11	Tjta PAT PR2	Tjta PAT PR12	Tjta PAT PR13	Tjta PAT PR14	Tjta PAT PH2.1
(ppm)							
La	41.76	44.59	45.78	45.89	45.93	48.68	44.31
Ce	89.56	79.06	100.72	98.28	90.21	112.59	92.91
Pr	11.85	12.70	13.07	12.99	13.07	13.68	12.84
Nd	49.86	53.33	54.30	54.27	53.98	57.56	53.27
Sm	12.19	13.08	13.23	13.49	13.12	14.45	13.17
Eu	2.89	3.20	3.21	3.13	3.10	3.31	3.17
Gd	12.34	13.34	13.37	13.77	12.98	14.86	13.09
Tb	2.14	2.35	2.36	2.41	2.25	2.63	2.32
Dy	13.37	14.66	14.68	15.15	13.99	16.51	14.36
Ho	2.74	3.00	3.04	3.11	2.89	3.39	2.90
Er	7.49	8.16	8.27	8.53	7.87	9.13	7.91
Tm	1.09	1.21	1.24	1.24	1.17	1.34	1.17
Yb	6.78	7.52	7.70	7.62	7.32	8.24	7.38
Lu	1.04	1.18	1.19	1.19	1.14	1.28	1.14
Ba	888.16	999.56	1047.79	1022.20	1034.36	1050.12	999.57
Th	7.47	7.99	8.47	8.21	8.53	8.34	8.04
Nb	34.69	36.78	38.36	37.18	38.98	36.74	36.46
Y	66.43	76.03	75.70	79.21	71.37	85.40	71.27
Hf	11.06	12.10	12.66	12.24	12.84	12.28	11.89
Ta	2.21	2.36	2.50	2.43	2.49	2.40	2.35
U	2.74	2.71	3.04	2.83	2.55	2.91	3.08
Pb	12.95	10.11	10.33	11.09	10.63	10.56	10.16
Rb	74.51	84.54	87.16	83.82	83.96	82.02	78.27
Cs	0.93	2.96	2.07	2.06	1.63	2.45	2.35
Sr	111.21	122.30	119.58	128.72	121.31	133.39	132.78
Sc	4.56	4.79	4.76	4.84	5.13	5.79	5.28
Zr	449.38	487.17	508.75	499.01	512.55	491.83	477.67

UNIT	Tjba	Tjba	Tjba	Tjba	Tjba	Tjba
SAMPLE #	PAT PR7	PAT PR3	PAT PR 29	PAT PR1	PAT PR6	PAT PR4
(ppm)						
La	24.54	22.45	22.40	25.63	25.34	32.96
Ce	56.84	51.32	51.69	59.89	59.18	77.00
Pr	8.14	7.20	7.24	8.42	8.36	10.68
Nd	37.84	33.04	32.73	38.87	38.27	48.09
Sm	9.90	8.65	8.55	10.20	10.01	12.49
Eu	3.42	2.95	2.93	3.42	3.37	4.19
Gd	10.60	9.23	9.25	10.91	10.80	12.98
Tb	1.71	1.52	1.49	1.73	1.77	2.13
Dy	10.05	9.05	8.98	10.51	10.46	12.79
Ho	1.99	1.82	1.81	2.10	2.09	2.54
Er	5.11	4.76	4.76	5.49	5.36	6.67
Tm	0.71	0.67	0.66	0.75	0.76	0.96
Yb	4.24	4.02	3.99	4.52	4.53	6.00
Lu	0.65	0.62	0.62	0.70	0.71	0.95
Ba	393.54	365.56	368	417.50	415.20	607.43
Th	2.94	2.69	2.67	3.33	3.27	4.37
Nb	19.28	18.84	18.82	18.86	18.76	31.44
Y	49.48	45.10	44.56	52.08	51.51	62.41
Hf	5.43	5.32	5.43	5.75	5.69	9.63
Ta	1.30	1.25	1.25	1.24	1.23	1.95
U	1.00	0.93	0.94	1.22	1.20	1.60
Pb	4.35	3.85	6.06	4.16	4.53	6.42
Rb	12.86	9.79	23.7	28.99	27.98	22.20
Cs	1.12	0.25	0.23	0.46	0.61	0.73
Sr	345.45	328.36	321	292.05	295.40	278.16
Sc	31.29	32.63	32.9	28.57	28.76	39.87
Zr	213.49	213.47	213	226.16	223.32	417.28

APPENDIX C

MICROPROBE FELDSPAR COMPOSITIONS

Microprobe feldspar compositions

UNIT	Tjts	Tjts	Tjts	Tjts	Tjts	Tjts	Tjts	Tjts
SAMPLE #	HS1	HS1	HS1	HS1	HS1	HS1	HS1	HS1
Al_2O_3	18.64	19.03	18.90	18.95	18.95	19.09	18.73	18.56
SiO_2	65.73	65.72	65.96	66.14	65.66	66.43	66.30	65.62
FeO	0.17	0.17	0.23	0.20	0.19	0.17	0.17	0.21
CaO	0.16	0.17	0.15	0.22	0.12	0.16	0.09	0.16
Na_2O	6.60	6.35	6.42	6.53	6.42	6.57	6.81	6.56
K_2O	7.14	6.97	6.99	6.92	6.80	7.04	7.01	7.03
BaO	n.a.	n.a.	n.a.	n.a.	n.a.	n.a.	n.a.	n.a.
Total	98.45	98.41	98.65	98.95	98.14	99.46	99.11	98.14

UNIT	Tjts	Tjts	Tjts	Tjts	Tjts	Tjts	Tjts	Tjts
SAMPLE #	HS1	HS1	HS2	HS2	HS2	HS2	HS2	HS2
Al2O3	18.65	19.03	18.64	18.05	18.85	18.56	18.74	18.36
SiO2	65.48	66.38	66.43	65.30	66.66	66.44	67.52	66.88
FeO	0.17	0.14	0.19	0.21	0.20	0.19	0.23	0.24
CaO	0.14	0.29	0.42	0.32	0.47	0.33	0.30	0.33
Na2O	6.54	6.87	7.30	7.22	7.31	7.40	7.25	7.29
K2O	6.94	6.18	6.02	5.89	5.93	6.04	5.86	5.92
BaO	n.a.	n.a.	0.45	0.17	0.39	0.37	0.29	0.30
Total	97.92	98.89	99.45	97.16	99.80	99.34	100.19	99.32

UNIT	Tjts	Tjts	Tjts	Tjts	Tjts	Tjts	Tjts	Tjts
SAMPLE #	HS2	HS2	HS2	HS2	HS2	HS2	HS7.2	MS1
Al2O3	18.95	18.91	18.76	18.75	18.29	18.68	19.05	20.81
SiO2	68.00	68.51	68.05	68.13	67.69	67.90	66.21	65.30
FeO	0.18	0.22	0.20	0.21	0.23	0.21	0.19	0.23
CaO	0.36	0.32	0.28	0.34	0.16	0.37	0.35	2.49
Na2O	7.40	7.28	7.24	7.03	6.90	7.20	6.57	9.19
K2O	5.90	6.11	6.20	6.22	6.91	5.96	6.17	1.51
BaO	0.47	0.40	0.37	0.39	0.08	0.39	n.a.	0.23
Total	101.27	101.74	101.11	101.06	100.27	100.70	98.54	99.76

UNIT	Tjts	Tjts	Tjts	Tjts	Tjts	Tjts	Tjts	Tjts
SAMPLE #	MS1	MS1	MS1	MS1	MS1	MS1	TF1	TF1
Al_2O_3	20.79	20.51	20.60	20.77	20.35	20.73	18.87	18.76
SiO_2	66.30	65.70	64.75	66.88	64.45	65.44	65.93	66.54
FeO	0.29	0.20	0.24	0.22	0.23	0.22	0.18	0.22
CaO	2.52	2.23	2.51	2.41	2.23	2.38	0.42	0.41
Na_2O	9.09	9.12	9.23	9.11	9.51	9.11	6.15	6.21
K_2O	1.36	1.69	1.41	1.57	1.55	1.56	7.51	7.58
BaO	0.17	0.17	0.19	0.28	0.21	0.21	0.16	0.22
Total	100.52	99.62	98.92	101.24	98.53	99.64	99.21	99.93

UNIT	Tjts	Tjts	Tjts	Tjts	Tjts	Tjts	Tjts	Tjts
SAMPLE #	TF1	TF1	TF1	TF1	TF1	TF1	TF1	TF1
Al2O3	19.31	18.63	18.76	18.39	18.76	18.80	18.81	18.50
SiO2	67.88	66.70	65.87	65.40	66.95	66.15	66.53	67.29
FeO	0.22	0.20	0.19	0.19	0.21	0.19	0.18	0.18
CaO	0.56	0.46	0.55	0.47	0.65	0.64	0.66	0.41
Na2O	6.42	6.56	6.50	6.56	6.53	6.71	6.41	6.15
K2O	7.17	7.29	6.98	7.21	6.97	6.94	6.91	7.50
BaO	0.28	0.21	0.20	0.22	0.22	0.31	0.35	0.18
Total	101.84	100.05	99.05	98.42	100.30	99.75	99.84	100.21

UNIT	Tjts	Tjts	Tjts	Tjts	Tjts	Tjts	Tjts	Tjts
SAMPLE #	TF1	TF1	TF1	TF2	TF2	TF2	TF2	TF2
Al2O3	18.97	18.70	18.64	18.94	19.59	18.57	19.01	18.91
SiO2	67.89	67.07	66.58	66.53	66.06	66.56	66.22	66.73
FeO	0.17	0.20	0.17	0.22	0.17	0.18	0.16	0.20
CaO	0.47	0.51	0.53	0.53	0.96	0.43	0.50	0.45
Na2O	6.30	6.41	6.16	6.35	7.25	6.39	6.62	6.39
K2O	7.32	7.24	7.43	7.24	5.56	7.36	7.40	7.10
BaO	0.25	0.17	0.30	0.22	0.27	0.19	0.31	0.19
Total	101.36	100.30	99.81	100.03	99.86	99.70	100.23	99.97

UNIT	Tjts	Tjts	Tjts	Tjts	Tjrgm	Tjrgm	Tjrgm	Tjro
SAMPLE #	PP	PP	PP	PP	GR1	GR1	GR1	OR1
Al_2O_3	24.22	17.66	17.85	17.92	20.03	20.17	18.26	21.15
SiO_2	60.53	66.60	66.33	66.00	64.88	66.20	66.69	64.08
FeO	0.31	-0.02	0.02	-0.02	0.21	0.23	0.50	0.38
CaO	5.31	0.02	0.00	-0.02	1.71	1.23	0.09	2.88
Na_2O	7.49	0.09	0.09	0.06	8.21	8.03	6.31	8.97
K_2O	0.79	16.03	15.71	16.24	3.58	4.37	7.86	1.55
BaO	n.a.	n.a.	n.a.	n.a.	0.41	0.54	0.24	0.22
Total	98.66	100.40	100.00	100.20	99.04	100.77	99.94	99.24
UNIT	Tjro	Tjro	Tjro	Tjro	Tjro	Tjro	Tjro	Tjro
SAMPLE #	OR1	OR1	OR1	OR1	OR1	OR1	OR1	OR1
Al2O3	21.93	22.04	21.81	21.53	21.50	21.59	21.46	21.48
SiO2	64.28	64.10	62.97	64.04	64.02	63.34	63.84	63.44
FeO	0.33	0.39	0.40	0.40	0.37	0.40	0.48	0.42
CaO	3.57	3.54	3.88	3.45	3.17	3.51	3.38	3.26
Na2O	8.70	8.78	8.83	8.78	8.87	9.19	8.97	8.96
K2O	1.22	1.42	1.26	1.25	1.36	1.32	1.49	1.56
BaO	0.13	0.07	0.17	0.16	0.24	0.16	0.14	0.15
Total	100.17	100.34	99.32	99.62	99.54	99.50	99.76	99.27
UNIT	Tjro	Tjro	Tjta	Tjta	Tjta	Tjta	Tjta	Tjta
SAMPLE #	OR1	OR1	PR10	PR10	PR10	PR10	PR10	PR10
Al2O3	21.70	21.94	24.26	23.72	23.97	23.74	24.14	23.85
SiO2	64.07	63.63	60.94	60.37	60.73	60.39	60.57	61.38
FeO	0.41	0.36	0.51	0.44	0.44	0.47	0.49	0.44
CaO	3.54	3.47	6.50	6.40	6.14	6.53	6.66	6.33
Na2O	9.03	8.55	7.55	7.57	7.40	7.35	7.68	7.34
K2O	1.20	1.32	0.48	0.46	0.58	0.51	0.57	0.56
BaO	0.09	0.17	0.10	0.04	0.02	0.02	0.02	0.00
Total	100.05	99.45	100.34	99.01	99.28	99.01	100.13	99.90

UNIT	Tjta	Tjta	Tjta	Tjta	Tjta	Tjta	Tjta	Tjta
SAMPLE #	PR10	PR10	PR10	PR10	PR10	PR10	PR10	PR10
Al_2O_3	23.95	24.17	24.78	24.84	25.01	24.82	24.55	24.79
SiO_2	60.83	61.29	60.43	59.91	60.54	59.88	60.74	60.89
FeO	0.44	0.39	0.40	0.43	0.43	0.39	0.41	0.47
CaO	6.56	6.49	6.53	6.56	6.58	6.52	6.18	6.44
Na_2O	7.41	7.36	7.08	7.15	7.06	6.98	7.24	7.32
K_2O	0.56	0.53	0.51	0.54	0.49	0.48	0.54	0.53
BaO	0.13	0.04	0.00	0.10	0.10	0.08	0.03	0.06
Total	99.87	100.27	99.74	99.53	100.21	99.14	99.68	100.50

UNIT	Tjta	Tjta	Tjta	Tjta	Tjta	Tjta	Tjta	Tjta
SAMPLE #	PR10	PH3	PH3	PH3	PH3	PH3	PH3	PH3
Al2O3	24.90	24.34	23.84	21.64	24.34	24.16	24.26	24.16
SiO2	60.16	60.68	60.86	65.49	60.77	61.66	61.54	61.25
FeO	0.47	0.43	0.48	0.26	0.48	0.37	0.45	0.43
CaO	6.58	7.00	6.72	3.03	6.98	6.48	6.63	6.54
Na2O	7.32	7.19	7.33	8.98	7.09	7.33	7.24	7.33
K2O	0.49	0.53	0.48	1.37	0.50	0.54	0.53	0.53
BaO	0.05	0.09	0.10	0.29	0.19	0.07	0.01	0.04
Total	99.97	100.26	99.82	101.05	100.35	100.61	100.66	100.28

UNIT	Tjta	Tjta	Tjta	Tjta	Tjta	Tjta	Tjta	Tjta
SAMPLE #	PH3	PH3	PH3	PH3	PH3	PH1G	PH1G	PH1G
Al2O3	24.00	24.22	23.95	24.19	24.12	24.03	23.79	24.19
SiO2	60.52	61.60	61.34	61.09	60.98	61.02	61.63	61.55
FeO	0.44	0.38	0.36	0.43	0.46	0.45	0.45	0.48
CaO	6.51	6.50	6.38	6.62	6.57	6.80	6.63	6.69
Na2O	7.44	7.67	7.53	7.16	7.23	7.32	7.29	7.42
K2O	0.52	0.55	0.55	0.48	0.54	0.54	0.53	0.49
BaO	0.07	0.12	0.09	0.09	-0.01	0.04	0.12	0.12
Total	99.51	101.05	100.21	100.05	99.90	100.19	100.44	100.94

UNIT	Tjta	Tjta	Tjta	Tjta	Tjta	Tjta	Tjta	Tjta
SAMPLE #	PH1G	PH1G	PH1G	PH1G	PH1G	PH1G	PH1G	PH1G
Al_2O_3	23.96	24.11	23.82	24.21	23.97	24.44	24.29	23.95
SiO_2	61.15	61.30	60.91	61.36	60.48	61.79	61.41	59.59
FeO	0.44	0.40	0.50	0.45	0.50	0.46	0.50	0.46
CaO	6.78	6.42	6.45	6.69	6.59	6.51	6.51	6.57
Na_2O	7.52	7.37	7.50	7.24	7.32	7.32	7.31	7.55
K_2O	0.47	0.49	0.60	0.46	0.48	0.54	0.53	0.50
BaO	0.10	-0.01	0.06	0.06	0.09	0.07	0.04	0.04
Total	100.43	100.08	99.84	100.47	99.44	101.13	100.59	98.66
SAMPLE #	PH2.1	PH2.1	PH2.1	PH2.1	PH2.1	PH2.1	PH2.1	PH2.1
Al2O3	24.22	23.44	23.96	24.27	24.19	24.67	24.20	24.09
SiO2	59.20	60.79	59.60	59.67	59.61	59.07	59.23	59.67
FeO	0.42	0.32	0.40	0.42	0.42	0.36	0.29	0.39
CaO	6.79	5.24	6.25	6.04	6.70	6.65	6.69	6.37
Na2O	7.13	7.67	6.88	7.12	7.04	7.18	6.77	7.24
K2O	0.48	0.65	0.56	0.53	0.49	0.49	0.46	0.53
BaO	n.a.	n.a.	n.a.	n.a.	n.a.	n.a.	n.a.	n.a.
Total	98.23	98.11	97.65	98.05	98.46	98.42	97.64	98.29
UNIT	Tjta	Tjta	Tjta	Tjta	Tjta	Tjta	Tjta	Tjta
SAMPLE #	PH2.1	PR12	PR12	PR12	PR12	PR12	PR12	PR12
Al2O3	18.95	24.46	24.29	24.51	24.21	24.45	24.52	24.62
SiO2	66.33	58.62	59.37	59.00	59.42	59.38	59.33	59.31
FeO	0.16	0.35	0.41	0.36	0.43	0.40	0.43	0.45
CaO	0.54	6.53	6.44	6.54	6.36	6.70	6.56	6.54
Na2O	5.46	7.26	7.11	7.18	7.36	6.96	6.87	7.46
K2O	8.07	0.49	0.50	0.50	0.47	0.48	0.49	0.58
BaO	n.a.	n.a.	n.a.	n.a.	n.a.	n.a.	n.a.	n.a.
Total	99.51	97.71	98.11	98.09	98.25	98.36	98.20	98.95

UNIT	Tjta	Tjta	Tjta	Tjta	Tjta	Tjta	Tjta	Tjta
SAMPLE #	PR12	PR12	PR12	PH1TA	PH1TA	PH1TA	PH1TA	PH1TA
Al_2O_3	25.09	24.38	19.21	23.93	24.27	23.97	24.42	25.56
SiO_2	59.06	58.80	65.29	58.93	59.10	59.23	58.97	57.96
FeO	0.32	0.32	0.47	0.41	0.41	0.43	0.42	0.51
CaO	6.97	6.75	0.75	6.44	6.41	6.47	6.61	7.75
Na_2O	7.22	6.88	5.22	7.38	6.90	7.30	6.91	6.79
K_2O	0.48	0.45	8.13	0.50	0.48	0.52	0.51	0.31
BaO	n.a.	n.a.	n.a.					
Total	99.14	97.56	99.07	97.59	97.58	97.92	97.85	98.88

UNIT	Tjta	Tjta	Tjta	Tjta	Tjta	Tjta	Tjta	Tjta
SAMPLE #	PH1TA	PH1TA	PH1TA	PH1TA	PH1TA	PH1TA	PH1TA	PH1TA
Al2O3	24.28	24.18	24.28	24.11	24.75	26.64	24.60	24.10
SiO2	58.95	59.76	59.52	59.78	59.12	55.97	59.08	59.56
FeO	0.35	0.41	0.43	0.40	0.37	0.36	0.43	0.43
CaO	6.53	6.39	6.45	6.35	6.58	8.87	6.55	6.47
Na2O	7.09	7.01	7.08	7.13	6.90	6.25	7.23	7.28
K2O	0.48	0.52	0.53	0.57	0.52	0.19	0.50	0.52
BaO								
Total	97.68	98.26	98.29	98.35	98.24	98.28	98.38	98.35

UNIT	Tjta	Tjta	Tjta	Tjta	Tjta
SAMPLE #	PH1TA	PH1TA	PH1TA	PH1TA	PH1TA
Al_2O_3	23.73	25.69	25.69	22.09	21.65
SiO_2	60.75	57.84	57.95	62.98	63.65
FeO	0.39	0.39	0.40	0.33	0.31
CaO	5.76	8.04	7.90	3.62	3.02
Na_2O	7.46	6.64	6.77	8.30	8.43
K_2O	0.61	0.21	0.38	1.01	1.15
BaO					
Total	98.70	98.81	99.09	98.33	98.20

APPENDIX D

MICROPROBE PYROXENE COMPOSITIONS

MIcroprobe pyroxene compositions

UNIT	Tjta	Tjta	Tjta	Tjta	Tjta	Tjta	Tjta	
SAMPLE #	PH1G	PH1G	PH1G	PH1G	PH1G	PH1G	PH1G	
FeO	29.61	29.73	29.47	29.55	29.53	29.40	29.46	
TiO_2	0.44	0.46	0.48	0.47	0.47	0.46	0.48	
CaO	19.36	19.26	19.26	19.05	19.39	19.17	19.10	
SiO_2	47.89	48.91	48.76	48.18	48.32	47.28	47.20	
Al_2O_3	0.79	0.82	0.84	0.85	0.81	0.79	0.79	
MgO	0.58	0.67	0.66	0.65	0.63	0.63	0.56	
MnO	1.09	1.09	1.04	1.04	1.03	1.04	1.05	
Na_2O	0.20	0.21	0.20	0.17	0.18	0.27	0.22	
Total	99.97	101.16	100.70	99.96	100.35	99.03	98.87	
UNIT	Tjro	Tjro	Tjro	Tjro	Tjro	Tjro	Tjro	Tjro
SAMPLE #	OR1	OR1	OR1	OR1	OR1	OR1	OR1	OR1
FeO	22.34	20.28	19.74	21.26	21.15	20.38	20.16	20.02
TiO_2	0.31	0.29	0.28	0.35	0.29	0.29	0.30	0.32
CaO	18.30	19.29	17.55	18.58	18.72	19.20	19.59	19.43
SiO_2	49.84	50.12	53.73	49.88	50.27	48.77	50.13	49.95
Al_2O_3	0.62	0.67	0.92	0.71	0.60	0.64	0.72	0.73
MgO	6.80	7.46	6.65	7.21	7.21	7.46	7.49	7.72
MnO	1.14	0.97	1.00	1.06	1.07	0.97	0.96	0.98
Na_2O	0.36	0.30	0.31	0.29	0.35	0.31	0.33	0.37
Total	99.71	99.39	100.18	99.34	99.66	98.02	99.68	99.51

APPENDIX E

SAMPLE LOCATIONS

Sample #	Unit		E	N
PAT HS5.1A	Rhy. Tuff at Haystack Reservoir	Tjth	647555	4928936
PAT HS5.2	Rhy. Tuff at Haystack Reservoir	Tjth	647555	4928936
PAT HS5.3	Rhy. Tuff at Haystack Reservoir	Tjth	647555	4928936
PAT HS10	Rhy. Tuff at Haystack Reservoir	Tjth	647453	4928853
PAT HS5.4	Rhy. Tuff at Haystack Reservoir	Tjth	647555	4928936
PAT GG	Rattlesnake Tuff	Tmr	688711	4902390
PAT 395	Rhy. Tuff at Haystack Reservoir	Tjts	646553	4928628
PAT HS4	Rhy. Tuff at Haystack Reservoir	Tjts	647582	4928880
PAT HS2	Rhy. Tuff at Haystack Reservoir	Tjts	647177	4928760
PAT HS9	Rhy. Tuff at Haystack Reservoir	Tjts	647482	4928825
PAT 393	Rhy. Tuff at Haystack Reservoir	Tjts	646691	4928468
PAT 394	Rhy. Tuff at Haystack Reservoir	Tjts	646612	4928481
PAT HS7.2	Rhy. Tuff at Haystack Reservoir	Tjts	647374	4928860
PAT HS19	Rhy. Tuff at Haystack Reservoir	Tjts	647374	4928860
PAT MS1	Rhy. Tuff at McKay Saddle	Tjts	687627	4931373
PAT MS2	Rhy. Tuff at McKay Saddle	Tjts	687598	4931652
PAT MS4	Rhy. Tuff at McKay Saddle	Tjts	687550	4932290
PAT MS3	Rhy. Tuff at McKay Saddle	Tjts	687491	4932332
PAT TF1	Rhy. Tuff at Teller Flat	Tjts	661269	4945844
PAT TF2	Rhy. Tuff at Teller Flat	Tjts	661269	4945844
PAT PP	Smith Rock Tuff	Tjts	671472	4911016
PAT 352	Smith Rock Tuff	Tjts	648600	4917700
PAT SR10.2	Smith Rock Tuff	Tjts	648243	4913412
PAT SR13	Smith Rock Tuff lithic	Tjts	--	--
PAT GR1	Grizzly Rhyolite Dome	Tjrgm	662943	4922320
PAT PR 16	Tuffaceous Sed. Rocks and Tuff	Tjtt	680868	4889887
PAT PR18	Tuffaceous Sed. Rocks and Tuff	Tjtt	680871	4889883

Sample #	Unit		E	N
PAT PR 16	Tuffaceous Sed. Rocks and Tuff	Tjtt	680868	4889887
PAT PR18	Tuffaceous Sed. Rocks and Tuff	Tjtt	680871	4889883
PAT PR20	Tuffaceous Sed. Rocks and Tuff	Tjtt	680871	4889883
PAT PR 24	Tuffaceous Sed. Rocks and Tuff	Tjtt	681532	4888045
PAT PR25	Rhy. Welded Tuff		681456	4888096
PAT PR 27	Rhy. Welded Tuff		681061	4888524
PAT PR28	Lapilli Tuff		681382	4888148
PAT ER2	Eagle Rock Rhy. Tuff	Tjte	688100	4896174
PAT ER3	Eagle Rock Rhy. Tuff	Tjte	688100	4896174
PAT OR1	Ochoco Reservoir Rhyolite	Tjro	681584	4907109
PAT BB3	Barnes Butte Rhy. Dome	Tjtb	673991	4909989
PAT BB1	Barnes Butte Rhy. Tuff	Tjrb	673100	4908352
PAT OR2A	Barnes Butte Rhy. Tuff	Tjrb	681043	4906892
PAT GB1	Gray Butte Rhy. Dome	Tjrg	648660	4917900
PAT GB353	Gray Butte Rhy. Dome	Tjrg	648115	4918090
PAT GB3L	Gray Butte Lithic in Smith Rock Tuff	Tjrg	648700	4917780
PAT GB2L	Gray Butte Rhy. Dike	Tjrg	648125	4918065
PAT GB2R	Gray Butte Rhy. Dike	Tjrg	648125	4918065
PAT SR1	Smith Rock Dike	Tjir	648264	4914083
PAT SR5	Smith Rock Dike	Tjir	647954	4913912
PAT SR8	Smith Rock Dike	Tjir	648097	4913985
PAT SR11	Smith Rock Dike	Tjir	648866	4914885
PAT PR8	Tuff of Antelope Creek	Tjta	680285	4888930
PAT PR9	Tuff of Antelope Creek	Tjta	680285	4888930
PAT PR10	Tuff of Antelope Creek	Tjta	680285	4888930
PAT PR11	Tuff of Antelope Creek	Tjta	680285	4888930
PAT PR2	Tuff of Antelope Creek	Tjta	680285	4888930
PAT PR12	Tuff of Antelope Creek	Tjta	680285	4888930

Sample #	Unit		E	N
PAT PR13	Tuff of Antelope Creek	Tjta	680285	4888930
PAT PR14	Tuff of Antelope Creek	Tjta	680285	4888930
PAT PH2.1	Tuff of Antelope Creek	Tjta	687905	4897654
PAT PH1G	Tuff of Antelope Creek	Tjta	687905	4897654
PAT PH1TA	Tuff of Antelope Creek	Tjta	687905	4897654
PAT PH1LTA	Tuff of Antelope Creek	Tjta	687905	4897654
PAT PH3	Tuff of Antelope Creek	Tjta	687905	4897654
PAT 454	Tuff of Antelope Creek	Tjta	688070	4901620
PAT PH1W	Tuff of Antelope Creek	Tjta	687905	4897654
PAT MG	Olivine Basalt	Tceb	683700	4889150
PAT PR7	Basaltic Andesites	Tjba	680115	4888850
PAT PR3	Basaltic Andesites	Tjba	680115	4888850
PAT PR 29	Basaltic Andesites	Tjba	681598	4887669
PAT PR1	Basaltic Andesites	Tjba	680115	4888850
PAT PR6	Basaltic Andesites	Tjba	680115	4888850
PAT PR4	Basaltic Andesites	Tjba	680115	4888850